# Optical Spectroscopy And Cavity QED Experiments With Rydberg Atoms

**Pierre Thoumany**

München, 2011

# Optical Spectroscopy And Cavity QED Experiments With Rydberg Atoms

Dissertation
der Fakultät für Physik
Ludwig-Maximilians-Universität München

vorgelegt von
**Pierre Thoumany**
aus Gif sur Yvette, Frankreich

München, Februar 2011

| | |
|---|---|
| Supervisor (first referee): | Professor Dr. Theodor W. Hänsch |
| Second referee: | Professor Dr. Wolfgang Lange |

Examination date: 07.04.2011

# Zusammenfassung

In dieser Arbeit konnte zum ersten Mal die Wechselwirkung zwischen Atomen im Grundzustand eines Zwei-Niveau-Systems und dem quantisierten thermischen Feld eines MW-Resonators untersucht werden.

Der Ein-Atom-Maser, oder Mikromaser, ist ein einzigartiges physikalisches System für die Untersuchung von Quanten-Aspekten der Wechselwirkung von Strahlung und Materie. Ein Zwei-Niveau-System von $^{85}Rb$ Rydberg-Atomen koppelt an ein einzelne Mode eines Mikrowellen Resonators mit einer hohen Güte. Durch die großen Dipol-Matrix-Elemente der einzelnen Rydberg-Atome und den supraleitenden Mikrowellenresonator mit einem Güte von $10^{10}$ kann der Bereich der starken Kopplung erreicht werden und die kohärente Wechselwirkung zwischen dem atomaren Zwei-Niveau-System und dem Resonatorfeld ist dominant. Daher ist die Beobachtung von Rabi Oszillationen und die Produktion von nichtklassischen Feld Zuständen möglich was auch in dieser Arbeit gezeigt werden konnte.

Bisherige Mikromaser Experimente zeigten einige Widersprüchlichkeiten zwischen der theoretischen Vorhersage und den Messergebnissen. Insbesondere bei tiefen Temperaturen war der beobachte Kontrast geringer als der theoretisch erwartete Kontrast. Eine mögliche Erklärung hierfür ist eine höhere Temperatur des Resonatorfeldes. Indirekte Temperatur Messungen an den Resonatorwänden sind durch externe Halbleiter-Temperatursensoren durchgeführt worden. Allerdings konnte keine direkte Temperaturmessung des Felds unterhalb 1K realisiert werden. Die experimentelle Realisierung von Rabi-Oszillationen zwischen dem Grundzustand des Zwei-Niveau-Systems und den quantisierten thermischen Resonatorfeld gibt eine direkte Messung der Feldstatistik und die Resonatorfeld Temperatur kann extrahiert werden. In dieser Arbeit werden zum ersten Mal Experimente mit den Rydberg Zustand $61D_{5/2}$ realisiert und kohärente Wechselwirkung wird gezeigt. Für eine hohe Zahl in den Resonator injizierter Atome konnten erste Maserlinien in dieser Konfiguration beobachtet werden. Bei einer niedrigen Injektionsrate, werden Rabi-Oszillationen mit hohem Kontrast beobachtet. Diese Messungen zeigen, dass die Feldtemperatur etwas höher ist als die Temperatur der Resonatorwände.

Zur Präparation Atome in der Rydberg Zustand $61D_{5/2}$ wurde ein neues

Laser-System entwickelt. Die Atome werden aus dem Grundzustand in den Rydberg-Zustand mit einem zweistufigen Diodenlaser Kaskaden Aufbau bei 780 nm und 480 nm angeregt. Die Umsetzung dieses neuen Lasersystems führte zur Entwicklung einer neuen Frequenzstabilisierungs Technik. Diese Arbeit stellt eine neue Methode der Doppler-freien, rein optischen Spektroskopie von *Rb* Rydberg-Zuständen in einer Gaszelle bei Raumtemperatur- vor. Diese neue Methode wird dann in der Spektroskopie für verschiedene Anregungsschemata verwendet. Die Anregung von Rydberg-Zuständen wird durch Beobachtung der Absorption des 780 nm Diodenlasers auf den starken *Rb* D2-Linie gemessen, in einem Schema, das Ähnlichkeiten zur Technik des Elektron-Schelving aufweist. Laserspektroskopie von Rydberg-Übergängen wird gezeigt und damit werden die verschiedenen Lasersysteme frequenzstabilisiert, die die Rydberg-Übergänge in dem Mikromaser Experiment anregen. Es konnte die Qualität dieser Stabilisierung mit einer Atomstrahl Vorrichtung und einem Flugzeit Experiment gemessen werden. Durch die Verwendung unterschiedlicher Laser Polarisationen wird auch die Anregung eines einzelnen Rydberg Hyperfein Zustandes demonstriert.

# Abstract

This thesis reports experiments on the interaction between a two-level atomic system and a single mode of the radiation field of a cavity. The interaction between atoms prepared in the ground state of the two-level atomic system and the quantized thermal cavity field is investigated for the first time in this configuration.

The One-Atom Maser, or Micromaser, is a unique tool for the investigation of quantum aspects of the interaction of radiation and matter. A two-level atomic system of $^{85}Rb$ Rydberg atoms is interacting with a microwave single mode of a high Q cavity. The large dipole matrix-elements of single Rydberg atoms and a superconducting microwave cavity with a Q-factor on the order of $10^{10}$ achieve the strong coupling regime and coherent interaction between the two-level Rydberg atomic system and the cavity field is dominant. The observation of Rabi oscillations and the production of nonclassical field states are, therefore, possible and will be shown in this work.

In the latest Micromaser experiments, the Rabi oscillations, so far measured, exhibit inconsistencies with the theoretical prediction, with a rather low observed contrast. One possible explanation is attributed to higher field temperature. Indirect temperature measurements of the cavity wall are performed by means of external semi-conductors temperature sensors. However no direct field temperature measurements below 1K have been realized yet. The experimental realization of Rabi-oscillations between the ground state of the two-level atomic system and the quantized thermal cavity field at the single photon level gives a direct measurement of the field statistic and the cavity field temperature can be extracted. In this work, experiments with the Rydberg state, $61D_{5/2}$ are realized for the first time. The coherent interaction is demonstrated for both a high atomic pumping leading to the measurement of the first maserlines in this configuration, and a low atomic injection rate, observing Rabi-oscillations with high contrast. These measurements show a slightly higher field temperature than the cavity wall temperature.

To prepare atoms into the Rydberg state $61D_{5/2}$, a new laser system has been developed. The atoms are excited from the ground state into the Rydberg state with a two-step diode laser cascade setup at 780 nm and 480 nm. The

implementation of this new laser system led to the development of a new frequency locking scheme. This thesis presents a new method of Doppler-free, purely optical spectroscopy of *Rb* Rydberg states in a room-temperature gas cell. This new spectroscopy method is then used for different excitation schemes. The excitation of Rydberg states is monitored by observing the absorption of the 780 nm diode laser locked on the strong *Rb* D2 line, in a scheme similar to electron shelving. Laser spectroscopy of Rydberg transition is demonstrated and the frequency stabilization of the different laser systems exciting the Rydberg states used in the Micromaser experiment is achieved. We measure the performance of this stabilization with an atomic beam apparatus and a time of flight experiment. Also, using different polarization schemes, the excitation of a single Rydberg hyperfine state is demonstrated.

# Contents

**1 Introduction** **1**

**2 Theory** **7**
2.1 Basics . . . . . 8
2.2 The Jaynes-Cummings model . . . . . 11
2.3 Micromaser Dynamics and Master Equation . . . . . 16

**3 Experimental Setup** **23**
3.1 Atomic Beam . . . . . 26
3.2 Rydberg Atoms . . . . . 29
3.3 Cavity . . . . . 41
3.4 Cryogenic Environment . . . . . 46

**4 Experiments with Maser Ground State Atoms** **53**
4.1 Magnetic Field Compensation . . . . . 54
4.2 Stark Effect and Velocity Selection by Doppler Effect . . . . . 58
4.3 Maser Line with Ground State Atoms . . . . . 64
4.4 Rabi Oscillations with a Quantized Thermal Field . . . . . 67

**5 Optical Spectroscopy of Rydberg Atoms** **71**
5.1 Weak Transition Detection by Electron Shelving . . . . . 72
5.2 Non-Destructive Spectroscopy of Rydberg Atoms . . . . . 76
5.3 Applications to the Micromaser Experiment . . . . . 84

**6 Quantum Trajectories** **89**
6.1 QTM applied to the Micromaser . . . . . 91
6.2 Micromaser Linewidth and the Phase Diffusion . . . . . 96
6.3 Ramsey Interferences in a Toroidal Cavity . . . . . 100

**Outlook** **107**

**Bibliography** **109**

# List of Figures


2.1 One Atom Maser Experiment . . . . . 8
2.2 Thermal Rabi oscillation with ground state atoms . . . . . 16
2.3 One-Atom-Maser Principle . . . . . 18
2.4 One-Atom-Maser Pumpcurve . . . . . 20

3.1 Experimental Setup . . . . . 25
3.2 Atomic Oven . . . . . 27
3.3 Velocity Distribution . . . . . 28
3.4 Atomic Level Scheme . . . . . 33
3.5 Channeltron Plateau . . . . . 36
3.6 State Selective Detection: Channeltron Box . . . . . 38
3.7 State Selective Detection . . . . . 39
3.8 High Q Niobium Cavity . . . . . 41
3.9 Field Distribution . . . . . 42
3.10 Cavity Frequency Dependence with the Piezo Voltage . . . . . 44
3.11 Frequency and Q-Factor Measurement . . . . . 45
3.12 Cavity Q-factor Measurement . . . . . 46
3.13 Mean Thermal Photon Number Temperature Dependence . . . 47
3.14 $^3He - ^4He$ Dilution Cryostat . . . . . 50

4.1 Magnetic Field Compensation Principle . . . . . 55
4.2 Magnetic Field Compensation Measurement . . . . . 57
4.3 Stark Effect Experiment . . . . . 61
4.4 Time of Flight Experiment . . . . . 62
4.5 Time-of-Flight Measurement with $61D_{5/2}$ Rydberg Atoms . . . . 63
4.6 Stark Effect Frequency Shift . . . . . 64
4.7 Maser Line with $61D_{5/2}$ Ground State Atoms . . . . . 66
4.8 Maser Line with $61D_{5/2}$ Ground State Atoms- Velocity Selected 67
4.9 Thermal Rabi Oscillations with $61D_{5/2}$ Ground State Atoms . . 69

5.1 Atomic Ladder Configuration . . . . . 73
5.2 Experimental Setup for the Blue Laser Spectroscopy . . . . . 74

5.3 Rydberg Spectroscopy with a Two-Steps Excitation Scheme . . 75
5.4 Setup for the Optical Spectroscopy with a 297 nm UV Laser . . 76
5.5 Rydberg Spectroscopy Signal with a 297 nm UV Laser . . . . . 78
5.6 Experimental Setup for the Three-Step Spectroscopy . . . . . 79
5.7 Atomic Level Scheme for the Spectroscopy of the $5D_{5/2}$ State . . 80
5.8 Hyperfine Spectroscopy of the $5D_{5/2}$ State . . . . . 81
5.9 Atomic Level Scheme for the $63P_{3/2}$ Spectroscopy with a Three-Step Diode Laser System . . . . . 82
5.10 Spectroscopy Signal of the $63P_{3/2}$ Rydberg State with a Three-Step Diode Laser System . . . . . 83
5.11 Spectroscopy Signal of the $60F$ Rydberg State with a Three-Step Diode Laser System . . . . . 84
5.12 Doppler-shiffted Signal using the Hyperfine Manyfold of the *Rb* D2 Line . . . . . 86
5.13 Time-of-Flight Spectra . . . . . 87

6.1 Phase Diffusion Constant $D$ . . . . . 97
6.2 Field Displacement in Phase Space and Atomic Statistics . . . . 99
6.3 Phase diffusion of the micromaser field state . . . . . 101
6.4 Torroidal cavity . . . . . 104
6.5 Quantum Ramsey Interferences . . . . . 106

# Chapter 1

# Introduction

The interaction between light and matter can be modeled theoretically by considering matter as a collection of two-level atoms. A dipole transition between two atomic levels then couples to a continuum of modes representing external radiation field.

Spontaneous emission process, postulated by Einstein [1] resulting in the exponential decay of the excited atomic state to a ground state is one of the consequences of this coupling. A quantitative quantum description of spontaneous emission was developed by Weisskopf and Wigner in 1930 [2]. Based on its quantum mechanical description, the environment is represented by a thermal bath consisting of infinitely many oscillators. The coupling of atoms to the thermal bath, which statistics is ruled by the Planck law, induces transitions between the excited state and ground atomic states. Therefore, the Weisskopf-Wigner spontaneous emission theory represents an example of a irreversible process of an open dissipative system.

The second consequence of this coupling is the virtual emission and reabsorption of photon by the atoms leading to the shift of the atomic transition (Lamb shift). It was first observed by Lamb and Retherford while performing microwave spectroscopy experiments with hydrogen atoms [3]. Later on the first theoretical treatment was achieved by Bethe [4]. Nowadays, accurate measurements of the Lamb shift are used to test with very high accuracy the quantum electrodynamic theory [5].

Both effects are also present, when the field of the environment is in its quantum ground state, the vacuum state, meaning no photons are present. The interaction between the atoms and the vacuum field can be explained using the Heisenberg uncertainty relation introducing vacuum fluctuations.

However, the dynamics of the system changes when the two-level atoms are coupled to a single mode of radiation. Coherent interaction between the atoms and the field takes place and reversible processes are possible: the atom emits a

photon in the radiation mode, and reabsorbs it. The frequency of this energy exchange between the two sub-systems is given by the coupling constant $g$, which is proportional to the dipole matrix element. The Jaynes-Cummings Hamiltonian describes this interaction [6].

The starting point of cavity quantum electrodynamics (CQED) where the realization of the coherent interaction between radiation and matter is investigated, can be regarded to Purcell who has suggested one of its principle ideas [7]. In the context of atomic physics, this principle means *the spontaneous emission rate and therefore the lifetime of an atomic state is not an intrinsic property of the atoms and can be modified when the atom is coupled to a resonant electrical circuit.*

Later on Casimir and Polder achieved a rigorous CQED calculation considering the force between an atom and a conductive plate [8]. The emission probability of a photon by an atom at the frequency $\omega_0$ is ruled by Fermi's golden rule and is therefore proportional to the mode-volume of the radiation field at $\omega_0$. In the presence of a conductive structure (hereafter we regard this structure as a cavity), the structure of the free-space modes seen by the atom is altered. If the cavity is resonant with the atoms, the spectral density at $\omega_0$ is higher than in the free-space case and therefore the spontaneous emission rate is increased compared to the free-space one. In the non-resonant case, no energy exchange occurs leading to an enhancement of the lifetime of the excited atomic state.

The most famous applications of the weak coupling where the emission rate is enhanced are the laser and the maser. Each individual atom of a lasing medium couples to the cavity in the weak coupling regime, however, due to the macroscopic number of atoms, stimulated emission occurs, realizing a coherent radiation source.

### The Strong Coupling Regime

In the case of the strong coupling regime, which is qualitatively different from the weak coupling, reversible processes are present and the atomic population oscillates. Strong coupling is achieved when the dipole coupling constant $g$ is larger than the spontaneous atomic decay rate $\kappa$ and the cavity decay rate $\gamma$. The condition $g > \kappa$ leads to a coherent emission of the atom in a well defined single mode and not in the environment. The emitted photon is then trapped in the cavity mode for such a long time, i.e $g > \gamma$, that it can be reabsorbed by the atom after a Rabi cycle $(\pi/g)$. Unitary reversible processes are realized. Periodic oscillation occurs and Rabi oscillations at the frequency $\Omega = \sqrt{n+1}g$ are observed.

The progress achieved over the last decades both for the engineering of

high-Q cavities as well as controlling single atoms has allowed physicists to developed experimental systems where the strong coupling regime is realized in two distinct frequency domains, the microwave and optical one.

Experiments with optical high finesse Fabry-Perrot cavities achieve the realization of the strong coupling regime. The coherent interaction is demonstrated by observing the vacuum Rabi-splitting between the eigenstate of the atom-cavity coupled system [9].

In the recent years, cavity QED experiments based on artificial atoms have been developed both in the microwave and optical regime. Circuit QED with superconductor circuits in the microwave domain [10] or quantum dots structures in optical cavities [11] are some outstanding examples of the development of the field.

In this thesis, the interaction between a single atom and a single mode of a microwave cavity is investigated.

**The One-Atom-Maser or Micromaser**

The first break-through in the realization of strong coupling between the light and matter was achieved with the development of high-Q cavities in the microwave regime. Inspired by the traditional maser, the micromaser experiment has been developed over the last decades at the Max Planck Institute for Quantum Optics by the group of H. Walther [12]. Meanwhile the group of S. Haroche in Paris developed a CQED experiment in the microwave regime based on an open Fabry-Perrot cavity [13]. An advantage of the closed cavity used in Garching is, that it covers the entire $4\ \pi$ solid angle isolating completely the atom from the environment.

In the micromaser, a stream of two-level atoms is injected into a superconducting cavity with a high quality factor. The injection rate is controlled such that at most one atom at a time is present inside the cavity. The cavity decay constant is made small by using a superconductive niobium cavity. The microwave photon energy is smaller than the energy gap of the superconductive $Nb$, thus the photon absorption by the cavity wall is reduced. An other advantage of microwave cavity over optical cavity is their mode structure. Wavelengths are on the order of cm in the former case and therefore the cavity oscillations in the fundamental mode can be realized. It is then possible to set the atom at the maximum of the field distribution. In the optical regime, higher modes have to be used and therefore the coupling constant is strongly dependent of the atom position in the cavity.

In contrast to the traditional maser, where a macroscopic molecular ensemble interacts with the cavity field, the micromaser studies the radiation-matter interaction at the single atom level. This implies that the atom-cavity coupling

must be larger than the atomic spontaneous decay rate. The latter condition has been fulfilled using highly excited atoms, Rydberg atoms. Their properties make them ideal for the micromaser. The transition between two neighboring Rydberg states is in the microwave domain. The dipole matrix element for the transition between Rydberg levels scales with $n^2$, where $n$ is the main quantum number, and is three orders of magnitude larger than for Zeeman or hyperfine transitions. Consequently, a few photons are enough to saturate the transition between neighboring levels. The spontaneous decay rate to the ground state scales with $n^{-3}$ and is therefore much smaller than the coupling constant $g$. Finally, the atoms in the micromaser play a dual role as the measurement of the cavity field is performed in an indirect manner, measuring the atomic statistics. In the micromaser experiment, $^{85}Rb$ atoms are used. The maser excited state is the $63P_{3/2}$ state and the maser ground state the $61D_{5/2}$. The transition frequency is 21.456 GHz, the coupling constant, $g/2\pi \sim 7$ kHz. The atomic decay rate $\gamma/2\pi = 0.7$ kHz and the cavity decay rate $\kappa/2\pi \sim 13$ Hz. The condition $g >> \kappa, \gamma$ for the strong coupling is then fulfilled.

In the micromaser experiment realized in Garching, the strong coupling regime is achieved and the coherent interaction between a single Rydberg atom and a single mode of the microwave radiation of a high-Q superconductive $Nb$ closed cavity is examined. The atoms prepared in the excited state enter the cavity and interact with the resonant field allowing the investigation of many fundamental aspects in quantum optics. For a large atomic injection rate, the combination of the coherent interaction when an atom is present in the cavity and decay processes lead to a steady state of the field, analogous to a maser [14]. The photon statistics of the micromaser then exhibits many interesting effects including sub-Poissonian statistics. Photon number states can be generated [15] and bistability has been observed [16]. For a low atomic injection rate, with less than one atom per cavity decay time, the realization of Rabi oscillations between the nonclassical field of the cavity and the two-level Rydberg atom is possible.

## This Thesis

### First Experiments with the Maser Rydberg Ground State $61D_{5/2}$

In the micromaser experiments at low temperature (below 1K), the Rabi oscillations, so far measured, exhibit inconsistencies with the theoretical prediction, with a rather low observed contrast. One possible explanation is attributed to higher field temperature. The control of the thermal field is one of the important challenges in the micromaser physics. The mean thermal photon number plays a central role in the steady state properties of the cav-

ity. Especially for the generation of photon number states, trapping states, or for the study of stochastic processes where the noise is at the quantum level, quantum stochastic resonances. The cavity is cooled using a dilution cryogenic system reaching temperature below 1 K. However, heating due to outside radiation from hotter surfaces present in the experimental apparatus could be significant. One of the scopes of this work is to measure, for the first time, the field temperature in a more accurate way using the micromaser ground state atoms as temperature sensors. When no atoms are present, the cavity is in thermal equilibrium and the field statistic is governed by the Planck law and the photon distribution is described by the Bose-Einstein distribution. The measurement of Rabi oscillations where a ground state atom interacts with the quantized thermal field of the cavity then give information about the photon distribution and the temperature of the field can be extracted.

**Development of a new Laser System and Demonstration of a new Method of Purely Optical Spectroscopy of Rydberg Atoms**

To perform thermal Rabi oscillation measurements, a new laser system had to be developed to prepare the Rydberg atoms in the maser ground state. This is achieved by two diode lasers at 780 nm and 480 nm. The implementation of this new laser system led to the development of a new frequency locking scheme for the laser promoting the atoms to the Rydberg states. So far, the spectroscopic signal used for the frequency locking was acquired from experiments performed on the atomic beam. Purely optical detection of Rydberg states has been a difficult task for many years, mostly due to the small radial part of the dipole matrix element between the atomic ground state and the highly excited Rydberg states. On the other hand, weak atomic transition are of particular interest as they offer the highest frequency resolution. Over the last decades, frequency standard experiments developed the detection of weak atomic transition in optical atomic clocks [17, 18] using the quantum amplification of the electron-shelving technique introduced by Dehmelt [19]. One of the results of this thesis is the demonstration of a new method of Doppler-free purely optical spectroscopy of Rydberg atoms in a room-temperature gas cell applying the quantum amplification of the electron shelving to Rydberg systems and its direct application in the micromaser experiment for a frequency locking scheme [20, 21].

The development of this new excitation scheme and the injection of ground state atoms inside the cavity opens the possibility for a range of new experiments with new atomic states. Maser lines, where the cavity frequency is tuned over resonance, are measured with ground state atoms for the first time. And thermal Rabi oscillations are observed at the single-thermal-photon level.

From the measured Rabi oscillations it can be deduced that the actual field temperature is slightly higher than expected.

**Numerical Support for Time Dependent Micromaser Experiments**

Parallel to the realization of maser ground states atoms experiments, I developed a theoretical and numerical support for the ongoing micromaser experiments in Garching. The steady state of the micromaser can be solved analytically. Nevertheless, there are no analytical solutions for time dependence of the fields. The phase diffusion experiment investigates the time evolution of the phase and amplitude of the maser field to determine the micromaser linewidth. Hence, numerical solutions for decoherence processes in the micromaser are developed using the quantum trajectory treatment.

**Chapters Organization**

Chapter 2 presents an introduction to the theory of the micromaser. The Jaynes-Cummings interaction is investigated and the case of Rabi oscillations between a ground state and a thermal field is solved. The analytical treatment of the micromaser in the steady state regime is also considered.

In the third chapter, the main experimental aspects for the realization of the micromaser experiments are described. Rydberg atoms and their main properties are discussed, as well as the latest improvement of the cryogenic system for a better temperature control over a wild range.

Chapter 4 presents the main results obtained when ground states atoms interact with the micromaser cavity at thermal equilibrium.

The new Doppler-free optical detection method, for the spectroscopy of Rydberg states in a gas cell at room-temperature is demonstrated in the fifth chapter.

Finally, Chapter 6 examines the numerical treatment of the micromaser using the Quantum Trajectory Method. The cases of the phase diffusion and quantum Ramsey interferences are presented

# Chapter 2

# Theory

*In this chapter, the Jaynes-Cummings Hamiltonian, describing the coherent interaction between a two-level system and a single mode of radiation field, is introduced. The particular case of the interaction between the lower level and the quantized thermal field of the cavity (experimentally investigated in Chapter 4) is analytically solved. Finally, the micromaser steady state is calculated when Rydberg atoms are injected into the cavity, both in the excited and the ground maser state.*

An article by Purcell [7] can be considered as the first proposal in the field which is nowadays well-known as cavity quantum electrodynamics (CQED). In this work it is enunciate that the spontaneous emission rate of an atomic frequency transition, compared to the free space rate, can be enhanced by coupling an atom to a resonant electric circuit. Later on Casimir and Polder [8] presented a rigorous CQED calculation considering the force between an atom and a conducting plane.

In presence of a conducting structure (hereafter we regard this structure as a cavity), the free-space field modes distribution is modified and the cavity can enhance the coupling of the atoms to some particular modes of the electromagnetic field. In this case the spontaneous decay rate of an excited atomic state can be different from the free-space one. Demonstrations of the modified radiation rates in the case of low-Q cavities have been done in the microwave [22] and the visible [23] regime.

In the case of the interaction of an atom with a high-Q cavity, qualitatively different from the low-Q cavity, reversible processes are present and the atomic population oscillates. The discovery of high-Q microwave cavities in the early 80s [12, 13] allowed to study the fundamental case where a single two-level atomic system interacts with a single mode of a cavity [24] which leads later to the realization of the one-atom-maser or micromaser.

In this chapter the theoretical model of the micromaser is introduced. The quantum nature of the steady state of the cavity field is shown and the particular case of the Rabi oscillations of ground state atoms in presence of a thermal field at the quantum level is discussed.

## 2.1 Basics

The one-atom maser or micromaser is a unique tool which allows to study the atom-field interaction in the particular case where a single two-level atomic system interacts with a single mode of a quantized field.

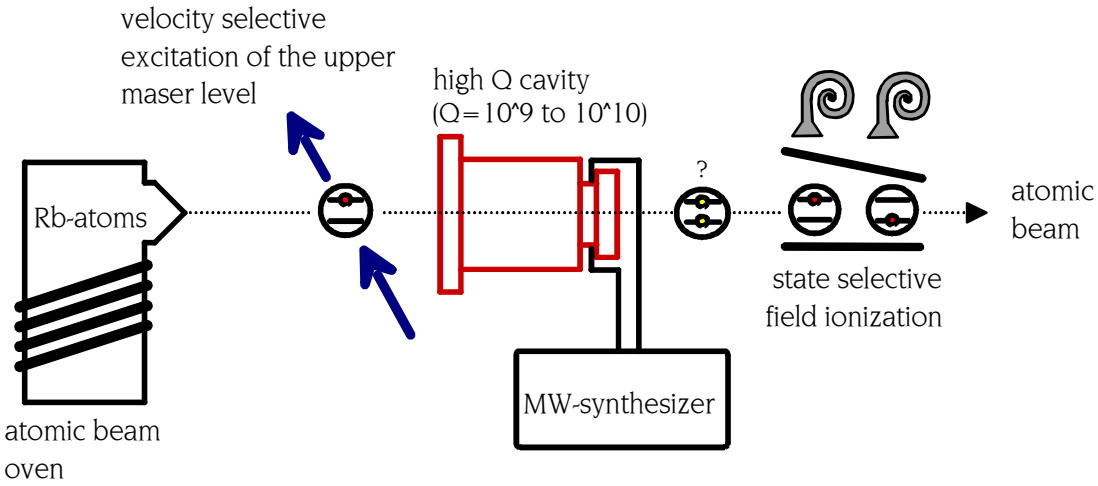


Figure 2.1: *The One-Atom-Maser or micromaser experiment. The heart of the experiment: a very high Q cavity is designed to isolate a single mode of microwave radiation. A thermal Rydberg Rb atomic beam interacts with the field in a coherent manner. The dilute atomic beam, ensuring that only one atom at a time is interacting with the field, is produced from an oven and the Rydberg states are produced by laser excitation before entering the cavity. The field measurement is achieved in an indirect way while the atomic state after the interaction is measured using a state-selective ionization detection scheme. The atom-cavity interaction time is controlled using angular excitation of the laser beam by means of Doppler selection.*

The atoms are injected in the cavity at such a low rate that at most one

atom at a time is present in the cavity. In the case of the micromaser we have to deal with an open quantum system under further assumptions:

- Atom-field interaction involves only one mode of the field and a two-level Rydberg atom with the ground maser level $|g\rangle$ as the $61D_{\frac{5}{2}}$ state and the excited maser level $|e\rangle$ the $63P_{\frac{3}{2}}$ state of the $^{85}Rb$ atom. Due to the cavity geometry only one mode is near resonant.

- The atom-field interaction time $\tau$ is controlled via Doppler selection of the velocity of the atoms in the excitation scheme.

- The coupling $g$ of the atom to the field is much stronger than the coupling between the atom or the cavity to the environment ($\gamma$ and $\kappa$ ): the micromaser operates in the strong coupling regime.

- The atom-field interaction is a dipole-dipole coupling between a single mode of a field and two well-known Rydberg states of the atoms.

In order to describe the dynamics of the mircomaser, the description of the electromagnetic field of the cavity has to be outlined first. From the Maxwells equations (in MKS unit) restricted to a charge-free (e.g. vacuum), isotropic and homogenous media:

$$\nabla.\mathbf{E} = 0 \tag{2.1}$$
$$\nabla.\mathbf{H} = 0 \tag{2.2}$$
$$\nabla \times \mathbf{H} - \epsilon_0 \dot{\mathbf{E}} = 0 \tag{2.3}$$
$$\nabla \times \mathbf{E} + \mu_0 \dot{\mathbf{H}} = 0 \tag{2.4}$$

Consider the electric field $\mathbf{E}$(r,t) and magnetic field $\mathbf{H}$ inside a volume V bounded by a surface S of perfect conductivity. $\mathbf{E}$ and $\mathbf{H}$ can be decomposed in terms of two sets of orthogonalized and normalized vector fields (modes) $\mathbf{E}_a$ and $\mathbf{H}_a$ .
These sets $\mathbf{E}_a$ and $\mathbf{H}_a$ obey to the Slater relations [25] :

$$k_a\mathbf{E}_a = \nabla \times \mathbf{H}_a \tag{2.5}$$
$$k_a\mathbf{H}_a = \nabla \times \mathbf{E}_a \tag{2.6}$$

From the wave equations (2.5) and (2.6), one recovers the Helmotz equations for $\mathbf{E}_a$ and $\mathbf{H}_a$ :

$$\nabla^2 \mathbf{E}_a + k_a^2 \mathbf{E}_a = 0 \tag{2.7}$$
$$\nabla^2 \mathbf{H}_a + k_a^2 \mathbf{H}_a = 0 \tag{2.8}$$

By using the separation of variables, the total resonator fields, $\mathbf{E}(r,t)$ and $\mathbf{H}(r,t)$, can then be decomposed as:

$$\mathbf{E}(\mathbf{r},t) = -\sum_a \frac{1}{\sqrt{\epsilon_0}} p_a(t)\, \mathbf{E}_a(\mathbf{r}) \tag{2.9}$$
$$\mathbf{H}(\mathbf{r},t) = \sum_a \frac{1}{\sqrt{\mu_0}} \omega_a q_a(t)\, \mathbf{H}_a(\mathbf{r}) \tag{2.10}$$

with $\omega_a = k_a/\sqrt{\mu_0\epsilon_0}$. Using the Maxwell equations and the Slater relations leads to the relations for $p_a$ and $q_a$:

$$\begin{aligned} p_a &= \dot{q}_a \\ \omega_a^2 q_a &= -\dot{p}_a \end{aligned} \tag{2.11}$$

In order to find a model for the quantization of a field in a cavity, we start by writing down the total energy of the field inside the cavity. The Hamiltonian of the system is:

$$H = \frac{1}{2}\int_v \mu_0\, \mathbf{H}.\,\mathbf{H} + \epsilon_0\, \mathbf{E}.\,\mathbf{E}\, dv \tag{2.12}$$

Replacing $\mathbf{E}(r,t)$ and $\mathbf{H}(r,t)$ by their expressions obtain in (2.9) and (2.10) gives:

$$H = \sum_a \frac{1}{2}(p_a^2 + \omega_a^2 q_a^2) \tag{2.13}$$

From the relations between $p_a$ and $q_a$ (2.11) obtained from the Maxwell' equations we see that $p_a$ and $q_a$ constitute a canonically conjugate pair and are solutions of the Hamiltons equations of motion relating $\dot{q}_a$ to $p_a$ and $\dot{p}_a$ to $q_a$.

The quantization of the electromagnetic field is then achieved by considering $p_a$ and $q_a$ as formally equivalent to the momentum and coordinate operator of a quantum mechanical oscillator. They then obey to the commutator relations:

$$\begin{aligned} [p_a, p_b] &= [q_a, q_b] = 0 \\ [p_a, q_b] &= i\hbar\delta_{a,b} \end{aligned} \tag{2.14}$$

We introduce at this point the creation operator $a_b^\dagger$ and the annihilation operator $a_b$ by:

$$a_b^\dagger(t) \;=\; \left(\frac{1}{2\hbar\omega_b}\right)^{\frac{1}{2}} \left[\omega_b\, q_b(t) \;-\; i\, p_b(t)\right] \tag{2.15}$$

$$a_b(t) \;=\; \left(\frac{1}{2\hbar\omega_b}\right)^{\frac{1}{2}} \left[\omega_b\, q_b(t) \;+\; i\, p_b(t)\right] \tag{2.16}$$

From (2.15) and (2.16) we find directly the commutator relations to be:

$$\begin{aligned} [a_a, a_b] \;&=\; [a_a^\dagger, a_b^\dagger] \;=\; 0 \\ [a_a, a_b^\dagger] \;&=\; \delta_{a,b} \end{aligned} \tag{2.17}$$

Replacing the operator $p$ and $q$ by the operator $a$ and $a^\dagger$ in (2.14), the Hamilton operator of a quantum field reads:

$$\widehat{H} \;=\; \sum_b \hbar\,\omega_b (a_b^\dagger a_b \;+\; \frac{1}{2}) \tag{2.18}$$

## 2.2 The Jaynes-Cummings model

To describe the interaction between the atoms and the cavity field, we have to use the well-known Jaynes-Cummings Hamiltonian[6]. It deals with the case when a single mode of a quantized electromagnetic field couples to a two-level system.

In the case of the micromaser experiment, the two-level system is formed by the Rydberg atomic states where the ground maser level $|g\rangle$ is the $61D_{5/2}$ state and the excited maser level $|e\rangle$ the $63P_{3/2}$ state of the $^{85}Rb$ atom.

The Hamiltonian $H_A$ of the atomic system can so be written as,

$$H_A = \frac{1}{2}\hbar\omega_A(\sigma^\dagger\sigma - \sigma\sigma^\dagger) \tag{2.19}$$

The energy gap between the two levels is $\omega_A$. The transition between the two atomic states is described by the operators $\sigma = |g\rangle\langle e|$ and $\sigma^\dagger = |e\rangle\langle g|$. These operators satisfy the fermionic anticommutation relation:

$$[\sigma, \sigma^\dagger]_+ = \sigma\sigma^\dagger + \sigma^\dagger\sigma = 1 \tag{2.20}$$

and the commutator reads:

$$[\sigma, \sigma^\dagger] = |e\rangle\langle e| - |g\rangle\langle g| = \sigma_z \tag{2.21}$$

This comes to a simple expression for the atom Hamiltonian:

$$H_A = \frac{1}{2}\hbar\omega_A\sigma_z \tag{2.22}$$

In the same way one can rewrite the position operator $\vec{r}$ of the electron to the nuclei in the $|e\rangle$ ,$|g\rangle$ basis. Under the assumption that the atom has no permanent dipole moment and that the matrix element are real, we have $\langle g|\vec{r}|e\rangle = \langle e|\vec{r}|g\rangle$ so,

$$\begin{aligned}\vec{r} &= |g\rangle\langle g|\vec{r}|e\rangle\langle e| + |e\rangle\langle e|\vec{r}|g\rangle\langle g| \\ &= (\sigma + \sigma^\dagger)\langle e|\vec{r}|g\rangle\end{aligned} \tag{2.23}$$

As the atomic transition is only resonant for one mode of the cavity field, the field Hamiltonian can be written as,

$$H_F = \frac{1}{2}\hbar\omega_F(a^\dagger a + \frac{1}{2}) \tag{2.24}$$

The quantum electric field along the atomic beam axis reads:

$$\hat{\vec{E}}(\vec{x}) = \frac{E_0}{\sqrt{2}}(a^\dagger + a)\sin(k\cdot z) \tag{2.25}$$

where we assume that the field has a linear polarization along the x-axis and $\vec{k} \parallel \vec{z}$, with $k = \frac{\omega_F}{c}$ and $\omega_F$ the cavity frequency .

Assuming that the wavelength of the field is large compared to the dimension of the Rydberg atoms, the interaction of the atom with the cavity field can be described in a good approximation with the dipole approximation. The interaction Hamiltonian $H_{AF}$ can then be written as:

$$H_{AF} = -e\vec{r}.\vec{E}(\vec{r}) \tag{2.26}$$

With (2.23) and (2.25), $H_{AF}$ reads:

$$H_{AF} = \hbar g(\sigma^\dagger + \sigma)(a^\dagger + a) \tag{2.27}$$

Where $g$ [26] is the coupling constant:

$$g = -e\frac{\langle g|x|e\rangle}{\hbar}E_0\sin(k\cdot z) \tag{2.28}$$

(2.27) has four different operators products which can be physically interpreted:

- $a\sigma$ corresponds to a photon absorption with the atomic transition $|e\rangle \rightarrow |g\rangle$, which corresponds to a loss of the total energy of the system.

- $a\sigma^\dagger$ corresponds to the stimulated absorption.

- $a^\dagger\sigma$ corresponds to the stimulated emission.

- $a^\dagger\sigma^\dagger$ corresponds to a photon emission with the atomic transition $|g\rangle \rightarrow |e\rangle$, which corresponds to a gain of energy for the system.

Let us transform the atom-field Hamiltonian $H_{AF}$ in the Heisenberg representation.

$$H_{AF} = \hbar g(ae^{-i\omega_F t} + a^\dagger e^{i\omega_F t})(\sigma^\dagger e^{-i\omega_A t} + \sigma e^{i\omega_A t}) \tag{2.29}$$

$$H_{AF} = \hbar g(a\sigma e^{-i(\omega_F+\omega_A)t} + a^\dagger\sigma^\dagger e^{i(\omega_F+\omega_A)t} + a^\dagger\sigma e^{i(\omega_F-\omega_A)t} + a\sigma^\dagger e^{-i(\omega_A-\omega_F)t}) \tag{2.30}$$

If we integrate the Schrödinger equation in the Heisenberg representation we get two oscillations terms:

1) a fast oscillation term $\approx \frac{1}{\omega_F+\omega_A}$

2) a slow oscillation term $\approx \frac{1}{\omega_F-\omega_A}$

As the slow term is dominant, we can neglected the fast one; this is called the rotating wave approximation. The expression of the atom-field Hamiltonian is in this approximation:

$$H_{AF} = \hbar g[a\sigma^\dagger e^{-i(\omega_F-\omega_A)t} + a^\dagger\sigma e^{i(\omega_F-\omega_A)t}] \tag{2.31}$$

The neglected terms can lead to the Bloch-Zieget shift in the $2^{nd}$ order of the perturbation theory [27].

$H_{AF}$ describes the Jaynes-Cummings interaction by finite detuning:

$$\Delta = \omega_F - \omega_A$$

from the field respect to the atomic transition.
The complete Hamiltonian of the system can then be written as:

$$\begin{aligned} H_{JC} &= H_{AF} \\ &= \hbar g(a\sigma^\dagger e^{-i\Delta t} + a^\dagger\sigma e^{i\Delta t}) \end{aligned} \tag{2.32}$$

This is the Jaynes-Cummings Hamiltonian. The new quantum state of the system is the tensor product between the field state and the atom state.

$$|i, n\rangle = |i\rangle \otimes |n\rangle, \text{where } |i\rangle \in \{|g\rangle, |e\rangle\} \tag{2.33}$$

The Jaynes-Cummings model can then be briefly summarized as follows:

- It is a fully quantum model describing the interaction between a two-level atomic system and the single mode of a quantized electromagnetic field by the means of the Hamiltonian (2.32).

- It is based on two approximations, namely the dipole approximation and the rotating-wave approximation.

Having now this Hamiltonian at our disposal we can start to look closer to the evolution of an atom-field system. Starting with an initial state where the atom is in his ground state $|g\rangle$ and the cavity in a number state $|n+1\rangle$:

$$\Psi(0) = |g, n+1\rangle \tag{2.34}$$

After a time $\tau$, the wave function is:

$$\Psi(\tau) = C_{g,n+1}(\tau)|g, n+1\rangle + C_{e,n}(\tau)|e, n\rangle \tag{2.35}$$

with the Schrödinger equation thus,

$$\begin{aligned}\dot{\Psi}(\tau) &= \dot{C}_{e,n}(\tau)|e, n\rangle + \dot{C}_{g,n+1}(\tau)|g, n+1\rangle \\ &= -ig(a\sigma^\dagger e^{-i\Delta\tau} + a^\dagger\sigma e^{i\Delta\tau})(C_{e,n}(\tau)|e, n\rangle + C_{g,n+1}(\tau)|g, n+1\rangle)\end{aligned} \tag{2.36}$$

if we projet on $|g, n\rangle$ and $|e, n-1\rangle$ we get:

$$\dot{C}_{e,n}(\tau) = -ig\sqrt{n+1}e^{-i\Delta\tau}C_{g,n+1}(\tau) \tag{2.37}$$

and,

$$\dot{C}_{g,n+1}(\tau) = -ig\sqrt{n+1}e^{i\Delta\tau}C_{e,n}(\tau) \tag{2.38}$$

If there is no detuning ($\Delta = 0$) of the cavity to the atomic transition, with the initial condition, we get:

$$C_{g,n+1}(\tau) = \cos(g\sqrt{n+1}\tau) \tag{2.39}$$

and

$$C_{e,n}(\tau) = -i\sin(g\sqrt{n+1}\tau) \tag{2.40}$$

We can write so the probabilities $P_{|g,n\rangle}$ and $P_{|e,n-1\rangle}$ to observe the states $|e,n\rangle$ and $|g,n+1\rangle$,

$$\begin{aligned} P_{|g,n+1\rangle}(\tau) &= |\langle g,n+1||\Psi\rangle|^2 \\ &= \cos^2(g\sqrt{n+1}\tau) \end{aligned} \tag{2.41}$$

and,

$$\begin{aligned} P_{|e,n\rangle}(\tau) &= |\langle e,n||\Psi\rangle|^2 \\ &= \sin^2(g\sqrt{n+1}\tau) \end{aligned} \tag{2.42}$$

This describes the reversible emission of the atoms, this behavior is the quantum mechanical version of the Rabi oscillations where a two-level atom coupled to a single mode electromagnetic field cavity alternately absorbs photon(s) from the cavity mode and reemits them.

Figure 2.2 shows theoretical simulations for Rabi oscillations where the atom is initially in his ground state $|g\rangle$ and the cavity in a well defined thermal state:

$$\rho_{th} = \sum_n \frac{\langle n\rangle_{th}^n}{(1+\langle n\rangle_{th})^{n+1}} |n\rangle\langle n| \tag{2.43}$$

Hence, the ground state atomic population oscillates as:

$$P_g = \sum_{n=0} \rho_{n,n} \cos^2(\sqrt{n} g\tau) \tag{2.44}$$

For the calculations, the experimental parameters were chosen, like the atom-field coupling constant $g/2\pi = 7$ kHz and the interaction time $\tau$. The experimental realization of such oscillations will be shown in Chapter 4.

The observation of the Rabi oscillations between the two atomic states where the atoms are initially in their excited state $|e\rangle$ has been done experimentally for an initial thermal state of the cavity [28] such as for number state ($n$=0,1,2) inside the cavity [29][30]. The measurement of Rabi oscillation also gives valuable information for a state reconstruction of the quantum field of the cavity [31]

We can finally make the remark that the sates $|e,n\rangle$ and $|g,n+1\rangle$ are not the eigenvalues of the Hamiltonian. We introduce the so-called "dressed states" which are the eigenvalues of the Jaynes-Cummings Hamiltonian [32]:

$$|n,\alpha\rangle = \cos\theta_n |e,n\rangle - \sin\theta_n |g,n+1\rangle \tag{2.45}$$

and,

$$|n,\beta\rangle = \sin\theta_n |e,n\rangle + \cos\theta_n |g,n+1\rangle \tag{2.46}$$

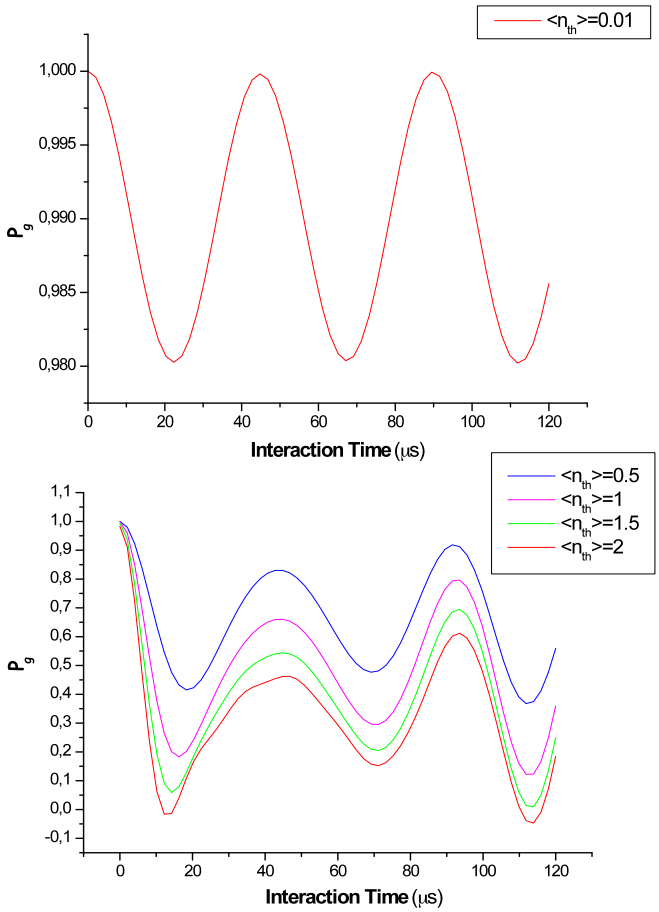


Figure 2.2: *Rabi oscillations between a quantized thermal field and ground state atoms.*

with the mixing angle

$$\tan(2\theta_n) = \frac{2\sqrt{n+1}g}{\omega_F - \omega_A} \tag{2.47}$$

## 2.3 Micromaser Dynamics and Master Equation

In the previous section, the coherent interaction of a two-level atomic sys-

| | | |
|---|---|---|
| Upper Maser State | $\|e\rangle$ | $63P_{3/2}$ |
| Lower Maser State | $\|g\rangle$ | $61D_{5/2}$ |
| Resonance frequency | $\frac{\omega_A}{2\pi} = \frac{\omega_F}{2\pi}$ | 21.456 GHz |
| Atom-Field coupling | $g/2\pi$ | $\approx 7$ kHz |
| Q-factor | $Q = \omega_F/\gamma = \omega_F\tau_c$ | $1.10^9...4.10^{10}$ |
| Atomic decay | $\kappa/2\pi$ | $\approx 0.2$ kHz |
| Interaction time | $\tau$ | 35...120 $\mu$s |
| Temperature | T | 0.15...1.3 K |

Table 2.1: *Main Micromaser parameters*

tem and the single mode of an electromagnetic field in a cavity is described by the Jaynes-Cummings Hamiltonian (2.32).

The cavity is now also interacting with the environment which causes the decay of the field. To describe this interaction, one assumes the coupling between the single mode of the cavity and a thermal bath consisting of a infinitely many oscillators of the environment.
The thermal bath is described by:

$$H_B = \hbar \sum_k \omega_F^k (b_k^\dagger b_k + \frac{1}{2}) \tag{2.48}$$

Using the same algebra as in section 2.2, the Hamiltonian describing the coupling between the cavity and the environment reads:

$$W = \hbar \sum_k g_k (a_k^\dagger b_k + a_k b_k^\dagger) \tag{2.49}$$

In the micromaser, one has to deal with an open quantum system which can be described as follows:

- One atom events: the standard experimental operation is when all atoms are uncorrelated: they arrive at random time and there is at most only one atom in the cavity at any time

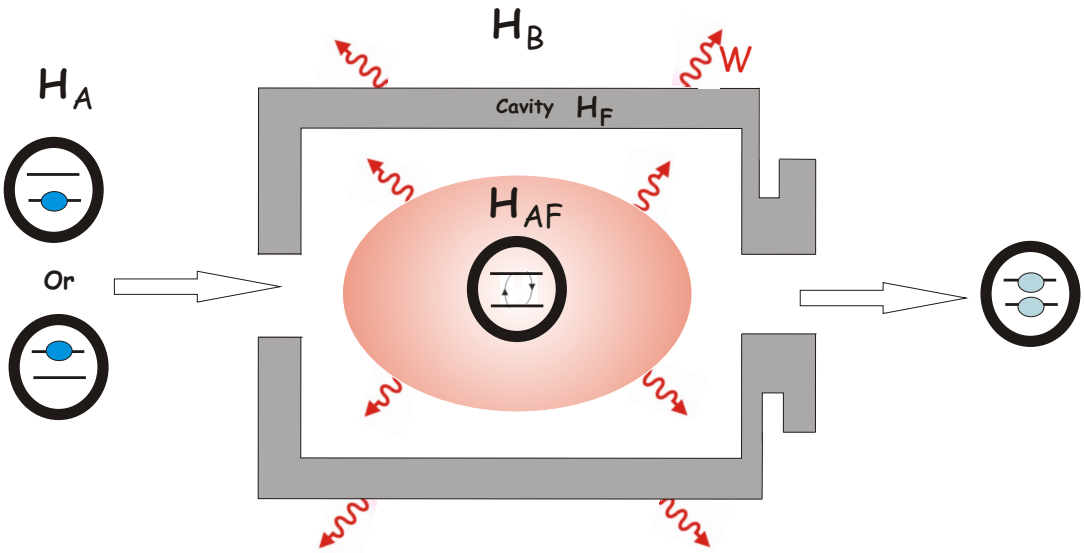


Figure 2.3: *One-Atom-Maser Principle. A single mode of a high Q cavity, $H_F$, interacts with a two-level atomic system, $H_A$. The atoms are injected inside the cavity either in the excited state $|e\rangle$ or ground state $|g\rangle$. When an atom is present in the cavity, the strong coupling regime is achieved and the coherent interaction between the cavity and the atoms occurs, $H_{AF}$. The measurement of the cavity state is done by performing the detection of the atomic state population leaving the cavity. When no atoms are present, the cavity couples to the environment, $H_B$, through the interaction $W$.*

- Leakage of the cavity field: since the lifetime of the photon in the cavity is much more larger ($\gamma/2\pi \approx 20$ Hz ) than the interaction time when an atom is present ($35\,\mu\text{s} < \tau < 100\,\mu\text{s}$), we can neglect a dissipation of the cavity during the interaction. Indeed, we assume that the cavity decays only in the time interval between two atoms.

- Atom-field interaction: when an atom enter the cavity, the atom-field system realizes the Jaynes-Cummings Model.

Under these assumptions, one can formulate an analytical model for the

micromaser [14, 33]. Considering the micromaser dynamics as two separable terms, namely a pumping process of the cavity field in presence of the atoms and a relaxation process when no atoms are present the time evolution of the field reads:

$$\frac{\partial \rho}{\partial t} = \left(\frac{\partial \rho}{\partial t}\right)_{gain} + \left(\frac{\partial \rho}{\partial t}\right)_{loss} \tag{2.50}$$

The decay of the cavity is modeled by the interaction W (2.49) coupling the single mode of the cavity to an external thermal bath. This model has a standard description and its evolution is given by the mean of the master equation of a damped harmonic oscillator [34] :

$$\begin{aligned}\left(\frac{\partial \rho}{\partial t}\right)_{loss} &= \mathcal{L}\rho \\ &= -\frac{1}{2}\gamma(n_{th}+1)(a^\dagger a\rho - 2a\rho a^\dagger + \rho a^\dagger a) \\ &\quad -\frac{1}{2}\gamma n_{th}(a^\dagger a\rho - 2a\rho a^\dagger + \rho a^\dagger a)\end{aligned} \tag{2.51}$$

where $n_{th} = (e^{\frac{\hbar\omega}{k_B T}})^{-1}$ is the mean thermal photon number. Here the evolution operator $\mathcal{L}$ is called the Liouvillian operator.

The pump process is assimilated to the atom field interaction. Starting from the Jaynes-Cummings Hamiltonian (2.32) the unitary evolution operator $\mathcal{U}(\tau)$ reads:

$$\begin{aligned}\mathcal{U}(\tau) &= e^{-(i/\hbar)H_{JC}\tau} \\ &= \cos\left(g\tau\sqrt{a^\dagger a+1}\right)|e\rangle\langle e| + \cos\left(g\tau\sqrt{a^\dagger a+1}\right)|g\rangle\langle g| \\ &\quad - i\frac{\sin\left(g\tau\sqrt{a^\dagger a+1}\right)}{\sqrt{a^\dagger a+1}}a|e\rangle\langle g| - i\frac{\sin\left(g\tau\sqrt{a^\dagger a}\right)}{\sqrt{a^\dagger a}}a^\dagger|g\rangle\langle e|\end{aligned} \tag{2.52}$$

The change of the cavity per atom is given by:

$$\delta\rho = \rho(t_o+\tau) - \rho(t_0) \tag{2.53}$$

where $\rho(t_0+\tau)$ can be expressed as:

$$\begin{aligned}\rho(t_0+\tau) &= Tr_a\{\mathcal{U}^\dagger(\tau)\rho_{a+f}(t_0)\mathcal{U}(\tau)\} \\ &= \mathcal{A}\rho + \mathcal{B}\rho\end{aligned} \tag{2.54}$$

with,

$$\begin{aligned}\mathcal{A}\rho = P_e(t_0)\cos\left(g\tau\sqrt{a^\dagger a+1}\right)\rho(t_0)\cos\left(g\tau\sqrt{a^\dagger a+1}\right) + \\ P_e(t_0)a^\dagger\frac{\sin\left(g\tau\sqrt{a^\dagger a+1}\right)}{\sqrt{a^\dagger a+1}}\rho(t_o)\frac{\sin\left(g\tau\sqrt{a^\dagger a+1}\right)}{\sqrt{a^\dagger a+1}}a\end{aligned} \tag{2.55}$$

$$\mathcal{B}\rho = P_g(t_0)\cos\left(g\tau\sqrt{a^\dagger a}\right)\rho(t_0)\cos\left(g\tau\sqrt{a^\dagger a}\right) + P_g(t_0)a\frac{\sin\left(g\tau\sqrt{a^\dagger a}\right)}{\sqrt{a^\dagger a}}\rho(t_o)\frac{\sin\left(g\tau\sqrt{a^\dagger a}\right)}{\sqrt{a^\dagger a}}a^\dagger \tag{2.56}$$

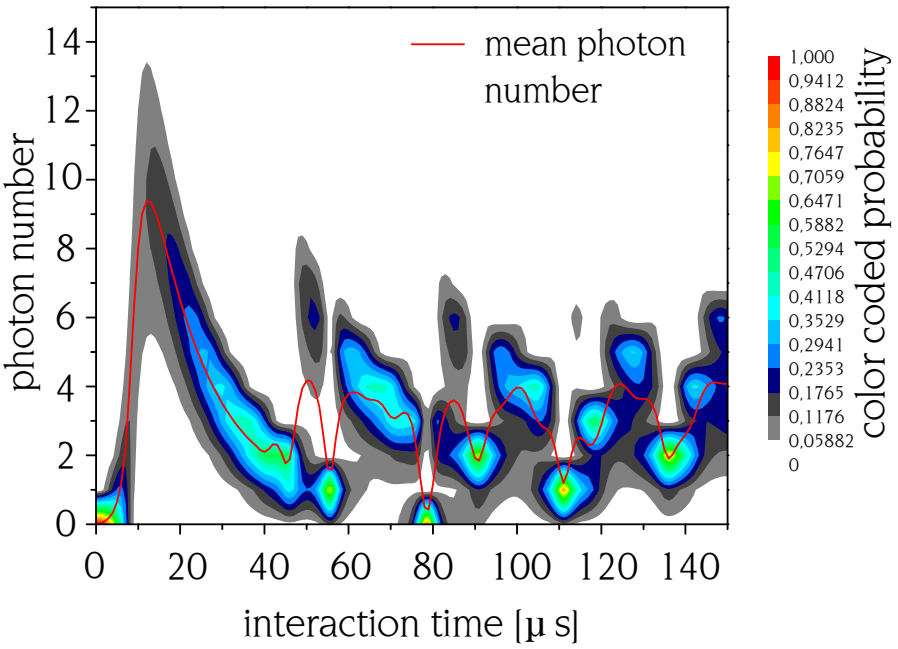


Figure 2.4: *One-Atom-Maser Pumpcurve: the red line represents the mean photon number of the cavity. Around the mean photon number, photon field states with sub-Poissonian statistic are present. In particularly, bistability can be observed for an interaction time $\tau = 57\mu s$. The marked depth show the presence of trapping state, Fock states, produced in the cavity*

In order to get only the time evolution of the cavity field, we have traced over the atomic state and $P_e(t_0)$ and $P_g(t_0)$ are the probabilities that the atom enters either in the excited or ground state. Hence the overall change of the cavity field due to the interaction with the atomic beam reads:

$$\Delta\rho = \mathcal{R}\Delta t(\rho(t_0+\tau) - \rho(t_0)) \tag{2.57}$$

The gain term in the master equation can then be written as follows:

$$\left(\frac{\partial\rho}{\partial t}\right)_{gain} = \mathcal{R}(\mathcal{A}+\mathcal{B}-1)\rho \tag{2.58}$$

where $\mathcal{R}$ is the atomic beam rate - number of atoms per cavity decay time. Substituting (2.49) and (2.56) in the master equation (2.48) leads to the general micromaser master equation:

$$\frac{\partial\rho}{\partial t} = \mathcal{R}(\mathcal{A}+\mathcal{B}-1+\mathcal{L})\rho \tag{2.59}$$

This equation describes an open driven quantum system and can be solved in the steady-state regime when the gains are equal to the losses, $\frac{\partial\rho}{\partial t} = 0$ . The resulting equation leads to the following recursion:

$$\rho_{nn} = \frac{n_{th}\gamma + \mathcal{E}_k}{(n_{th}+1)\gamma + \mathcal{G}_k}\rho_{n-1} \tag{2.60}$$

The steady-state solution $\rho_{nn}^{ss}$ reads:

$$\rho_{nn}^{ss} = \rho_{00}^{ss}\prod_{k=1}^{n}\frac{n_{th}\gamma + \mathcal{E}_k}{(n_{th}+1)\gamma + \mathcal{G}_k} \tag{2.61}$$

with the coefficients:

$$\mathcal{E}_k = \frac{\mathcal{R}_e}{k}\sin^2(\sqrt{k}g\tau) \tag{2.62}$$

$$\mathcal{G}_k = \frac{\mathcal{R}_g}{k}\sin^2(\sqrt{k}g\tau) \tag{2.63}$$

and $\mathcal{R}_i$ is the rate at which the atoms are injected into the state $|i\rangle (= |e\rangle$ or $|g\rangle)$ per cavity decay time.

Equation (2.59) is the central result of the micromaser theory, describing the steady-state of the maser field and the starting point of the studies of the statistical properties of the field. In the case of a pumping where all atoms enter the cavity in the excited state $|e\rangle$, as showed in figure (2.4), field states with sub-Poissonian (super-Poissonian) statistics, also called "nonclassical" states, can be observed [35]. Particular states, such as bistable states or trapping states, were experimentally observed [15, 16, 29].

# Chapter 3

# Experimental Setup

*In this chapter, the experimental setup of the micromaser is developed. The generation of a controlled atomic beam and the high Q superconuctive cavity are introduced. The most relevant properties of the $^{85}Rb$ Rydberg atoms are studied. In particular the coupling constant is reevaluated and the Rydberg lifetime of the maser ground state, $61D_{5/2}$ is recalculated using the latest theoretical contribution. Improvements of the cryogenic system, leading to a continually controlable cooling temperature from 1.3 K down to 150 mK, are explained.*

The experimental realization of the theoretical Jaynes-Cummings model where a single two-level atom couples to a single mode of the field of a cavity is achieved with the micromaser experiment. The experimental idea of the micromaser is based on the MASER realized by Townes and co-workers [36], where an ammoniac molecular beam interacts with a low Q microwave cavity. In order to achieve the strong coupling regime where the dynamics is dominated by the coherent interaction between a two-level system and a single mode of radiation, highly excited Rydberg atoms and a high Q superconducting niobium cavity are used.

Cavities offering the longest lifetime are obtained in the microwave domain at frequencies of several tens of gigahertz (GHz) for wavelength $\lambda$ of the order of the centimeter. Since the microwave photon energy is smaller than the energy gap of certain superconductive materials, the photon absorption at the surface is reduced. The resistivity of a superconductor vanishing at absolute zero [37]. Long storage time of the microwave field on the order of few hundred millisecond in the cavity can be achieved. The superconducting $Nb$ cavity used in the micromaser experiment has a cylindrical form and has two small coupling holes along the atomic beam axis. The cavity is also designed to fulfill the experiments requirements:

- Only one mode of the cavity is resonant with the atomic transition .

- The decay rate of the cavity field for this mode has to be small enough to achieve the strong coupling condition: $\gamma << g$ (see Chapter 2).

The microwave transitions traditionally used in atomic physics (Zeeman transitions or hyperfine transitions) are not adapted to the realization of the strong coupling regime due to their very small coupling to an electromagnetic field. Hence, highly excited atoms, Rydberg atoms, are used. Rydberg atoms present many advantages:

- Rydberg-Rydberg atomic transitions, which are in the microwave region, present a large dipole moment as the wave functions of two neighboring states strongly overlap.

- Long lifetime with respect to the ground state as the wave function is strongly delocalized from the nucleus.

- Easily produced by laser field excitation.

- State-selective detection in DC-electric fields.

Figure 3.1 shows an overview of the experimental setup. The experiment is in a vacuum environment. This is done by means of turbo-molecular pump and a vacuum of the order of $5.10^{-7}$ mbar is achieved. For the realization of the micromaser experiment:

- A very dilute and stable $Rb$ atomic beam is produced from an oven.

- $^{85}Rb$ atoms are prepared in the maser state $|g\rangle = 61D_{5/2}$ atomic state and $|e\rangle = 63P_{3/2}$ atomic state by the mean of different laser excitation.

- A cryogenic environment is needed to work with a low thermal photon number and operate the superconducting $Nb$ cavity as high Q cavity in order to achieve the strong coupling regime.

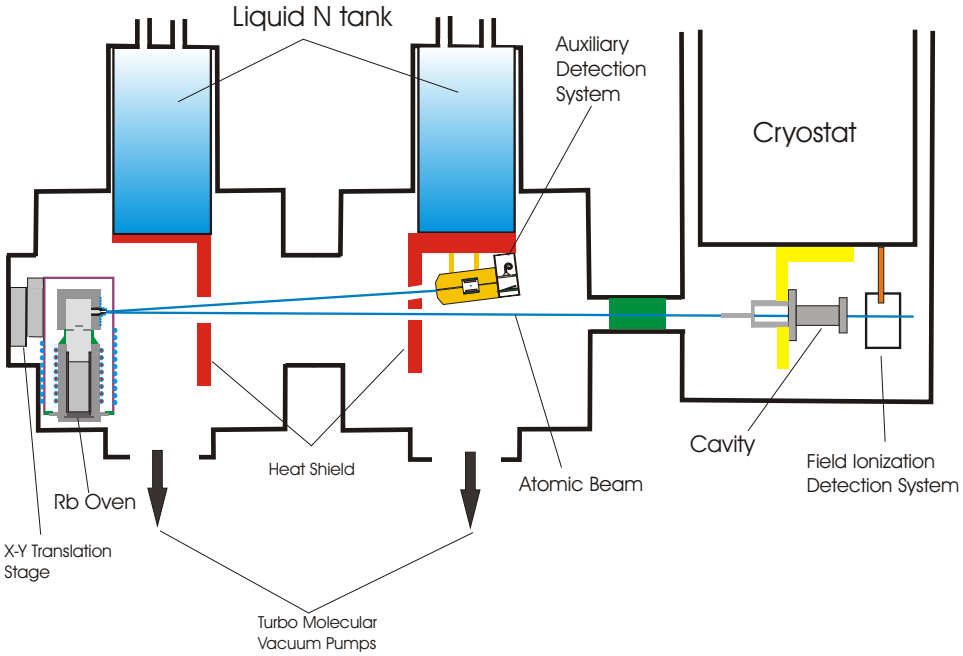


Figure 3.1: *Experimental Setup*

The *Rb* atomic beam is produced by an atomic oven. The beam is highly collimated by a collimator placed in front of the cavity. Moreover, due to its small aperture, 0.3 mm, it plays a role of thermal shielding for the cavity. Before entering in the cavity, the *Rb* atoms are prepared in the maser states by the help of laser radiation. A small fraction of the atomic beam is used in the auxiliary chamber for the laser frequency stabilization.

The $TE_{121}$ mode is the single cavity mode resonant with the Rydberg microwave transition $63P_{3/2} \iff 61D_{5/2}$. In order to achieve a very high Q-factor, the apertures of the cavity are reduced to the minimum. Therefore, it is impossible to perform a direct measurement of the cavity field, like for a classical MASER. Especially as the experiment concerns very small fields on the order of few quanta. Hence an indirect measurement of the cavity field via measuring the state of the atom after the interaction with the cavity field is used. This is done with the help of a state-selective field ionization detection based on the design described in [38, 39]. Through this detection, the information about the field statistics can be extracted [35]. However only a partial tomography of the quantum state of the field is performed as the atomic statistics only gives an information about the diagonal elements of the field's density matrix. A homodyne measurement can be done by mixing the

quantum field of the one atom maser with an external coherent field and map the phase information into the atomic statistics [40].

In the following sections, the description of the atomic beam production will be explained. An introduction to Rydberg atoms and their more relevant properties for the micromaser experiments will be discussed. Finally in the two last sections, the high Q-factor cavity will be described and the cryogenic system will be explained.

## 3.1 Atomic Beam

A scheme of the atomic oven is shown in figure 3.2. It consists of two stainless steel cylinders separated by an insulating material providing a thermal isolation between the two parts. The lower cylinder consists of a cartridge of rubidium and is mounted from below. The cartridge can be individually heated up with a resistance wire well above the *Rb* melting point at around 470K creating a *Rb* buffer gas in the upper part. The independent control over the heating temperature $T_1$ in the section 1 allows to determine how much *Rb* is evaporated, controlling the gas pressure in the oven and finally allows an independent adjustment of the atomic density flux.

The second section consists of a chamber where the *Rb* buffer gas is trapped before exiting through a nozzle, forming the atomic beam. Therefore the nozzle design plays a major role in the determination of the atomic beam properties. A longer nozzle with a small aperture will contribute to a better collimated atomic beam with a small spacial divergence at the expense of the atomic flux. Because of the long path from the oven to the cryostat, a nozzle with a rather small diameter, 0.3 mm, and 3 mm is used in the experiment, providing a good compromise between atomic flux and divergence, avoiding contamination of the vacuum with diverging *Rb* atoms. The section 2, and the nozzle in particular, is heated independently from the cartridge with a second resistance wire, allowing a separate control over the velocity distribution of the atoms forming the atomic beam. The velocity distribution of the atomic beam is described by a modified Maxwell-Bolzmann distribution law [41, 42]:

$$P(v) \propto P_{MB}(v)dv = \frac{1}{2}\left(\frac{m}{kT}\right)^2 v^3 e^{-\frac{mv^2}{2kT}} dv \tag{3.1}$$

In the case of the micromaser experiment, the coupling constant g and the cavity length $l$ define the velocity range (at least 150 to 850 m/s) needed to cover a full Rabi cycle ($g * l/v \in [0, 2\pi]$). The $^{85}Rb$ atomic velocity distribution dependence is shown in figure 3.3. Such a setup then provides a full control over the atomic flux and the atomic velocity independently as the temperature

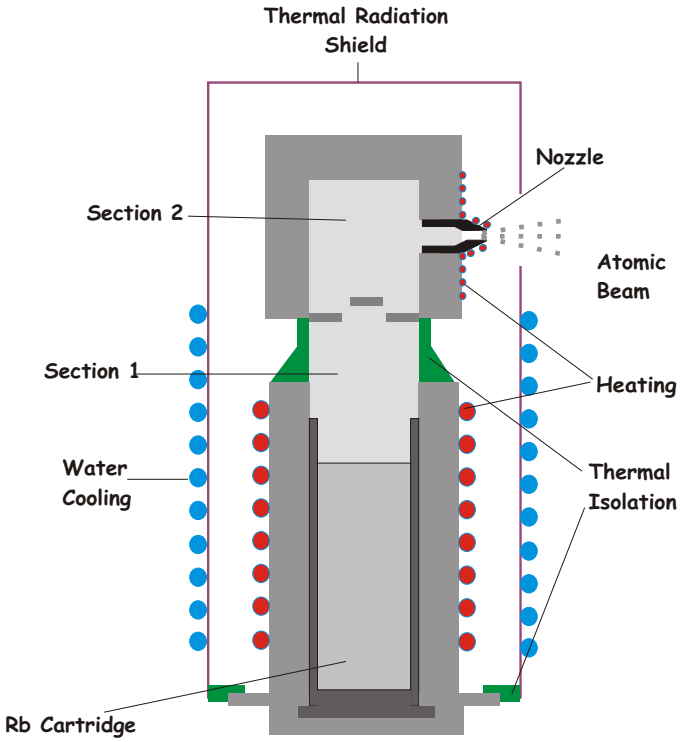


Figure 3.2: *Atomic oven design providing a high stable Rb atomic beam*

$T_1$ of the cartridge determines the atomic density and the temperature $T_2$ of the nozzle determines the velocity distribution.

The whole oven is surrounded by a water cooled copper shield, reducing the thermal radiation and achieving a pre-collimation. A cooper shield cooled down to liquid nitrogen is placed in front of the oven trapping the atoms far-off the atomic beam axis and keeping a low vacuum by cryogenic pumping. In the second chamber, the so-called "auxiliary chamber" a small fraction of atoms is used for spectroscopical purpose and frequency locking of the laser system. The second cooper shield cooled down to 77 K is placed in the atomic beam path, reducing furthermore the thermal radiation emitted from the oven, pointing directly into the cavity.

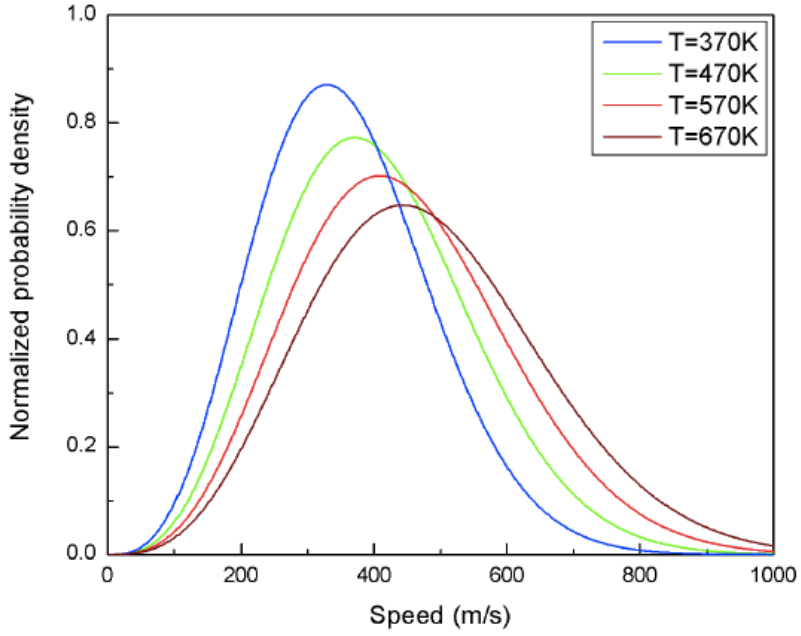


Figure 3.3: *Velocity distribution for $^{85}Rb$ atoms for different temperatures*

The main experiment setup where the cavity is mounted and the final collimation is achieved, is about 0.9 m away. The oven is mounted on a X-Y translation plate for an easier fine tuning alignment with the cavity axis and the atomic beam collimator placed in front of it.

The main collimation of the atomic beam is achieved in the cryostat. A good collimation is important for two reasons. First, in order that all atoms couple with the same strength with the cavity mode, a high spatial resolution of the atomic beam path inside the cavity is required. Second, the atomic velocity selection, determining the interaction time, is achieved by means of Doppler selection, where the atoms interact with the laser radiation at a well defined angle (see Chapter 4). Smaller angular dispersion will, therefore, lead to a narrow velocity distribution. The dimension of the collimator placed just in front of the cavity has the following dimension, 50 mm length and 0.3 mm diameter offering a good compromise between the atomic flux and the angular dispersion, giving an angular acceptance of 0.34 deg.

The collimator also plays the role of a thermal shield as it is mounted on the same cold finger as the cavity and cooled down to several hundreds of mK. The atomic beam collimator and the laser excitation region are both made of Nb providing a uniform environment for the Rydberg atoms, avoiding

contact potential with the resonator, with a stable zero magnetic field and at a constant temperature.

## 3.2 Rydberg Atoms

Rydberg atoms are excited atomic systems where an electron has been promoted to a level with large principal quantum number $n$. Their radiative properties are very interesting for several reasons: first, the large electric dipole matrix elements between neighboring levels - proportional to $n^2$- are typically three orders of magnitude larger than for atomic system in the ground state or lower excited state. Then, the coupling to a radiation field is very strong. Second, these atoms have very long spontaneous emission lifetimes, which means that one can manipulate them for a long time without loss of the atomic coherences.

The first experiment on Rydberg atoms was done by the end of the $19^{th}$ century as Balmer measured in 1885 the hydrogen line and derived the Balmer-formula. In 1890 Rydberg started to classify, by series, the spectral ray of Alkali-atom in the form of $S$=sharp, $P$=principal, $D$=diffuse[43] leading to the relation in energy:

$$\nu_l = \nu_{\infty l} - \frac{R_{Ryd}}{(n-\delta_l)^2} \quad for\ l = S, P, D \tag{3.2}$$

where $\nu_{\infty l}$ is the limit of the series, $R_{Ryd} = 109721.6\ \mathrm{cm}^{-1}$ the Rydberg constant and $\delta_l$ the quantum defect. From these relations one can derive the energy difference between two energy states and then define the transition frequency between these two states. The meaning of $n$ became then clear with the introduction of Bohr's Hydrogen Model, as the principal quantum number describing the orbit of the electron around the nucleus. The electron biding energy $W$ to the nucleus can be then written for the hydrogen atom as:

$$W = -\frac{e^4 m_e}{32\pi^2\epsilon_0\hbar}\frac{1}{n^2} = -\frac{R_{Ryd}}{n^2} \tag{3.3}$$

As the atom size also grows with $n^2$, the large size of the Rydberg atoms combined with the small transition probabilities lead to a very long lifetime of the Rydberg states. Lifetimes up to 50 ms were measured [44]. There are many different ways to produce Rydberg atoms. The most probable is the recombination of ions. This occurs when ions collide with neutral particles and exchange charges or by recombination of ions with electrons [45]. The recombination process plays a major role in plasma physics. The disadvantage of these methods are that the final Rydberg states can not be determined.

Rydberg atoms can also be produced by means of laser radiation, which is the technique used for this work. The use of a narrow laser transition allow to populate only the target Rydberg states. Moreover coherent population can be achieved [46].

In this work $^{85}Rb$ atoms are used. They are alkali atoms and hydrogen-like as only one electron is sitting in the outer shell. The difference between hydrogen and hydrogen-like atoms is that the electron does not see only a proton but a nucleus with an electron cloud forming a positive charge entity. In this system, the energy levels of the outer electron are shifted compare to the hydrogen atom. The energy shift can be calculated as we exchange the main quantum number $n$ by the effective quantum number $n^*$ :

$$n^* = n - \delta_{n,j,l} \tag{3.4}$$

where $\delta_{n,j,l}$ is called the quantum defect [47]. The quantum defect can be calculated by the Rydberg-Ritz formula:

$$\delta_{n,j,l} = \delta_0 + \frac{\delta_2}{(n-\delta_0)^2} + \frac{\delta_4}{(n-\delta_0)^4} + \frac{\delta_6}{(n-\delta_0)^6} + \frac{\delta_8}{(n-\delta_0)^8}.... \tag{3.5}$$

The $\delta_i$ coefficient are experimentally determined and were lately improved for $Rb$ atoms with absolute frequency measurements in an atomic beam [48]. The energy level of the Rydberg states can then be recalculated:

$$W = -\frac{R'_{Ryd}}{(n^*)^2} = -\frac{R'_{Ryd}}{(n-\delta_{n,j,l})^2} \tag{3.6}$$

with $R'_{Ryd}$ is the particular element Rydberg constant. In the case of $^{85}Rb$, it values $109736.605\,cm^{-1}$ [49].

In the following sub-section, the main properties of the Rydberg states used for the micromaser will be briefly described.

### Microwave Transitions between Rydberg Levels

The transition frequency between two neighboring Rydberg states scales with the main quantum number $n^{-3}$:

$$\omega_{nl\to n'l'} \sim \frac{2R_{Ryd}}{n^3} \tag{3.7}$$

For Rydberg transitions with $n \approx 50 \ldots 65$, the transitions are in the microwave regime of the order of tens of GHz. In the micromaser, the Rydberg transition $63P_{3/2} \iff 61D_{5/2}$ in $^{85}Rb$ at 21.456 GHz is used.

The matrix element $\mu$ for the dipole interaction between two Rydberg states scales proportional to $n^2$:

$$\mu = \langle nl|er|n'l'\rangle \sim e\, a_o\, n^2 \tag{3.8}$$

Typical values for $\mu$ with $n = 60$ are three orders of magnitude larger than for optical transitions and are much larger than microwave hyperfine or Zeeman transitions used traditionally in atomic physics. The exact value of the dipole matrix element can be determined with the help of a model presented in [50, 51, 52, 53]. For the maser Rydberg transition $63P_{3/2} \iff 61D_{5/2}$:

$$\frac{\mu}{ea_0} \sim 1355 \tag{3.9}$$

The vacuum Rabi frequency $\Omega$ for the coupling of the two Rydberg level atom system with the single mode of a cavity can then be calculated using the relation:

$$\hbar\Omega = \mu E_0 \tag{3.10}$$

with $E_0$ given by (2.25). In the case of the micromaser experiment, the vacuum Rabi frequency is $\sim 7.2$ kHz.

### Rydberg Atoms Lifetime

One of the most important properties of the Rydberg atoms for their application in the maser are their long lifetime. Namely, in order to realize a coherent interaction, the Rydberg atomic states have to survive during the whole experiment. This implies, that there is no decay into the atomic ground state during the interaction with the cavity mode. Also, as no direct measurement of the field can be achieved, the measurement of the atomic state provides an indirect measurement of the cavity field. Therefore, a decay of the atomic state would lead to a loss of information. The time of flight of the Rydberg atoms from their production till their detection, is typically on the order of few 100 $\mu$s.

The lifetime of highly excited states can be very large. If only one decay channel to a lower state exists, the lifetime $\tau$ of the excited state is then given by the inverse of the Einstein $A_{n',l',n,l}$ coefficient. In the case of Rydberg states, more than one decay channel is available, and $\tau$ can be then calculated by summing over all possibilities:

$$\frac{1}{\tau} = \sum_{n,l} A_{n',l',n.l} \tag{3.11}$$

The lifetimes for Rubidium atoms $S$, $P$, and $D$ states have been calculated up to $n = 80$ [54] and experimentally determined until $n = 45$ [55]. A semi-empirical formula is commonly used for the approximation of numerical results on radiative lifetime $\tau$ [56]:

$$\tau = \tau'(n^*)^\gamma \tag{3.12}$$

with $n^*$ the effective quantum number and $\tau'$, $\gamma$ are state dependent coefficients.

| State | $\tau'_{th}(ns)$ | $\gamma_{th}$ | $\tau'_{exp}(ns)$ | $\gamma_{exp}$ |
|---|---|---|---|---|
| $S_{1/2}$ | 1.43 | 2.94 | $1.45 \pm 0.03$ | $3.02 \pm 0.02$ |
| $P_{1/2}$ | 2.4360 | 2.9989 | $2.80 \pm 0.03$ | $3.01 \pm 0.03$ |
| $P_{3/2}$ | 2.5341 | 3.0019 | | |
| $D_{3/2}$ | 1.0761 | 2.9898 | $2.10 \pm 0.03$ | $2.89 \pm 0.02$ |
| $D_{5/2}$ | 1.0687 | 2.9897 | | |

Table 3.1: *Lifetime parameters for Rb Rydberg atoms calculated from [54] and experimentally determined in [55]*

However this formula is valid only for a temperature $T = 0$ as the blackbody radiation (BBR) also has an impact on the Rydberg states lifetime, inducing other transitions in new decay channels. For a given $n$, spontaneous transitions occur predominantly to low excited states, while BBR populates mostly neighboring levels with $n' = n \pm 1$. Hence, a correction to the actual lifetime has to be done [49]:

$$\frac{1}{\tau} = \frac{1}{\tau_0} + \frac{1}{\tau_{BB}} \tag{3.13}$$

with,

$$\frac{1}{\tau_{BB}} = \frac{4\alpha^3 k_B T}{3\hbar(n^*)^2} \tag{3.14}$$

where $\alpha$ is the fine structure constant. In the case of the micromaser experiment, the Rydberg atoms evoluate in a cryogenic environment at a temperature T $\sim$ 300 mK, so the black body corrections are negligible and the lifetime of the exited and ground maser states are 557 $\mu$s for the $63P_{3/2}$ state and 219 $\mu$s for the $61D_{5/2}$ state, respectively .

### Rydberg Atoms Production by Laser Excitation

The micromaser experiment studies the interaction between a well-defined two-level Rydberg atomic system and a single mode of a high Q microwave

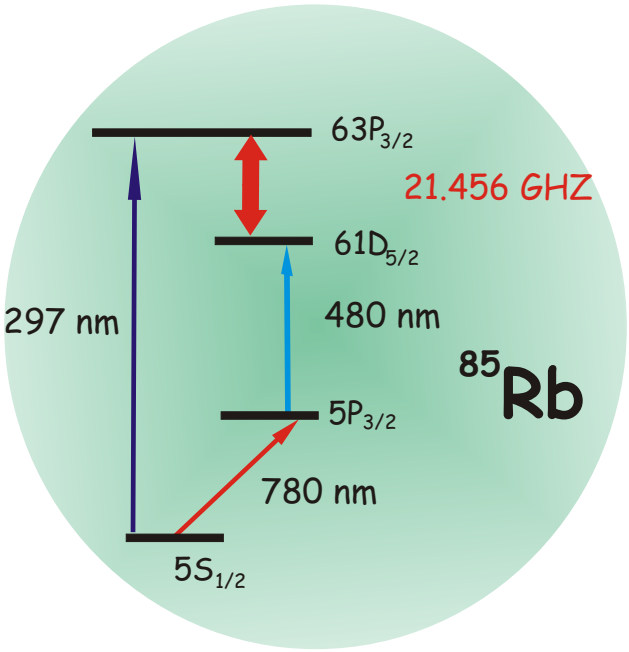


Figure 3.4: $^{85}Rb$ *Atomic scheme. The upper and lower maser states are the* $63P_{3/2}$ *and* $61D_{5/2}$ *states*

cavity. Figure 3.4 shows a scheme of the atomic states used in the micromaser experiment.

The state selective Rydberg excitations are performed by means of laser radiation. This is done either in a one step excitation scheme to promote the $^{85}Rb$ atoms from the ground state $5S_{1/2}$ into the upper maser state $63P_{3/2}$ or in a two step excitation scheme into the lower maser state $61D_{5/2}$.

For the one step excitation to the upper maser state, an Argon-Ion ($Ar^{+}$) laser pumps a Rhodamine $6G$ dye laser at 594 nm. The dye laser is then frequency doubled by a $BBO$ crystal in a ring cavity to produced the necessary UV light at 297 nm with an output power of about 40 mW. The use of dye laser shows however some disadvantages:

- Low laser excitation rate with a one-step Rydberg excitation scheme.
- Laser beam pointing instability leads to intensity fluctuation in the frequency doubling cavity, leading to instability of the excitation rate and an unstable micromaser operation.
- The instability in the laser output power implies an external intensity stabilization by an EOM. The maximum laser power after the EOM has

to be on the order of one half of the output UV power in order to have a constant laser power over many hours.

These disadvantages lead to the development of a new excitation scheme performing a three-step excitation with diode lasers in the infrared region [30]. The application of this three-step excitation scheme for the spectroscopy of Rydberg atoms in a room temperature gas cell will be discussed in more detail in Chapter 5.

In order to promote ground state $^{85}Rb$ atoms to the micromaser ground state, $61D_{5/2}$, a two-step excitation scheme is used due to the atomic selection rules: no direct transition from $S$ to $D$ states is possible. This is done by the mean of two external cavity grating-stabilized diode laser systems. The first stage excites the ground state $5S_{1/2}, F = 3$ to the $5P_{3/2}, F = 4$ state by a diode laser at 780 nm. The laser is stabilized on the atomic transition by a saturation absorption spectroscopy scheme in an external $Rb$ gas cell.

The second diode laser at 960 nm is frequency doubled by a $BBO$ crystal in an external ring cavity at 480 nm and can be then stabilized by two different means. The first one, which is also the traditional one, is done directly on the atomic beam. In the auxiliary chamber, a cryogenic-vacuum system, a small fraction of the atomic beam interacts with the two lasers and the number of Rydberg atoms is counted via a field ionization detection. The second step laser is then stabilized on the peak of the spectroscopic signal obtained on the atomic beam. The stabilization is done using an adapted synchronous demodulation (lock-in) technique. Error signals are processed by a computer which also calculates the PID feedback signal to the laser. One advantage of a digital treatment of the locking scheme is an easier change from one laser system to the other depending on which experiment one want to realize (use of the excited or ground atomic maser state).

The second method for the laser stabilization uses the Doppler-free spectroscopy signal of Rydberg atoms in a room temperature gas cell. The full description of this new method is presented in Chapter 5.

### Rydberg Atoms in an External Electrical Field

Due to the large separation between the nucleus and the out-bounding electron, Rydberg atoms are highly sensitive to the interaction with an external electrical field, e.g Stark Effect. The dependence representation of the electric fields of the atomic states and, therefore, their excitation frequency, is known as Stark map. Such Stark maps can be calculated and so the frequency offset due to the perturbation of the external electrical field can be determined [58]. Using the strong sensitivity of the Rydberg states to an external electrical field, one can tune the atomic frequency transition in a very controlled way,

applying an external electric field at the laser excitation place. Such a scheme is used to select the atoms velocity for the micromaser experiment and will be discussed in more details in Chapter 4.

Increasing the electrical field leads to the ionization of the atom. This field ionization will be used in order to perform a state selective detection of the Rydberg states in the micromaser experiment.

**State-Selective Detection in the One-Atom-Maser Experiment**

The measurement of the cavity field is done in an indirect way through the state selective measurement of the atoms emerging from the cavity with a field-ionization [59]. The electrons produced from the ionization are then detected in two separate channels with a single channel electron multiplier (channeltron). The details of the electron detection setup have already been described in earlier work [30, 38]

A channeltron operates on the same principle as a photon multiplier detector. The electron hits the curved glass vacuum tube, creating an electron avalanche and multiplying the incident charges along the tube, forming at the output end a pulse of $10^7$ - $10^8$ electrons for a duration of $\sim$ 10ns. For the best performance, the BURLE 7010M is mounted in the experimental setup. It is a single channel electron multiplier in the form of a planar spiral with a conic aperture of 10 mm diameter. The detection of a single electron is done via the voltage measurement between the input of the channeltron which is grounded and the output at a high positive charge (3 kV). At such voltages, the minimum gain is around $5.10^7$. The voltage pulse produced by the electron avalanche has particular characteristics concerning its amplitude and can therefore be electronically discriminated from the background noise by a digital data acquisition and analysis. In order to operate the channeltron in the pulse counting mode one has to determine the gain by scanning the input voltage. In figure 3.5, the typical curve shows four regimes:

- At low gain the applied potential is not large enough to multiply the cascade charges and no pulse are produced or the pulse amplitude is too small to be detected.

- As the voltage applied is increased, the pulse amplitude produced from the electrons cascades also increases. However not all events are recorded as the pulse amplitudes differs from one event to the other and not all are above threshold.

- Increasing the gain further leads to a plateau where all event are collected. Increasing the voltage further raises the gain but the count rate remains constant.

- However, if the gain is to high ion feedback occurs do to the ionization of the rest gas present on the glass walls causing additional noise. This is an undesirable operation as a significant part of the detected signal is not produced from the ionization products, but from the positive ions and secondary electrons produced within the channeltron itself without any correlations to the input.

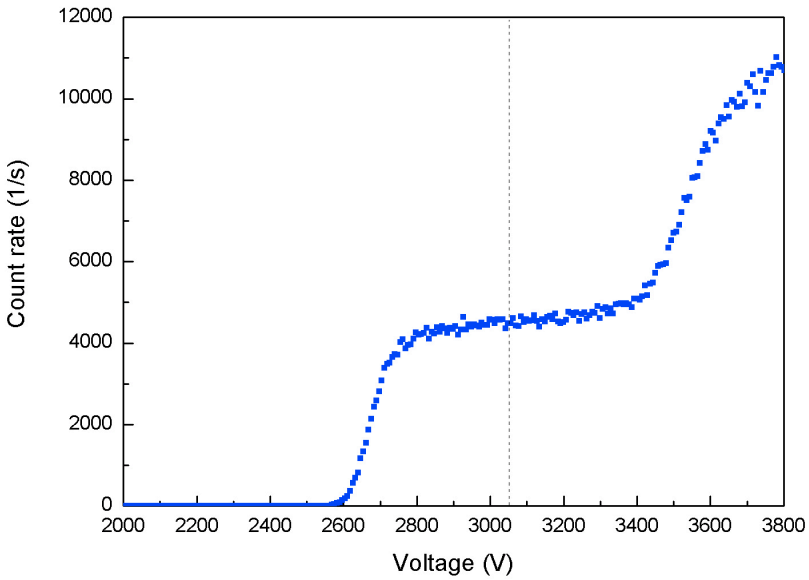


Figure 3.5: *Channeltron plateau measurement. Four regime are present. i) a low gain regime where the pulse amplitude generated by the electron cascade are not high enough to be detected. ii) an intermediate phase where a partial detection is achieved. iii) the plateau regime where all events are detected. iv) a saturated regime where undesirable electrons signals are present.*

For stability reasons, the middle point of the plateau is used as operating gain. If the input voltage changes during the maser operation, there are no consequences on the detection efficiency as the count rate remains the same even if the pulse amplitude slightly changes. From the measurement showed in figure 3.5, the operating voltage is set at 3050 kV, corresponding to the middle of this regime.

The channeltron temperature has to be considered with special care. At room temperature, the electrical resistance of the channeltron is around 600

MΩ. Due to the cooling at liquid $He$ temperature, the resistance increases by more than two orders of magnitude leading to a saturated operating regime. The electron cannot be replenished on the timescale of the pulse transit. Hence, the channeltron is heated at around 77 K by means of a special high resistivity $NiCr20AlSi$ wire (ISAOHM).

As previously mentioned, Rydberg atoms are highly sensitive to an external electrical field, e.g Stark effect. Increasing the electrical field to several tens of Volt per centimeter, one can reach the field strength where the outbound electron is no more bound to the nucleus, leading to the ionization of the atom. In the case of the Hydrogen atom, the Coulomb potential can be written as:

$$V = -\frac{e^2}{4\pi\epsilon_0 r} + eEr \tag{3.15}$$

In the absence of electron tunneling through the potential barrier, the saddle point of the potential can be calculated as $r_{max} = -\sqrt{\frac{e}{4\pi\epsilon_0}\frac{1}{E}}$ and the potential at this point reads:

$$V(r_{max}) = -2\sqrt{\frac{Ee^3}{4\pi\epsilon_0}} \tag{3.16}$$

As the binding energy is $W = -\frac{R_{Ryd}}{n^2}$, the ionization field reads:

$$E = \frac{R_{Ryd}^2 \pi\epsilon_0}{n^4 e^3} \tag{3.17}$$

In the case of hydrogen-like atom one just has to exchange $n$ with the effective quantum number $n^*$.

However, ionization processes can occur for a smaller field due to a tunnel effect of the outbound electron through the barrier potential. Also the case of pulsed ionization field is much more complicated, as different ionization channels have to be taken into consideration [49]. Therefore, for the micromaser experiment, the ionization of the Rydberg atoms is performed in a static and constant electrical field.

In the case of the two maser states, the strong dependence of the ionization field in $n$ is used to perform a state-selective ionization scheme applying two different field strength along the atomic beam path. The ionizing fields read respectively $E_{up} = 20.4$ V/cm for the upper maser state, $n = 63$ and $E_{down} = 23.2$ V/cm for the lower maser state, $n = 61$. The ionization process occurs in the so-called channeltron box which shields the experiment from the statistical electric field used for the ionization or produced by the channeltrons itself and the heating produced by the channeltrons due to their higher working temperature (77 K). Based on the plate condensator principle, the

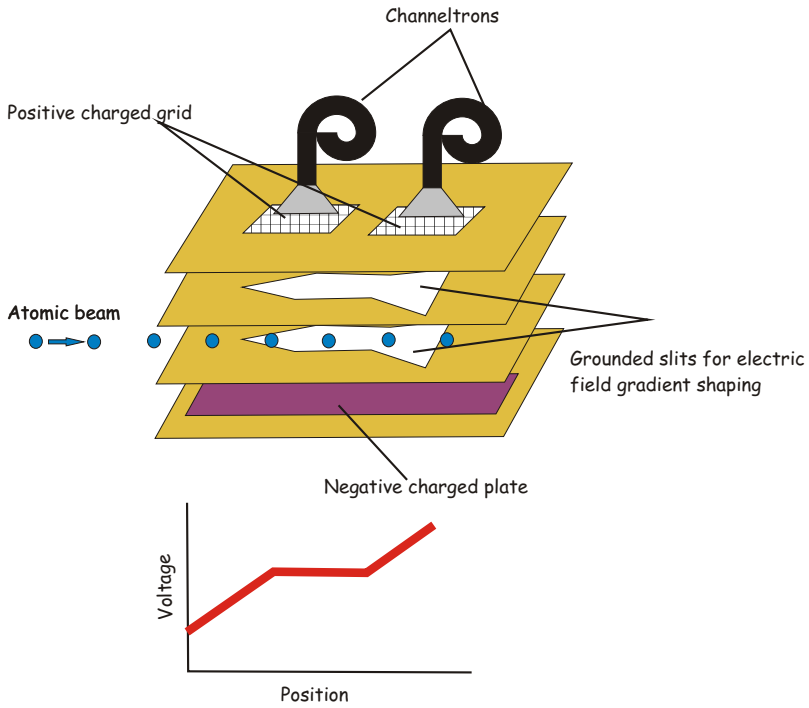


Figure 3.6: *Channeltron-box: state-selective field-ionization detection system. An increasing field is created along the atomic beam path between a negative charged plate and two positive charged grids. Atoms with different atomic states are then ionized and detected in two different detection channels.*

atoms are subjected to an adjustable electric field created between the negative charged electrode plate and the positive charged electrode grid. Using intermediate grounded plates, the electrical field is tuned along the atomic beam path due to the particular shape of these plates. In the region of the second channeltron, a stronger field is created than in the region of the first channeltron. In between, the electrical field remains constant to avoid the miscounts in corresponding channeltron, achieving a better spatial separation. The state-selective detection is achieved by collecting the ionizations products of the two different atomic states in two different channeltrons.

Figure 3.6 shows a picture of the channeltron-box. As the atoms in the upper maser state $63P_{3/2}$ are ionized by a smaller electrical field, they will be ionized in the first detection channel. The lower maser state $61D_{5/2}$ will be then ionized later along the atomic beam path at a higher electrical field intensity in the second detection channel. Choosing the right potential applied in the two ionizations areas, discrimination from one state to the other one is achieved and the state selective detection where each atomic state is detected

in a different channeltron is realized.

The calibration of the potential is done in the following way. First the cavity is tuned out of resonance, to have a beam of atoms prepared in the maser ground state $61D_{5/2}$. The electrode voltage is then scanned and the signal of both channeltrons is monitored and recorded with a computer. The measured signal is shown in figure 3.7.

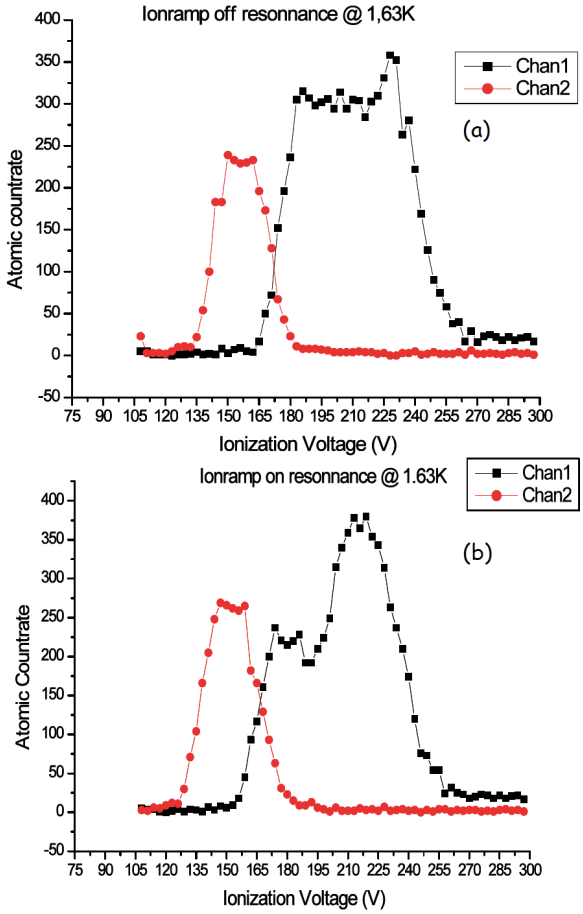


Figure 3.7: *Field-ionization signals for atoms in the upper-maser state and in the ground-maser state. In the case of non-resonant cavity (a) and the cavity tuned on resonance (b) are shown. The optimum ionized voltage lies at* $158V$

The same measurement is then done with the cavity tuned on resonance with the atomic maser transition, producing atoms in both the $61D_{5/2}$ and $63P_{3/2}$ state. The signal recorded from the second channeltron do not vary

corresponding to the maser ground state atoms ionized in the second detection channel until the electrical field is high enough in the first channel to ionize the maser ground state. However the signal collected from the first channeltron varies from the non-resonant case to the resonant one. When no excited states are produced (cavity off-resonance), the signal recorded in the first channeltron corresponds to all ground states atoms ionized. Also, the curves recorded from the two channeltrons do not overlap showing that practically no ground states atoms are detected in the first channeltron and the second one at the same voltage. When the cavity is on resonance, the curve of channeltron 1is shifted to a lower potential corresponding to the detection of atoms in the excited maser state, reflecting the lower ionization potential of the $63P_{3/2}$ state. The slope of the curve also changes showing a step profile. The first plateau corresponds to the detection of the excited states atoms while the second plateau corresponds to the detection of all atoms without any state selection.

The optimum value of the applied ionization voltage lies where in the first channeltron the maximum of excited maser state are detected and at the same time a minimal of maser ground state . Analogously for the second channeltron where the maximal of ground states atoms are detected with a minimum of excited states. The optimum values in this case lies at 158 V. This value is higher than the theoretical one presented earlier. However one has to take into consideration the particular design of the channeltron box, with the two ground plates forming the field gradient and the distance of 2 cm between the two charged electrodes.

For the laser stabilization a much simpler ionization set-up is used as no state selective detection is needed. Placed in an auxiliary chamber, a small part of the atomic beam interacts after collimation with the laser radiation and is excited into the maser ground state $61D_{5/2}$. The atoms are then ionized in an orthogonal static electrical field produced by a tilted negative-potential ionization plate, producing an increasing field along the atomic beam path. This allows to keep a narrow zone of the ionization region and put the atoms in a linear electrical field ramp, avoiding the abrupt turn on of the ionization field corresponding to a pulsed electrical field. The signal detected is then digitally processed to lock the second step laser onto the maximum of the spectroscopic signal.

In the excitation region, a small electrical field can also be produced with two parallel condensator plates. Shifting the atomic frequency due to the Stark effect. This precisely controlled laser frequency shifting is then used to perform a velocity selection of the atom and will be described in more details in Chapter 4.

## 3.3 Cavity

For the generation and storage of the quantum light field, a superconductive cavity, developed and manufactured at the Max Planck for Quantum Optics, is used [60].

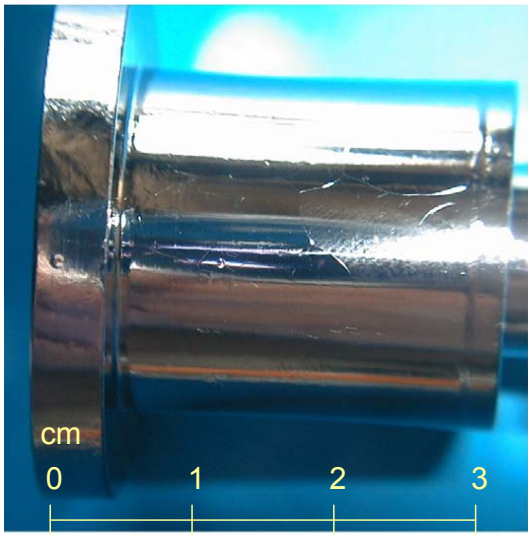


Figure 3.8: *The high Q-factor superconductive niobium cavity used in the micromaser experiment*

The microwave cavity has a cylindrical form with a length and a diameter of about 25 mm. At the centers the presence of two holes with a 2 mm aperture allows the atomic beam to enter and exit the cavity as also the injection of an external microwave field.

Along the atomic beam axis, only the $TE_{1np}$ modes have a non vanishing transversal electric field. In the case of the micromaser experiment, the Rydberg atoms interact with the $TE_{121}$ mode. The mode form corresponds to a half period of a sine wave. Also, the polarization direction allows an external coherent field injection via a simple microwave coupling through an external waveguide. This is important, first for the cavity frequency and the Q-factor measurements, and in the case of experiments requiring coherent states like the study of the phase diffusion process. The resonance frequency of a cylindrical cavity is given by [61]:

$$\omega = c\sqrt{\frac{x_{12}^{'2}}{R^2} + \frac{\pi^2}{L^2}} \tag{3.18}$$

where $R$ and $L$ are the radius and length of the cavity respectively and $x_{12}^{'}$ is the 2-nd zero of the first derivative of the Bessel function $J_1$.

Finally, with the mode volume of the $TE_{121}$ mode, $V = 1.58.10^{-2}\pi R^2 L$, the parameter $E_0$ of equations (2.25) and (2.28) can be calculated to $E_0 = 1.1\,10^{-3}$ V/m and so the atom-field coupling constant $g$ in the Jaynes-Cummings model can be evaluated (see equation 3.10 ). The distribution of the transverse E-field in the cavity is shown in Figure 3.9.

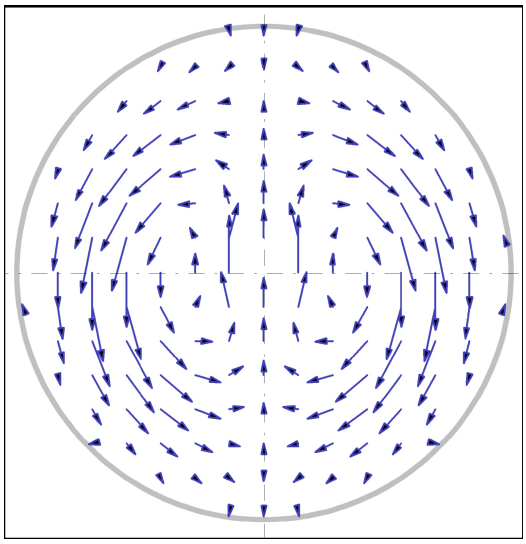

Figure 3.9: *The transverse electric field distribution of the $TE_{121}$ mode in the cavity*

In the case of a perfect cylindrical cavity, the $TE_{121}$ mode is doubly degenerate. The degeneracy is then lifted by a slight deformation from the circular cross-section into an oval shape, determining the direction of polarization of the field mode. The deformation is achieved as the cavity is mechanically squeezed, shifting the two polarization components, vertical and orthogonal, respectively to higher and lower frequency due to their dependence on the spacial dimension. In this experiment, the vertical polarization mode is used.

**High Quality Factor Superconductive Cavity**

In order to achieve a long coherence time in the micromaser field, e.g long

lifetime of the light field trapped inside the cavity, a high Q-factor is required. This is achieved taking advantage of the superconductivity property of the niobium, $Nb$. Hence, the cavity is made of 99.9 % pure $Nb$. At atmospheric pressure, the critical temperature for superconductivity of $Nb$ is 9.3 K [62] leading to the reduction of the field dissipation, enhancing the Q-factor. Since the unloaded electrical Q-factor of a vacuum superconducting cavity is given by [63]:

$$Q_0^{-1} = R_s \Gamma^{-1} \tag{3.19}$$

where $R_s$ is the surface resistance and $\Gamma^{-1}$ is the geometric factor of the mode, low $R_s$ leading to high Q-factor. The physical properties have been described in detail in [64].

Also, a recipe for minimizing the surface resistance to several $n\Omega$, combining electron polishing, chemical etching and backing procedure at around $1800°C$ for 24H in a ultra high vacuum oven is presented there [65] [66][67].

The backing procedure relieves an important step to achieve the high Q-factor, through the reduction of lattices irregularities and building 1-10 mm single crystal domains. Therefore, reducing the light-element concentration, homogenizing their distribution. At the same time, the thickness of the surface oxide layer is reduced.

Finally the cavity properties, frequency and Q-factor, are tested at very low temperature, reaching the superconductive temperature with the help of a He-bath cryostat.

**Frequency and Q-factor Measurement**

The resonance frequency of the $TE_{121}$ mode is 21.456 GHz. The tuning of the cavity frequency is achieved via the elastic mechanical deformation of the cavity cylinder. First, the resonance of the cavity is measured by the injection of a microwave field (with Wandel Goltermann tracking generator TG-23) into the cavity and analyzing the reflected signal, coming back through a circulator with a spectrum analyzer (Wandel Goltermann SNA-33). Figure 3.11 shows the basic setup of the frequency measurement. Adjustment of the cavity frequency is done in two steps. A first rough tuning in the range of 15 MHz is achieved by a mechanical screw driver. The cavity frequency is adjusted by this mean slightly below the resonance frequency (typically down to 300 kHz). The fine frequency adjustment is then done by the piezoelectric drive over a 1 MHz frequency range with 0.6 KHz steps (piezoelectric sensitivity: 600 Hz/V). Figure 3.10 shows the measured cavity frequency tuning range as a function of the applied piezo voltage. The relative large tuning range of the cavity allows the study of the complete tuning range of the micromaser in a single mode configuration.

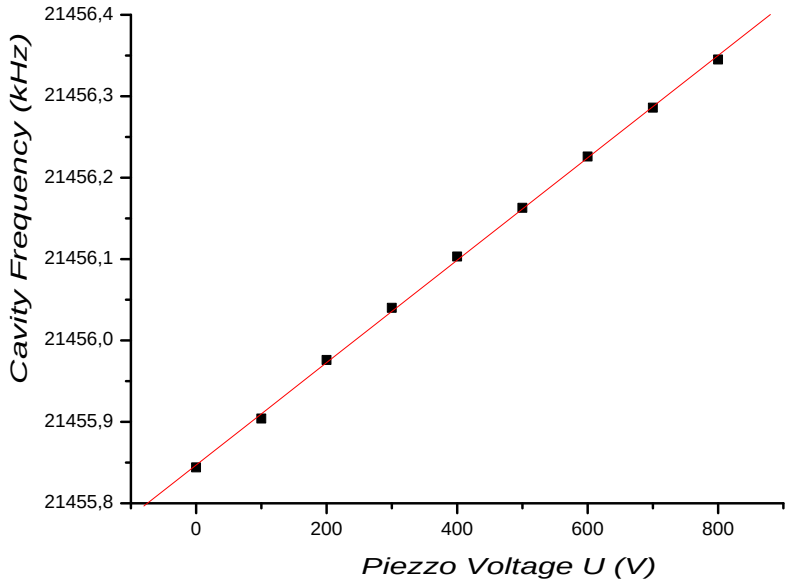


Figure 3.10: *Cavity frequency dependence as scanning the applied the piezo voltage. From the measurement the piezoelectric sensitivity is 600 Hz/V*

The measurement of the cavity Q-factor is done by the mean of a heterodyne scheme, since a direct measurement of the microwave field intensity inside the cavity is rather complicated. The setup of the heterodyne measurement is the same as the one used for the frequency measurement and is depicted in figure 3.11. The only difference lies in the microwave generation. In the case of the Q-factor measurement, two microwave signals generated from a synthesizer (Systron Donner 1730B) which is periodically modulated between two frequencies - one on resonance with the cavity, $\omega_0$ and the other one detuned by 100 Hz, $\omega_1$, are send to the cavity. Inside the cavity, the resonant field is stored and starts to decay exponentially at the frequency $\gamma$. After a certain time $t$, corresponding to the synthesizer periodicity, the off-resonant field reflected by the cavity superimposes with the coupled out resonant field, creating a beat note between the two fields propagating back through the rectangular waveguide and microwave circulator to the detection microwave diode. The electric field reads:

$$E(t) = E_0 e^{-i\omega_0 t+\phi_0} e^{-\gamma t} + E_1 e^{-i\omega_1 t+\phi_1} \tag{3.20}$$

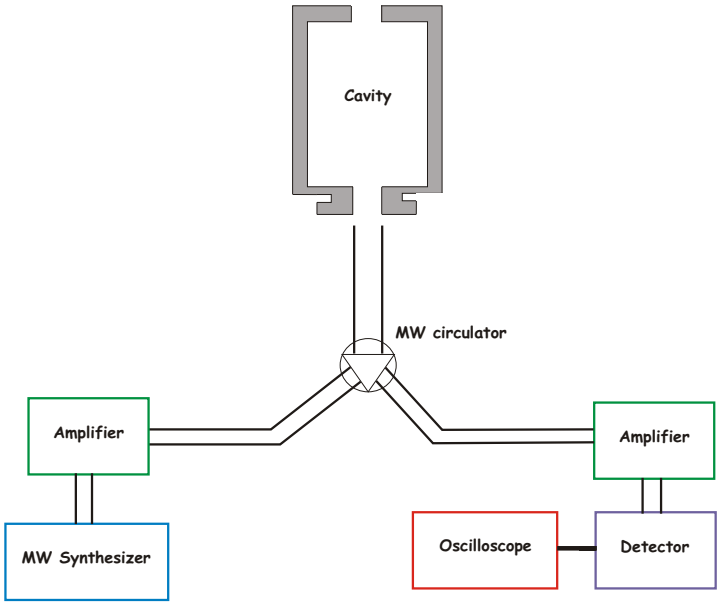


Figure 3.11: *Frequency and Q-factor measurement setup.*

Using a high pass filter, the strong reflected signal $|E_1|^2$ is filterd out and the detected beat note signal is then proportional to:

$$|E(t)|^2 \propto 2E_0E_1cos[(\omega_0 - \omega_1)t + \phi_0 - \phi_1]e^{-\gamma t} \tag{3.21}$$

This shows that the beat signal decays with the same time constant as the cavity decay time. Measuring the decay time of the beat signal amplitude gives a direct measurement of the cavity photon lifetime, the cavity Q-factor:

$$Q = \omega_0\tau_f = \frac{\omega_0}{\gamma} \tag{3.22}$$

where $\tau_f$ is the cavity decay time.

Figure 3.12 shows a typical result of such a heterodyne measurement. Corresponding to a decay time of 73 ms, extracted from the fit, the cavity Q-factor is $Q = 4.9\,10^9$.

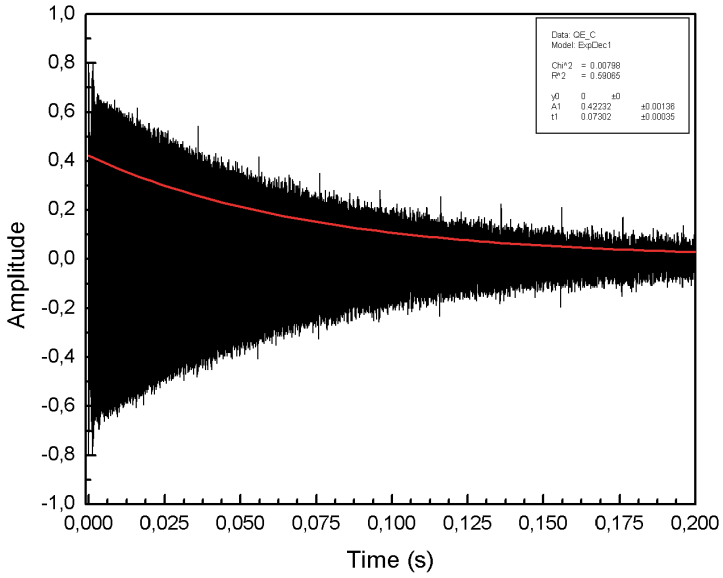


Figure 3.12: *Cavity Q-factor with a heterodyne measurement. Fram the fitted red curve, the extracted energy time is* 73 *ms coinciding to a Q-factor value of* $4.9\,10^9$.

## 3.4 Cryogenic Environment

The micromaser experiment has to be operated at very low temperature for three reasons:

- The micromaser experiment investigates the coupling between a single atom and a quantum state of light in cavity. In order to realize it, one has to operate it at a field with very few thermal photons. This means for microwave field to work at very low temperatures. Figure 3.13 shows the mean thermal photon number $n_{th}$ dependence on the temperature. Usually, for photon number state experiments such as trapping state or Fock state Rabi oscillations a temperature below 0.5 K is required.

- Rydberg atoms are at the same time actors and messenger as we need to detect them in order to reconstruct the field statistic from the atomic statistic. As have been seen in the previous section, the decay to the ground state also depends on the temperature and Rydberg atoms need to evolve in a cold environment to achieve a long coherence time.

- The micromaser operates in the so-called strong coupling regime, which means that the decay constant of the cavity $\gamma$ as to be smaller than the coupling constant $g$. The superconductor surface resistance of the cavity is inverse proportional to the temperature. Therefore in order to achieve a high Q factor one has to cool down the $Nb$ cavity to a temperature below 0.7 K.

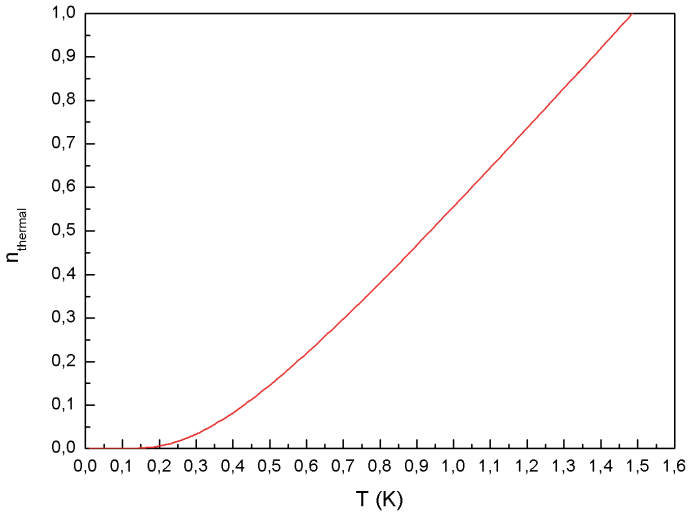


Figure 3.13: *Temperature dependence for the mean thermal photon number at* 21.456 *GHz.*

In order to reach such low temperatures a cryostat has to be used. Temperature such as 77 K or 4 K are easily reached by the use of a liquid nitrogen or liquid helium cryogenic system. These are bath cryostats and are the starting point of all cryogenic systems. Their conception is pretty simple. A liquid $He$ vessel placed in a vacuum environment is surrounded from a liquid $N$ vessel in order to reduce the heat leak due to the hot wall of the vacuum apparatus.

### $^3He$ Evaporation Cryostat

Evaporation cryostat are the simplest way to reach a temperature below 4 K. In order to reduce the temperature of liquid $^4He$, pumping the vapor above the bath allows to reach temperatures down to 1.3 K without much effort.

But it is not sufficient for our purpose. With a $^3He$ evaporation cryostat it is possible to reach lower temperature[68]. The use of $^3He$ has two essential advantages over $^4He$. First the higher vapor pressure allows temperatures as low as 0.3 K. Secondly, $^3He$ does not possess the problem created by creeping superfluid film, which lead to an enhancement of the heat transport from the warm part to the cold part.

A special designed Oxford $^3He$ is used and has been described in details in [30]. A nitrogen bath at 77 K and a $^4He$ bath at 4 K surround a vacuum chamber. In the center of this chamber is placen the $^3He$ pot (so called cold-finger) on which the main part of the experimental set-up, cavity with a microwave coupler, piezo system for cavity squeezing and the collimator, is mounted. To pre-cool the system a $^4He$ evaporation cryostat is used. The so-called 1K pot is connected to the main $^4He$ bath with the help of a narrow tube ( about 1 mm diameter). A needle valve controls precisely the liquid $^4He$ flow from the main bath. The $^4He$ is mechanically pumped to reach a temperature of 1.3K . The 1K pot then plays the role of a heat sink. At this temperature, the $^3He$ gas starts to condense in the $^3He$ pot. Once all the $^3He$ is condensed, reaching a temperature around 0.9 K one can start to pump it. The pumping is done via an absorption pump. In this case, the $^3He$ that is condensed inside the cold-finger is absorbed onto charcoal powder. While this operation, this absorption pump is cooled down below $40K$ by anchoring it at the $^4He$ main bath. Because of the large surface area of the charcoal pump, the $^3He$ is pumped in a very efficient way. The reduction pressure allows to reach a working temperature of 300 mK for a 12 hours cycling time. After the $^3He$ is pumped and the cold-finger is empty the absorption pump is warming up. Upon warming, the $^3He$ is desorbed. The $^3He$ gas is pumped back in the dumps for storage or can be re-condensed for a new cooling cycle.

### $^3He - ^4He$ Dilution Cryostat

In the previous section, we discussed the cooling process of a liquid by pumping the vapor above it. Using $^3He$, the lowest temperature that has been achieved is 0.24 K [69], where in our system the end working temperature is around 300 mK. In order to reach lower temperature, one has to use the specific thermodynamical properties of dilute $^3He - ^4He$ mixture. The basic idea of this method was first introduced by London in 1951 [70] .

The principle operation of a dilution refrigerator is based on the fact that a phase separation in $^3He - ^4He$ mixtures occurs at very low temperature. First, because $^4He$ atoms, due to their larger mass, have a lower zero-point energy, the $^3He$ atoms are more strongly bound to them than among each other. Secondly, the $^3He$ atoms obey to the Fermi statistics and thus their kinetic

energy increases with their number density, which leads to the reduction of the binding energy. Already at a $^3He$ concentration of 6.5% in $^4He$, the binding energy vanishes when $T \to 0$ and no $^3He$ can be dissolved in the $^4He$ and a phase separation occurs. A light, $^3He$ rich phase and a heavy $^4He$ phase are produced. In the dilution cryostat performed in Garching, a $^3He$ concentration of around 25% is used. This is energetically more favorable for the two phases.

The heart of the dilution refrigerator is the so-called mixing chamber where the transfer of $^3He$ from the light phase into the dilute one occurs. As the $^3He$ atoms in the $^3He$ rich phase have a lower entropy than the rest $^3He$ atoms in the heavy $^4He$ phase, the transfer of $^3He$ atoms from one phase to the other leads to a cooling of the mixture. In analogy to evaporation of gases, one can understand this process as an evaporation of $^3He$ atoms into the quasi-vacuum of the superfluid $^4He$. In order to use this cooling process in a continuous way a new phase separation occurs where $^3He$ atoms are extracted from the dilute phase and re-inject in the $^3He$ rich phase.

Figure 3.14 shows a scheme of the dilution cryostat used to perform the micromaser experiment. The $^3He-^4He$ circuit is sitting in a vacuum chamber immersed in a $^4He$ bath. As for the $^3He$ cryostat the $^3He-^4He$ mixture is condensed with the help of a so-called $1K$ pot. The cavity is directly mounted on the mixing chamber which is the coldest part of the dilution cryostat. The $^3He-^4He$ circuit consists essentially of the mixing chamber, the still and a counter flow heat exchanger. This circuit has to realize a sufficiently high circulation of $^3He$, while maintaining the heat load at the mixing chamber as low as possible. The circulation of the $^3He$ atoms is driven by pumping the still. The still is heated at around 0.7 K so that at this point a phase separation between the $^3He$ atoms and the $^4He$ atoms occurs. Due to their higher vapor pressure, most of the $^3He$ atoms are evaporated and pumped out. After cleaning in nitrogen and liquid helium traps, the $^3He$ atoms are re-injected in the cooling circuit and again pre-cooled in the 1 K pot. After the 1 K pot, as the pressure is sufficiently high, $^3He$ atoms condense before entering the counterflow heat exchanger system. this consists in two different types of heat exchangers. The first type, the so-called continuous heat exchanger is composed of two tubes that are mounted in a such complicated way so that the interface between the both is as large as possible to achieve a maximal thermal contact. The second one, so called step heat exchanger, consists of several chambers made from sintered silver in oder to increase the thermal contact area. There, the phase separation occurs with the lighter $^3He$ rich phase forming the top layer. In the mixing chamber, $^3He$ atoms are diffusing across the phase boundary and are mixed to the quasi-stationary liquid $^4He$, where adiabatic dilution causes the cooling. $^3He$ atoms then diffuse back to the still via the heat exchanger where they will be evaporated. The lowest temperature

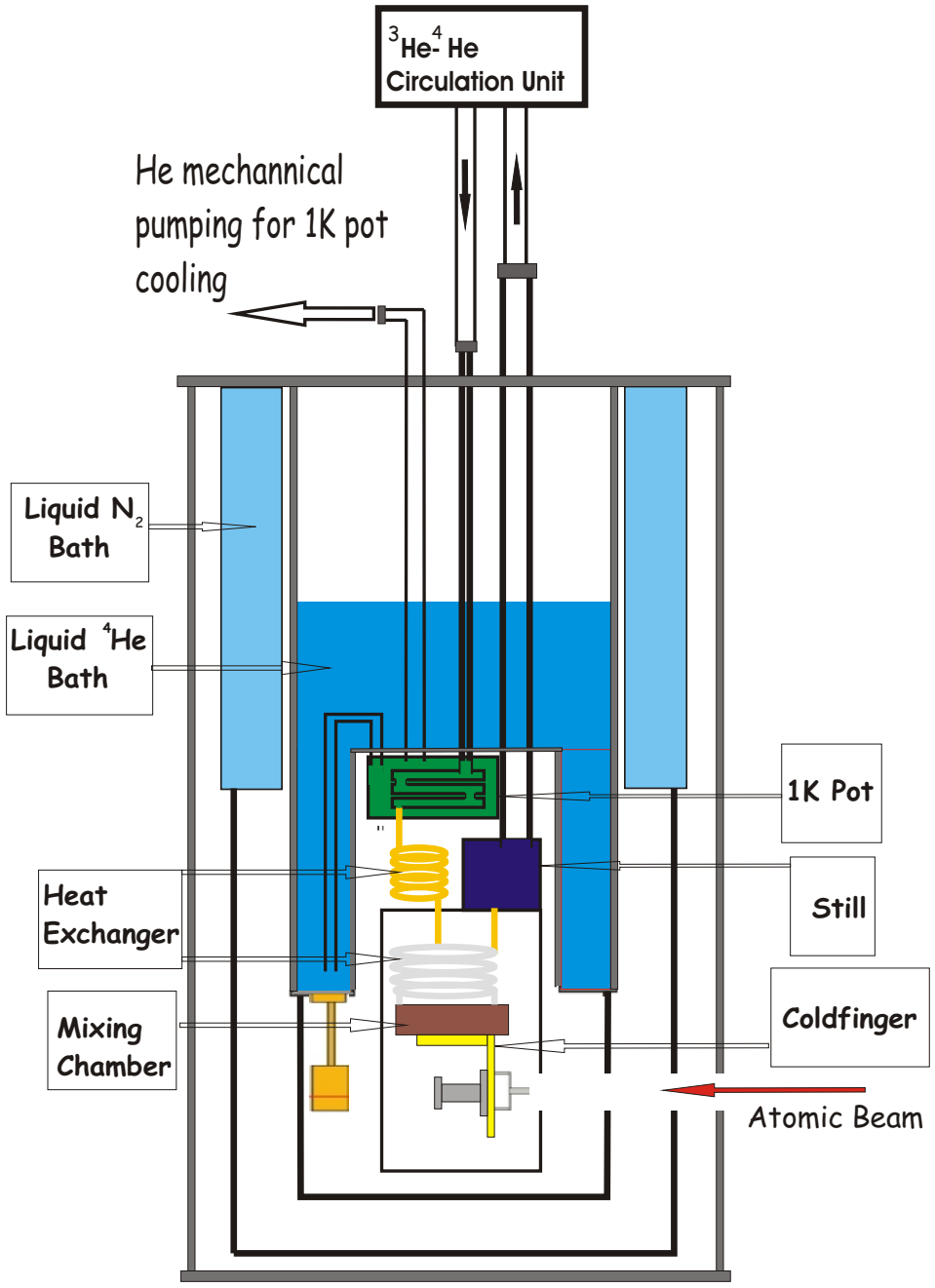


Figure 3.14: $^3He -^4 He$ *Dilution Cryostat*

obtained with a dilution cryostat is 1.5 mK [71]. In the micromaser experiment in Garching, the end working temperature is around 150 mK. This "bad" performance is due to the large mass that has to be cooled,e.g cavity, piezos system, and the outside heating due to the laser radiations, electrical wires, the close detection system at a 4 K temperature and the atomic oven. On the other hand a large improvement is done as the end working temperature was improved by adding a new shielding at 0.8 K and moreover, due to a better control over the still temperature a continuous working temperature range from 1.3K down to 150 mK is accessible which is one of the requirements for measuring quantum stochastic resonances in the micromaser [72].

# Chapter 4

# Experiments with Maser Ground State Atoms

*The first experiments with atoms in the maser ground state, the* $61D_{5/2}$ *Rydberg state are presented. The magnetic field compensation using the Hanle effect is realized for the first time in this configuration. Earth magnetic field avoids the degeneracy of the* $m_j$ *components of the Rydberg states and therefore, needs to be compensated at the mG level. The Stark effect of the Rydberg* $61D_{5/2}$ *state is investigated. The Stark effect is used in the micromaser experiment to perform a velocity section of the atoms, controlling their interaction time with the cavity field via the Doppler effect. Finally, the first maser experiments, where ground state atoms interact with the quantized thermal field of the cavity are performed. In particular, Rabi oscillations with a very high contrast are observed, performing a direct measurement of the field temperature.*

In Chapter two, the Jaynes-Cummings model describing the interaction between a two-level system and a single radiation mode of a cavity has been introduced. The realization of a very high-Q cavity with a long trapping time of the radiation field, and the large dipole interaction between two Rydberg states lead to the strong coupling regime where the coherent interaction is dominant. Cavity QED experiments with Rydberg atoms offer therefore a wide range of experimental conditions to study the light-matter interaction at the quantum level with a single atom.

The one-atom-maser or micromaser is a system where a stream of atoms interacts one by one with the cavity field. For a low atomic injection rate, with less than one atom per cavity decay time, the realization of Rabi oscillations between a nonclassical field and the two-level Rydberg system is possible. For a larger atomic pumping, the combination of the coherent interaction and decay processes leads to a steady-state of the field, analogous to a laser or a

maser. Due to the strong coupling, the presence of only one atom in the cavity is a sufficient condition to achieve stimulated emission. In the steady-state, the generation of a non classical field with sub-Poissonian statistics is possible. Finally, due to the long coherence time of the system, one atom can experience the field in the cavity created through the interaction between the cavity and the previous atoms opening a path towards atomic entanglement controlled by the coherent interaction with the cavity field [73].

In the following sections, the magnetic field compensation will be explained. This is necessary as the earth magnetic field affects the micromaser experiment on two aspects: the magnetic sub-levels are no more degenerated and an external field affects the the high Q factor of the cavity. Then, the velocity selection of the atoms and the control of the interaction time will be developed. Finally, the first experiments between ground states atoms and the quantized thermal field of the cavity are presented. The experiments are performed, both for large atomic pumping with the measurement of the so-called maser line and for low atomic injection rate where informations about the actual field temperature are extracted from the measurement of Rabi oscillations between ground states atoms and the cavity field at thermal equilibrium.

## 4.1 Magnetic Field Compensation

The earth magnetic field and the electronic components present in the experimental environment contribute to a non zero magnetic field in the experimental region of the order of 350 mG. This residual magnetic field has to be compensated due to its influence on the micromaser experiment. First, in the presence of an external magnetic field, the magnetic sublevels of the $63P_{1/2}$ and $61D_{5/2}$ are no longer degenerate. The different Lande-factors of the $m_j = +1/2 \leftrightarrow +1/2$ and $m_j = -1/2 \leftrightarrow -1/2$ transitions lead to a splitting of about 1.5 kHz/mG. Since the splitting should be smaller than the Rabi frequency $\Omega/2\pi \approx 7,2$ kHz, the magnetic field should be compensated at the mG level [74].

Another reason for the compensation lies in the cavity properties itself. Since the cavity is made from niobium, which is a superconductor of type II, below the superconductive critical temperature (9.3 K), the magnetic field fluxes freeze inside the material, increasing the high frequency resistance [75] of the cavity walls. The Q-factor is then degraded [76], leading to the reduction of the lifetime $\tau_{cav}$ of the field.

The all experimental setup is made of niobium which is a superconductor of type II and the compensation can be done only once before cooling down to liquid He temperature. Once the compensation is achieved and the cavity is cooled down below the superconductive temperature of 9.3 K, the zero mag-

netic field created around the experimental setup is frozen and kept as long as the cavity temperature is kept below the critical temperature.

The magnetic field compensation (MFC) is achieved by three pairs of Helmotz coils mounted perpendicular to each other outside the cryostat. The cavity is sitting in the center point. The current flowing through each pair of the coils is controlled by high precision current supplies (Burster Digistant 6426). In a first step, a rough magnetic field compensation down to $\sim 30$ mG is achieved using a magnetometer (Magnetoscop type 1.068). The final precise MFC is then performed using the atoms as magnetic sensor and observing the precession of magnetically oriented atomic sample in a variable magnetic field [77].

The principle of the traditional Hanle experiment is the following. In a first step, the atomic sample is magnetically polarized as the magnetic moments of all atoms are aligned along the same axis after the interaction with a first laser. Then as the sample is put in a presence of an external magnetic field, the magnetic moments of the atoms start to precess around non vanishing magnetic field (Hanle effect). Recording the polarization of the sample's fluorescence shows the precession frequency dependence on the magnetic field.

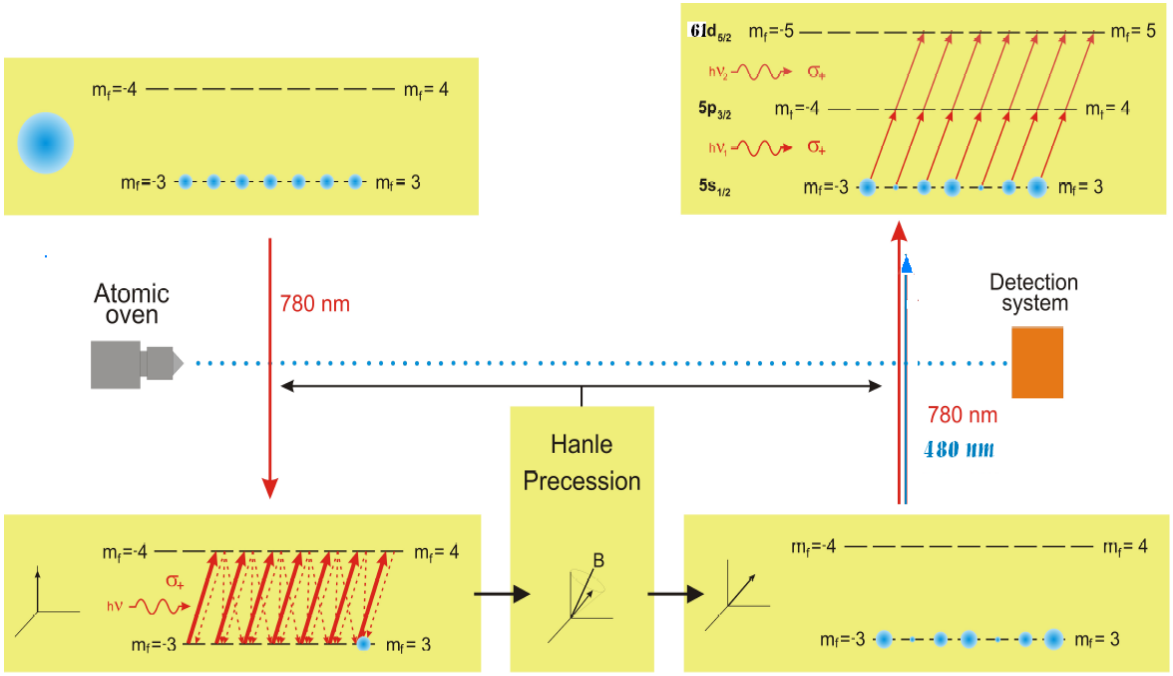


Figure 4.1: *Magnetic field compensation using the Hanle effect*

A detailed explanation of the experimental implementation of the Hanle

effect measurement in the micromaser is shown in figure 4.1. Atoms emerging from the oven are in equally distributed quantum states over all $m_f$ magnetic sub-levels. Using the hyperfine transition of the *Rb* D2 line at 780 nm:

$$5^2S_{1/2}, F = 3 \leftrightarrow 5^2P_{3/2}, F = 4 \tag{4.1}$$

and applying a circular polarized laser light it is possible to optically pump the atoms in a well-defined magnetic sub-level $m_f$. Since only the transitions of $\delta m_f = +1$ are allowed, after several hundred of absorption and spontaneous emission cycles the atoms are prepared in the quantum ground state $5^2S_{1/2}, F = 3, m_f = 3$ with well aligned magnetic moments.

Then, the atoms are placed in a static homogeneous magnetic field during a certain time $t$, corresponding to the time of flight of the atoms from the first laser excitation region where the optical pumping occurs to the second laser excitation region where the atoms are exited into a well defined Rydberg state.

The magnetic moment of the atom precesses around the magnetic field, thereby changing coherently the distribution of the $m_f$ quantum number states. The probability that the spin of the atom will be oriented in the initial direction ($m_f = +3$) after a time $t$ is given by:

$$P_{m_f=+3}(t) = 1 - \sin^2(\alpha)\, \sin^2(\omega t) \tag{4.2}$$

where $\alpha$ is the angle between the magnetic field and the laser beam, determining the quantization axis, and $\omega = g_F \frac{eB}{2m}$ is the Larmor frequency and $g_F$ the hyperfine structure Lande-factor (here 1/3). From equation 4.2, in the special case where the laser and the magnetic field are aligned, no precession occurs. The atoms magnetic moments and the magnetic field are collinear and the atoms remains in the $m_f = +3$ state. One can also note, if the interaction is fully coherent, one cannot speak strictly of magnetic coherent control over the magnetic level as only the $m_f = +3$ state is well defined over the interaction time as the distribution over the others $m_f$ states remains uncontrolled. The $m_F$ states can only be distributed corresponding to the orientation of the classical B field.

Finally, the atoms are excited to the $61D_{5/2}$ Rydberg state with a two-steps laser excitation scheme. The polarizations of the two lasers ($\sigma^+$, $\sigma^+$) are chosen so that in a zero magnetic field, the excitation rate over the ladder:

$$5S_{1/2}, F = 3, m_f = +3 \rightarrow 5P_{3/2}, F = 4, m_f = +4 \rightarrow 61D_{5/2}, F = 5, m_f = +5 \tag{4.3}$$

is the most efficient. The excitation probability depends on the $m_f$ quantum number as each transition has a characteristic Clebsch-Gordan coefficient depending on the oscillator strength. Therefore, in the case of a non-zero magnetic field, the excitation probability will then depend on the resulting $m_f$ distribution after the spin precession.

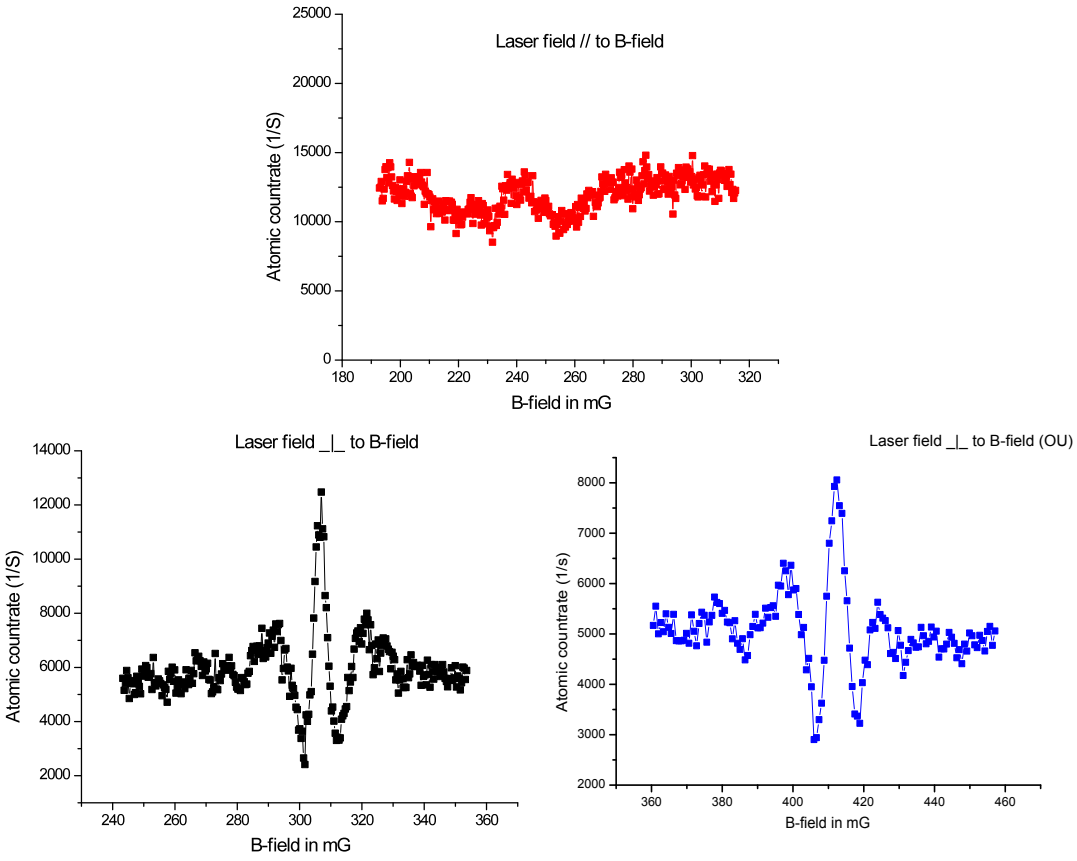


Figure 4.2: *Magnetic field compensation in the three directions*

Since the spin precession is periodic and the $m_f = +3$ time evolution is given by equation 4.2 , the excitation rate to the Rydberg level for an atom with a fixed interaction time, e.g fixed velocity, depends on the magnitude of the magnetic field, showing an oscillation of the atomic count rate as the magnitude of the magnetic field is scanned. And each maximum corresponds to a complete rotation. In the experimental realization of the MFC, no velocity selection is achieved and atoms with all velocity components contribute to the measurement. Then, only at $B = 0$, the oscillation shows a pronounced

maximum, since no rotation occurs and the magnetic moment remains aligned.

However, a symmetric oscillating pattern along one defined axis (x-axis for example) is only achieved if the other field component (y- and z-axis) are compensated to zero. An iterative method in all three direction is used to perform the MFC. Concerning the particular case, when the magnetic field and the laser are collinear, the zero-field point measurement is achieved by applying a small off-set field ($\sim 3$ mG) in one of the other directions.

Figure 4.2 shows the experimental result of the magnetic field compensation in the micromaser achieved with the detection of the $61D_{5/2}$ Rydberg state. The right compensating magnetic field is determined from the maximum at the symmetry center of the curve. And a magnetic field compensation with a precision on the order of 1 mG is achieved.

MFC measurements have been developed since the very beginning of the micromaser experiments. But the detection scheme using the micromaser ground state, e.g $61D_{5/2}$ Rydberg state shows improvements in the fringe contrast, due to the Clebsch-Gordan coefficients of the 2nd step laser with $\sigma^+$ polarization for the $5P_{3/2}, F = 4 \rightarrow 61D_{5/2}, F = 5$ transition, compared to previous measurements [78, 79].

## 4.2 Stark Effect and Velocity Selection by Doppler Effect

In chapter 2, the central equation determining the micromaser steady-state is derived and reads:

$$\rho_{nn}^{ss} = \rho_{00}^{ss} \prod_{k=1}^{n} \frac{n_{th}\gamma + \mathcal{E}_k}{(n_{th}+1)\gamma + \mathcal{G}_k} \tag{4.4}$$

with the Rabi dynamics contribution:

$$\mathcal{E}_k = \frac{\mathcal{R}_e}{k} \sin^2(\sqrt{k} g\tau) \tag{4.5}$$

$$\mathcal{G}_k = \frac{\mathcal{R}_g}{k} \sin^2(\sqrt{k} g\tau) \tag{4.6}$$

The mean thermal field photon number $n_{th}$ is determined by the cavity temperature, and the pumping rate is controlled by the laser excitation rate, e.g laser field intensity. The third experimental parameter, the interaction time is optically controlled via the Doppler effect and will be the subject of this section.

Accurate control of the interaction time between atoms and field plays an important role in the micromaser dynamics as it gives access to different quantum features of the produced field such as sub-poissonian field, trapping states

or bistability. In the case of the micromaser, since the cavity mode is oriented along the atomic beam axis, the interaction time is equal to the transit flight time of the atoms inside the cavity. The interaction time control has been achieved by different technics over the different experiments, presenting advantages and disadvantages. The first technique used was the mechanical velocity selection by means of nine Fizeau wheels. The main advantage is the very accurate selection with a interaction time spreading smaller than 4% [38]. On the other hand, the mechanical cut of the atomic beam strongly reduces the atomic flux.

**Doppler Velocity Selection**

The optical velocity selection of the atoms is achieved using Doppler effect via the angular excitation of the atoms. This allows the selection of a sub-velocity class among all velocities available in the thermal atomic beam. The Doppler selection is achieved using the angular excitation of the Rydberg atoms. The Rydberg excitation to the micromaser ground state, $61D_{5/2}$, is achieved by means of a two-step excitation scheme. The first laser step, promoting the $^{85}Rb$ atoms to the $5P_{3/2}, F = 4$ state is doppler free and interacts perpendicularly to the atomic beam. The Doppler selection is achieved as the second step laser at 480 nm interacts with the atomic beam at the same point as the first step but at an angle of 11°. Due to the angular excitation, the atoms see a Doppler shifted laser light, with the frequency:

$$\nu' = \nu_l \frac{c + v\sin\theta}{c} = \nu_l \left(1 + \frac{v\sin\theta}{c}\right) \tag{4.7}$$

where $\nu_l$ is the blue laser frequency, $v$ the atoms velocity and $\theta$ the angle between the atomic beam and the laser light field, as $c$ is the speed of light. It is therefore possible to select a certain velocity class of atoms by tuning the laser frequency as:

$$v = \frac{c\Delta\nu}{\nu_l \sin\theta} \tag{4.8}$$

where $\nu$ is the atomic transition, $5P_{3/2}, F = 4 \rightarrow 61D_{5/2}$, frequency and $\Delta\nu = \nu - \nu_l$. The accuracy of the velocity selection depends on several experimental parameters. The atomic divergence is reduced as the atomic beam is collimated (see Chapter 3). Other parameters are the laser frequency and laser linewidth. Compared to the one step excitation in the UV, the blue laser frequency is around 1.6 time smaller (297 nm compared to 480 nm) leading to an enhancement in the uncertainty of the same order. This increase in uncertainty is however counterbalanced by a better linewidth of the blue laser

system, leading to a typically interaction time spreading $\delta t/t$ of the order of 3%.

**Laser Frequency Shift using the Stark Effect**

In the previous chapter, the high sensitivity (or polarisability) of the Rydberg atoms due to an external electrical field E is explained and used for the state-selective detection scheme. At very small fields on the order of several hundreds of mV/cm, energy shifts of the order of hundreds of MHz are observed. Using the atomic frequency shift due to the Stark effect, the laser frequency can be tuned for atomic velocity selection. The quadratic Stark effect is the dominating term and the energy change $W$ is given by:

$$W = -\hbar\alpha E^2 \tag{4.9}$$

where $\alpha$, the polarisability, is state dependent. The polarisibility for the micromaser excited state $63P_{3/2}$ has been experimentally determined as $\alpha = 1482 \pm 33$ MHz/$(\frac{V}{cm})^2$ [80]. In some Rydberg states, measurements of the Stark shifts and splittings at low electrical field strength show that the familiar second order expansion is no longer adequate and deviations from the quadratic dependence are found [81, 82, 83]. The fourth-order Stark effect investigations shows good agreement in the case of Ca Rydberg D states , given an interpretation of the hyperpolarisabilities previously observed [84]. In the case of the micromaser ground state, $61D_{5/2}$, the fourth-order contributions has to be taken into account. The energy change $W$ is then given by:

$$W = -\hbar\alpha E^2 - \hbar\gamma E^4 \tag{4.10}$$

where $\gamma$ is the hyperpolarisability.

The frequency locking of the Rydberg laser system (the U.V laser for the upper maser state, $63P_{3/2}$ and the blue laser for the maser ground state, $61D_{5/2}$) is achieved in the so-called auxiliary chamber, shown in figure 4.3. A small fraction of the atomic beam, highly collimated, interacts with the laser light in presence of an external electric field created between two parallel condensator plates. At the end the Rydberg atoms are detected using the same field-ionization technique as described in Chapter 3. The laser is then locked on the maximum of the spectroscopy signal using a traditional lock-in demodulation technique. The frequency tuning is then controlled via the Stark voltage as the spectral lines are shifted.

The second order shift is always to lower energy (redshift), as expected from oscillator strength sum rules [85]. The Doppler shift can be either blueshifted or redshifted depending on the relative angle $\theta$ between the light propagation and the atomic beam axis. For too large electrical fields, a splitting between

the $JM$ and $JM'$ sub-levels of the Rydberg states is observed, which is a drawback for the laser frequency locking scheme as the spectroscopic signal is broadened and the amplitude of the individual sub-levels decreases. An excitation angle set to 11° allows a tuning of the transition resonance to the required frequencies with moderate Stark voltage.

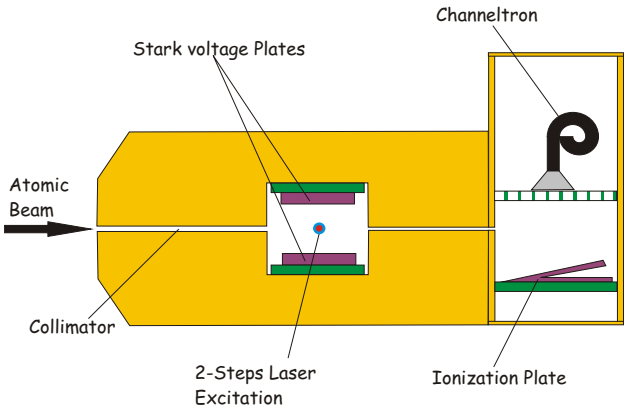


Figure 4.3: *Auxiliary chamber setup for the frequency stabilization of the Rydberg laser, using the Stark effect as frequency tunning*

**Time of Flight Measurement**

The relation between the interaction time $\tau_{int}$ and the Stark voltage $U_{St}$ can be written from equation 4.10 as:

$$\tau_{int} = P1 + \frac{P2}{U_{St}^2} + \frac{P3}{U_{St}^4} \tag{4.11}$$

where the $P_{1,2,3}$ parameter dependent on details of the experimental setup and are subject to changes from day to day operation, depending on not fully controllable parameters like the small deviation of the excitation angle or electrical stray fields in the Stark effect region due to *Rb*-deposition on the electrical plates. Therefore a day to day calibration of the Stark voltage has to be done using a time of flight measurement.

This can be done with a pulsed experiment where the time of flight of the atoms from the laser excitation region to the detectors is measured. The blue laser is mechanically chopped and a small part of the light is sent into a photodiode triggering the experiment as a start signal for the clock as the atom is excited into the Rydberg state. The clock is then stopped once an atom is detected and the elapse time measured corresponds to the effective time of

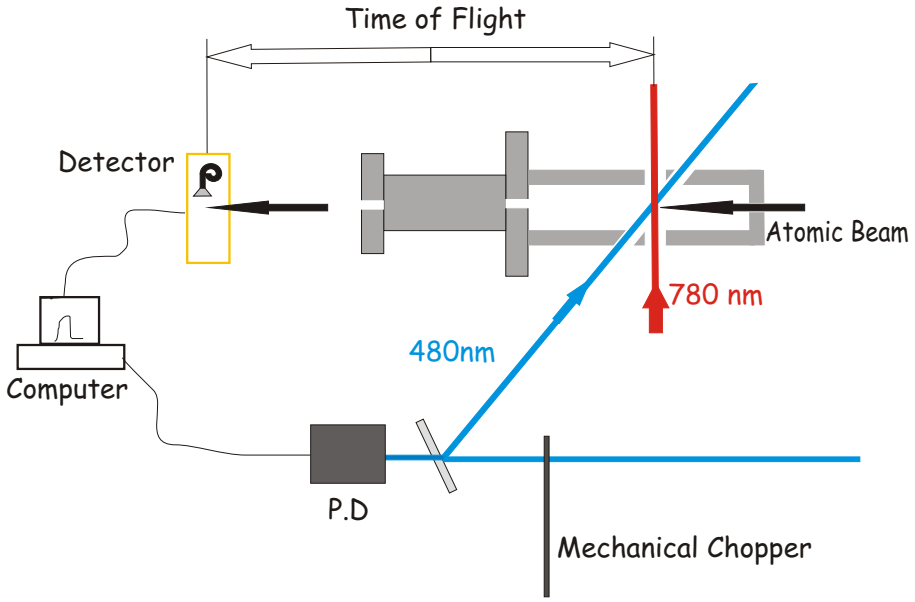


Figure 4.4: *Time of flight experimental setup. The blue laser interacts with the atomic beam at an 11° angle. A mechanical chopper is used, creating $\mu$s light pulse. A photodiode linked to a computer records a fraction of the pulse triggering the experiment. Rydberg atoms are then detected and the time elapsed between the photodiode signal ad the detection click, measures their time of flight.*

flight of the atoms from the excitation region till the arrival in the detection region. Figure 4.5 shows the histogram resulting from different measurements.

For the generation of the uniformly time spaced laser pulses, a mechanical beam chopper is used. The pulsed length has to be on the same order as the Doppler broadening due to the laser linewidth: $\delta\tau_l \sim 5$ $\mu$s. The separation time between two pulses has also to be much larger than the mean time of flight of the atoms which is of the order of several hundreds of $\mu$s. Therefore the following values were chosen: the laser pulse width is set to 5 $\mu$s (FWHM) and the separation between the pulses is 20 ms.

The width of the measured time of flight spectrum can be explained by the Doppler equation and the finite laser linewidth combined to the thermal velocity distribution inside the atomic beam. At a finite angle, the Doppler shifts seen by the fastest atoms will be larger and the velocity distribution will then correspond to a broader frequency distribution than for the slower one.

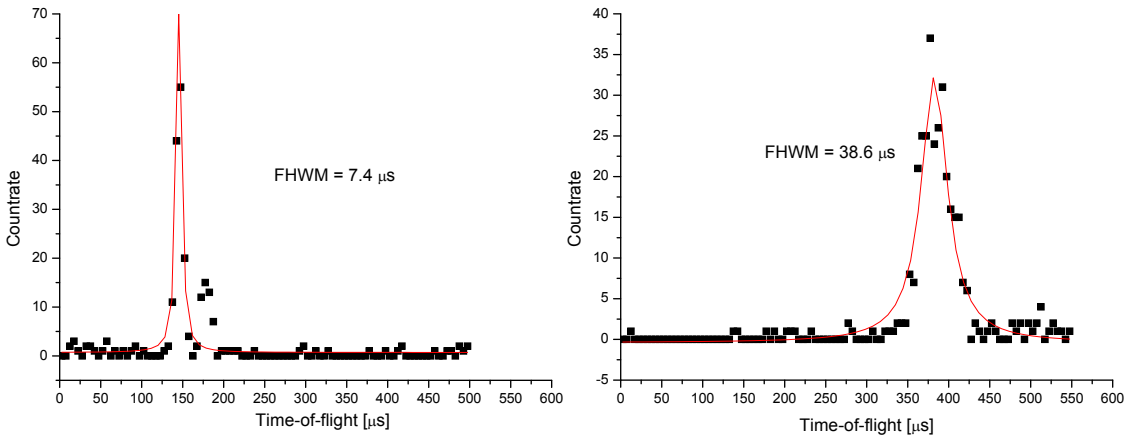


Figure 4.5: *Time-of-Flight Measurement with* $61D_{5/2}$ *Rydberg Atoms: the different linewidth observed between fast and slow atoms is explained by the Doppler equation. Fast atoms see a larger Doppler shift, and the velocity distribution is broadener than for slower atoms. The second peak observed in the left spectrum at* $t_{int} = 180$ $\mu s$ *is explained by the presence of slower atoms excited in the* $61D_{3/2}$ *state.*

The distribution of arrival times is then expected to be broader for the slower atoms:

$$\delta t = \frac{x}{v^2} \frac{c}{\sin\theta} \frac{\delta\nu}{\nu_l} \tag{4.12}$$

The asymmetry observed in the spectrum is explained by the thermal atomic velocity distribution. The laser linewidth is symmetric around the central frequency, however it is not the case of the velocity distribution.

Also, in the spectrum of fast atoms, e.g large Doppler shift, a second velocity component is observed at $t_{int} = 180$ $\mu$s. This corresponds to slower atoms excited in the $61D_{3/2}$ Rydberg state. However, the excitation of the second fine structure component of the $61D$ state is not an issue for the coupling of the atom to the cavity, as the frequency detuning, 51 MHz for the $61D_{3/2} \rightarrow 63P_{3/2}$ transition, is much larger than the Rabi frequency. From the time-of-flight measurement, the statistical contribution of $61D_{3/2}$ atoms to the atomic detection can be extracted and used for the data analysis.

Finally, several such time of flight spectra at different Stark voltages are taken for the calibration. The experimental results are shown in figure 4.6. From the extracted fit parameters, a first evaluation of $\alpha = 782 \pm 58$ MHz$/(\frac{V}{cm})^2$

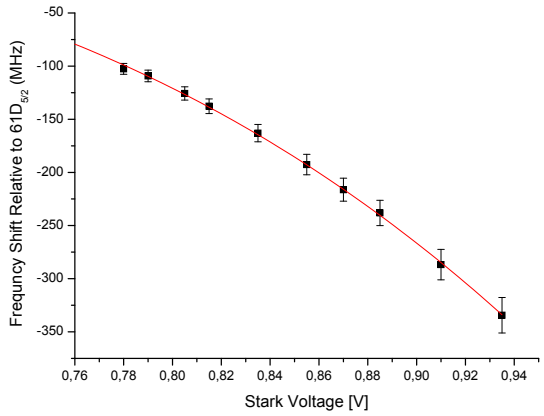


Figure 4.6: *Stark effect frequency shift of the* $61D_{5/2}$ *Rydberg level in an external DC field.*

and $\gamma = 1970 \pm 356$ MHz$/(\frac{V}{cm})^4$ is achieved.

## 4.3 Maser Line with Ground State Atoms

In order to setup the micromaser experiment and tune the cavity frequency on resonance with the atomic Rydberg transition, the resonance curve of the maser (so called "Maser Line") is measured. By changing the applied voltage of the piezoelectric drive, the cavity is slowly quenched and tuned over the resonance frequency. The evolution of the atoms-field coupling is then recorded while monitoring the state-selective ionization signal in the two channeltrons.

The count rate in the two channeltrons corresponding to the two maser states (excited state, $63P_{3/2}$ and ground state $61D_{5/2}$) starts to change in the vicinity of the resonance frequency (21.456 GHz). Ground state atoms start to exchange energy with the thermal cavity field in a coherent interaction through Rabi oscillations.

The observation of maser lines, where excited atoms are injected into the cavity, has a long record in experimental maser physics. The observation of saturation broadening of the maser line demonstrated for the first time the stimulated emission with at most one atom in the cavity [24] and a theoretical description of the maser was published later [14]. However the description of the maser line was their qualitative. Based on the steady-state equation, the maser line features and dependence on the atomic pumping rate can be well understood. The frequency scanning time-scale is much larger than the cavity

dynamics, therefore one can assume that for each frequency the steady-state of the cavity is reached. Replacing the Rabi oscillation contribution (4.5) and (4.6) by the non-resonant term:

$$\mathcal{E}_k = \frac{\mathcal{R}_e}{k}\frac{g^2}{\Omega}\sin^2(\sqrt{k}\Omega\tau) \tag{4.13}$$

$$\mathcal{G}_k = \frac{\mathcal{R}_g}{k}\frac{g^2}{\Omega}\sin^2(\sqrt{k}\Omega\tau) \tag{4.14}$$

where $\Omega^2 = g^2 + \Delta^2$ is the effective Rabi frequency. The steady-state of the field (4.4) can be calculated for any cavity frequency.

When all atomic velocities are present, the average over many oscillation periods of the Rabi frequency is:

$$\lim_{T\to\infty}\int_{-T/2}^{T/2}\sin^2(\frac{1}{2}\Omega\tau)d\tau = \frac{1}{2} \tag{4.15}$$

In the case of ground state atoms pumping the cavity, the steady-state reads:

$$\rho_{nn}^{ss} = \rho_{00}^{ss}\prod_{k=1}^{n}\frac{2\,\Omega^2\,n_{th}\gamma}{2\,\Omega^2\,k\,(n_{th}+1)\,\gamma + g^2\,\mathcal{R}_g} \tag{4.16}$$

This rather simplified approximation showed good agreement with the measured data in the case of excited atoms pumping the cavity giving access to the overall detection efficiency of 45% [30]. In the limit of large detuning, no interaction occurs and the cavity is in its thermal equilibrium. Also, for large pumping parameter, the cavity is cooled down to the vacuum state.

A measured maser line where $61D_{5/2}$ ground state atoms are injected into the cavity is shown in figure 4.7. The injection rate is 450 atoms/s ($\mathcal{R}_g \sim 13$) and no velocity selection is performed. The cavity temperature is 1.3 K, corresponding to a mean thermal photon number $n_{th} = 0.85$. On resonance, ground state atoms start to exchange energy with the cavity field leading to the superposition of ground and excited state due to the Rabi dynamic. A change in the count rate of the channeltrons corresponding to the two states is then observable as the cavity is tuned close to resonance. A large asymmetry for the red-detuned slope is observed. Such large deviations have already been measured for large atomic fluxes of excited atoms [74] where this effect is explained in terms of stray fields in the entrance holes of the cavity.

Performing the measurement of the maser line with velocity selected atoms gives access to the Rabi dynamics of the system. Using the angular excitation, Doppler selected atoms with a well defined velocity, i.e well defined interaction

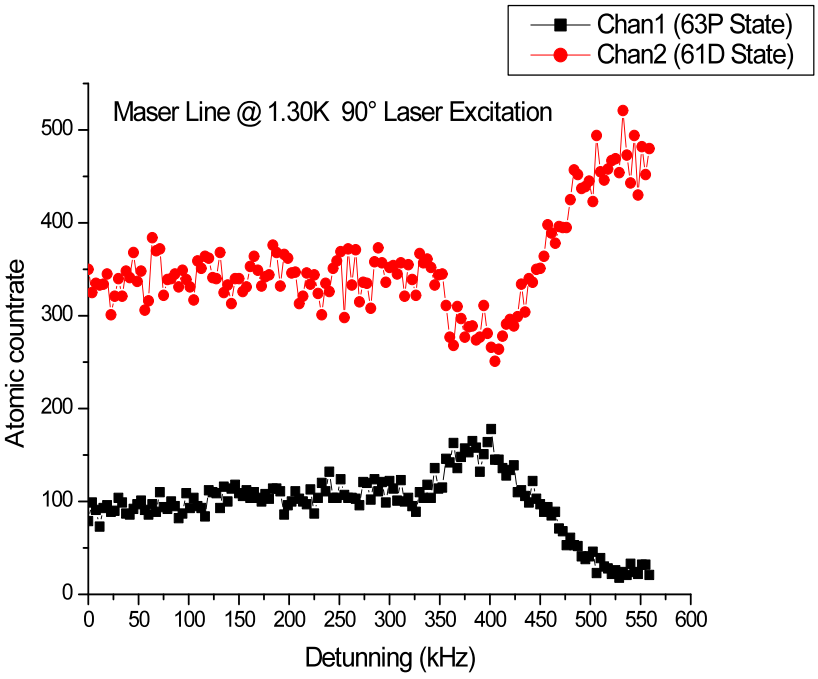


Figure 4.7: *Resonance curve of the maser.* $61D_{5/2}$ *ground state atoms are injected into the cavity and interact with the thermal field at 1.3 K. While the frequency of the cavity is tuned over the resonance* $63P_{3/2}$ *excited atoms are produced .*

time $\tau_{int}$, are injected into the cavity. The recorded spectra are shown in figure 4.8. On resonance, the different interaction times lead to a different inversion which is a direct consequence of the Rabi dynamic between the Rydberg atoms and the microwave field of the cavity and allow to test the cavity steady-state $\rho^{ss}_{n,n}$.

From the measured maser line at a well-defined interaction time with excited maser states, thermal Rabi oscillation at high temperature (2.5 K) were observed in previous experiments [28, 38]. Such measurement were possible as the cavity Q-factor was only of the order of $10^8$, and a higher atomic flux could be used without a pumping effect on the cavity. Also, at higher atomic flux, measurement of the micromaser pump curves were performed, recording velocity selected maser lines [74].

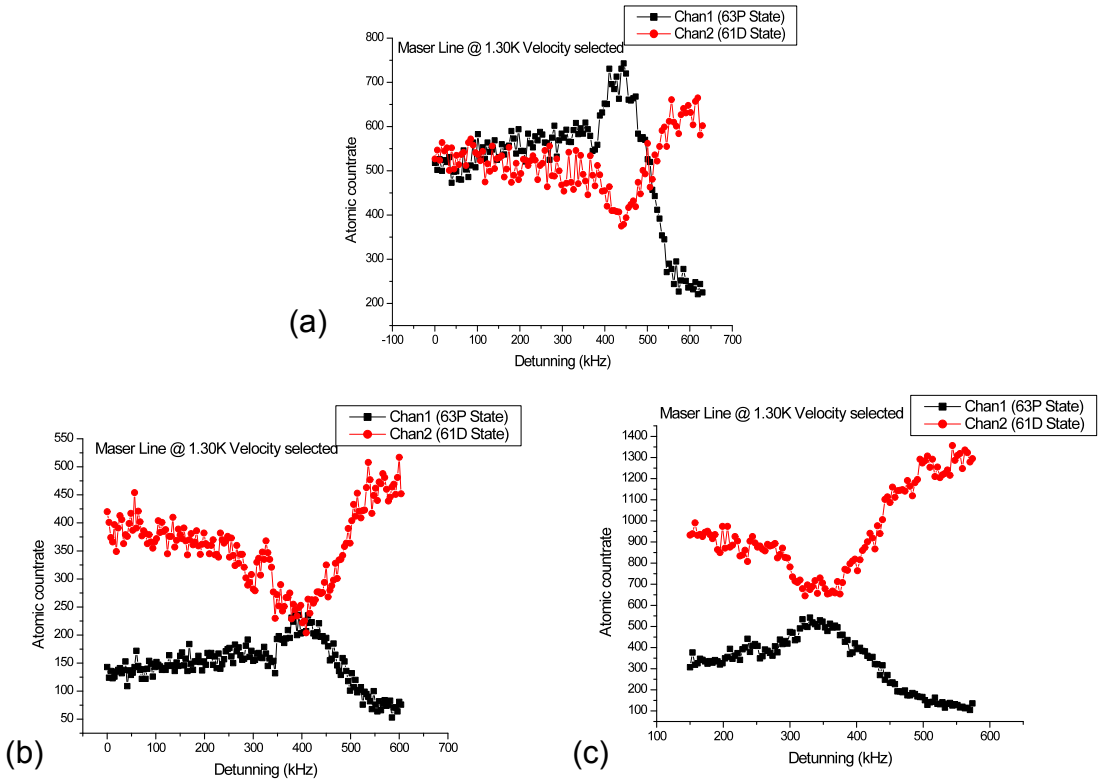


Figure 4.8: *Resonance curve of the maser with velocity selection.* $61D_{5/2}$ *ground state atoms are injected into the cavity and interact with the thermal field at 1.3 K, (a)* $\tau_{int} = 94\mu s$*, (b)* $\tau_{int} = 60\mu s$*, (c)* $\tau_{int} = 50\mu s$*.*

## 4.4 Rabi Oscillations with a Quantized Thermal Field

As discussed in chapter 2, the interaction of a two-level atom with a single mode of the cavity is described by the Jaynes-Cummings interaction. In this model, an atom in presence of a resonant quantum field exchanges periodically energy (Rabi oscillations) and its population oscillates in a coherent way. The realization of high Q cavity where the cavity decay constant $\gamma$ is much smaller than the Rabi frequency allows the realization of this coherent atom-field interaction. It is then possible to demonstrate the quantum nature of coherent light with a collapse and revival of the Rabi oscillations observed using a spin echo measurement scheme [87]. Vacuum Rabi oscillations where an excited state atom $|e\rangle$ interacts with the vacuum field $|0\rangle$ of the cavity are also demon-

strated [29][30] in the micromaser experiment. However, inconsistencies with the theoretical prediction of the vacuum Rabi oscillations remain. One possible explanation is attributed to higher field temperature. Until now, the cavity temperature has been measured with a temperature sensor mounted on the cold finger, giving the temperature of the cavity wall. In fact, the cavity field could be hotter due to outside radiation from hotter surfaces like the atomic oven or microwave waveguides which weakly couple into the cavity. Finally, the mean thermal photon number $n_{th}$ is together with the interaction time $\tau_{int}$ and the atomic rate $\mathcal{R}$ one of the free experimental parameter in the realization of the micromaser and it is therefore important to measure it accurately. To measure the cavity field temperature, $61D_{5/2}$ ground state atoms are used as sensor.

At zero atomic flux, the cavity is in thermal equilibrium, and a blackbody field is present. At 1.3 K, the average number of thermal photons is $\langle n\rangle_{th} = 0.85$ and the cavity state reads:

$$\rho_{th} = \sum_n \frac{\langle n\rangle_{th}^n}{(1+\langle n\rangle_{th})^{n+1}} |n\rangle\langle n| \tag{4.17}$$

and the photon distribution in a thermal field is described by the Bose-Einstein distribution:

$$\begin{aligned} \rho_{n,n} &= \langle n|\rho|n\rangle \\ &= \frac{\langle n\rangle_{th}^n}{(1+\langle n\rangle_{th})^{n+1}} \end{aligned} \tag{4.18}$$

When a ground state atom enters the cavity, interaction with the blackbody field starts, energy exchange occurs and the atomic population starts to oscillate. The atom absorbs a photon and is excited in the upper maser state. The photon can be reemitted and the atom returns into the ground state. Since the unperturbed field temperature of the cavity should be measured, the average photon number should not be changed from one atom to the other. The cavity reaches a thermal equilibrium on a timescale given by its decay time $\gamma = 13$ Hz and an atomic injection rate $R$ much smaller than $\gamma$ is chosen. In the experiment, $R < 1$Hz. This ensures that each atom entering the cavity interacts with the field in thermal equilibrium and not a blackbody field modified under the interaction with the previous atom.

The experimental setup for the measurement of Rabi oscillations is equivalent to the one depicted in figure 4.4, used for the time-of-flight measurement. The laser pulse width is set to 3 $\mu$s (FWHM) giving a limitation to the interaction time resolution. The time between two pulses is set to 100 ms which is

larger than $\tau_f = 73$ms the cavity decay time. Also, the laser intensity is chosen so that less that one atom per pulse is excited into the Rydberg state. The recorded signal is averaged over 1000 events. For each velocity component, the atoms undergo different Rabi cycles. The probability to detect the atom in the ground state is:

$$P_g = \sum_{n=0} \rho_{n,n} \cos^2(\sqrt{n} g\tau) \tag{4.19}$$

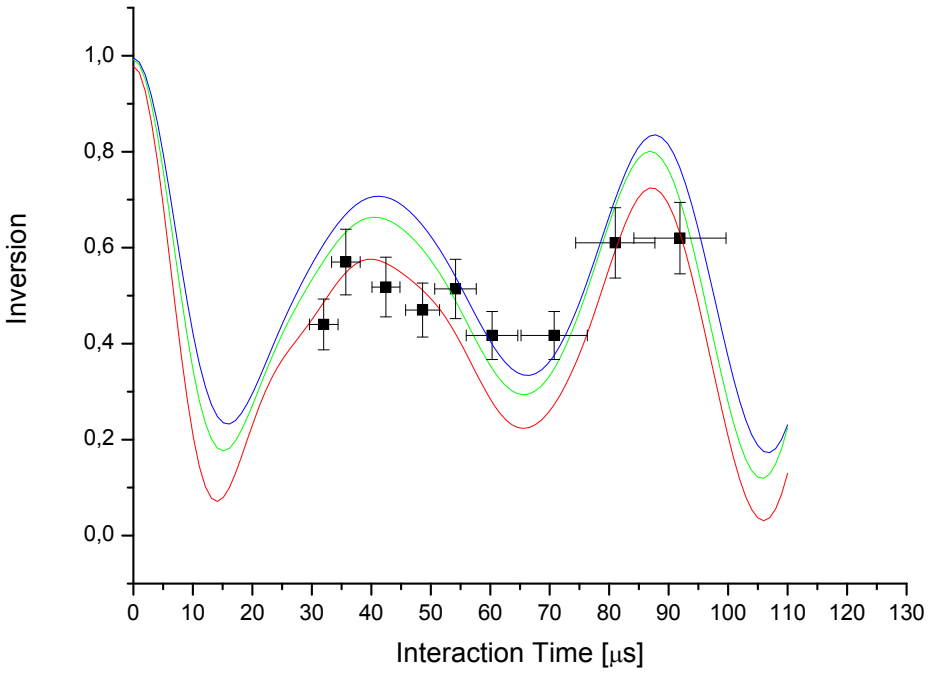


Figure 4.9: *Experimental realization of Rabi oscillations between* $61D_{5/2}$ *maser ground state and the blackbody radiation of the cavity. The temperature of the cavity wall is 1.3K corresponding to* $\langle n\rangle_{th} = 0.85$ *photon. The blue curve shows the theoretical expectation for a Rabi oscillation at this field temperature. The green and red curve show simulations at higher field temperature with* $\langle n\rangle_{th} = 1$ *and* $\langle n\rangle_{th} = 1.37$*, respectively.*

Figure 4.9 shows the realization of Rabi oscillation between ground state atoms and the thermal field of the cavity. The observed quantity is the so-

called inversion giving a detection efficiency independent observation of the dynamics:

$$Inv = \frac{P_g - P_e}{P_g + P_e} = \sum_{n=0} \rho_{n,n} \cos(2\sqrt{n} g\tau) \tag{4.20}$$

The resolution of the measured Rabi oscillations is comparable to the results achieved by Rempe et al. [28], where the observed dynamics at higher temperature was extracted from maser-lines measurement.

The extracted coupling constant $g/2\pi = 7.4 \pm 0.1$ kHz, is in good agreement with theoretically predicted values and with the previous measurement of $\sim 7$ kHz [26, 29, 30].

The extracted average thermal photon number is $\langle n \rangle_{th} = 1.13 \pm 0.14$. The cavity wall temperature measured by a sillicium diode temperature sensor, is 1.3 K and remained constant during the experiment. This corresponds to an average photon number of $\langle n \rangle_{th} = 0.85$. The blue curve represent the realization of such oscillations. Mean photon numbers of $\langle n \rangle_{th} = 1$ and $\langle n \rangle_{th} = 1.37$ correspond to field temperatures of 1.47 K and 1.56 K respectively. Therefore, it can be deduced, that the actual field temperature is slightly higher than the cavity wall temperature. This has to be taken into account when analyzing former Rabi oscillations measurements.

# Chapter 5

# Optical Spectroscopy of Rydberg Atoms

*In Chapter 4, the first cavity QED experiments with maser ground state atoms, the Rydberg $61D_{5/2}$ state, are shown. To perform these experiments, a new diode laser system has been developed leading to the demonstration of a new purely optical spectroscopy method of Rydberg atoms in a room-temperature gas-cell. This new method is based on an electron shelving scheme and is the subject of this Chapter. The excitation of Rydberg states is monitored by observing the absorption of a laser locked on the strong D2 line. Applied to different excitations schemes, this method demonstrates a wide range of applications for Rydberg atoms experiments. In particular, stabilization of a frequency doubled dye laser in the UV to one Rydberg transition is demonstrated.*

Rydberg atoms with principal quantum numbers $n >> 1$ have exaggerated atomic properties. The micromaser experiment takes advantage of the large dipole-dipole interactions that scales in $n^4$ or the long radiative lifetimes that scale in $n^3$. In the last decade, Rydberg atoms start to play a major role for quantum information processes [88]. Taking advantage of the Rydberg atom properties, the implementation of quantum gates between neutral atom qbits was proposed a decade ago [89]. However, until very recently, in the most experiments the detection of the Rydberg atom was done in an indirect destructive electronic scheme where Rydberg atoms are ionized first and the ionizations products are detected electronically afterwards. This includes state selective ionization in a static electrical field as the most common technique, since it combines high detection efficiency and Rydberg states discrimination (see chapter 3) [90]. Therefore, the development of a non-destructive detection scheme of Rydberg atoms is of great interest.

In this chapter, a new method of Doppler-free, purely optical detection of laser excited *Rb* Rydberg atoms in a room-temperature gas cell is presented. The Rydberg atoms are excited from the ground state by the laser systems used in the micromaser experiment, either in a single-excitation step with UV light at 297 nm or in a two or three-step diode laser cascade setup. The detection is performed as the absorption of the 780 nm diode laser on the strong *Rb* D2 line is monitored in a scheme similar to the electron shelving. In the first part, the detection of weak transitions using the electron shelving technique will be introduced. Results of the non-destructive Rydberg spectroscopy of *Rb* atoms in a gas cell will be presented. Finally, the implementation of this new method in the laser stabilization scheme for the micromaser experiment will be explained.

## 5.1 Weak Transition Detection by Electron Shelving

Purely optical detection of high lying atomic Rydberg states has been a difficult task for many years. This is mostly due to the small radial part of the dipole matrix element between the atomic ground state and the highly excited Rydberg states, leading to small absorption cross-sections and therefore poor absorption or fluorescence signals. In early experiments on optical detection of Rydberg transitions with *Ba* atoms, the fluorescence of absorptions lines has been observed in continuous spectra of picosecond laser pulses [91][92]. However, the high temperatures of the glass cell needed to achieve a high atomic density does not allow any sub-Doppler spectroscopy. Doppler-free fluorescence detection has been limited to low-lying Rydberg levels (n=7, 9 and 10) with *Cs* atoms [93].

Weak atomic transition have to be detected as they offer the highest frequency resolution. In atomic optical clocks experiments [17][94] or quantum information experiments based on trapped ions [18] the detection of weak atomic transitions is performed using the quantum amplification of the electron-shelving technique introduced by Dehmelt [19]. Considering a three-level atomic system in a V scheme. The transition $|1\rangle \leftrightarrow |2\rangle$ is the so-called strong transition with $\tau_2$ the atomic lifetime of the state $|2\rangle$, while the transition $|1\rangle \leftrightarrow |3\rangle$ is the so-called weak transition with $\tau_3$ the atomic lifetime of the state $|3\rangle$. The key of the detection scheme is the so-called quantum amplification which occurs when the detected signal is not the absorption or fluorescence caused by the transition itself but the fluorescence emitted on the strong transition. In absence of the weak transition (for example when the laser is off-resonant), the atom undergoes many absorption-emission cy-

cles on the strong transition. In the case of a resonant laser, an excitation on the weak transition hinders many absorption-emission cycles on the strong transition. The atom is in the so-called dark state as the fluorescence signal drops to zero. In single trapped ions experiments, the quantum amplification is given by the ratio $\frac{\tau_3}{\tau_2}$ of the lifetimes of the two excited states and can reach values of $10^6$ or more. In a room-temperature gas cell, conditions are not so clean and atom-atom collisions and interaction time limitations decrease the amplification factor down to values of several hundreds.

The electron shelving technique is a rather simple detection technique taking advantage only of the different lifetime of two excited atomic states. Although the dark-state nomination only comes from the absence of fluorescence observed when the atom is excited along the weak transition. It is not related to the interesting phenomenon in which a coherent superposition of atomic states is responsible for coherent trapping or dark states. Such phenomena rely on the control over the Rabi frequencies driving the three level atomic system. One extension of it is the electromagnetically induced transparency (EIT) where both the Rabi frequencies and the decay of the excited states play a role in the transparency of the medium for the probe field. Doppler-free purely optical detection of Rydberg states has been reported in a room-temperature cell [95] and in an atomic beam apparatus [96] using EIT technique.

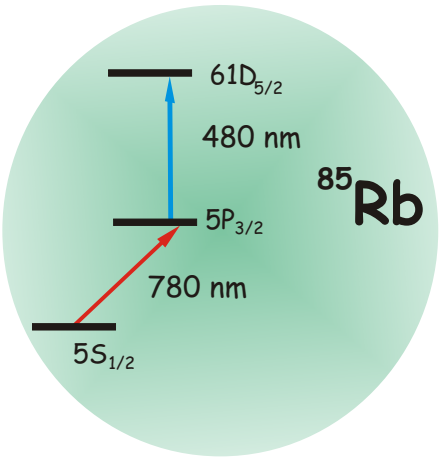


Figure 5.1: *Atomic ladder scheme for the 2-steps excitation and detection of* $^{85}Rb$, $61D_{5/2}$, *Rydberg atoms*

A first breakthrough in the optical detection of Rydberg atoms in room-temperature glass cell was obtained in the C. Addams group where EIT in an atomic ladder scheme was used to create an observable and spectrally narrow signal from Rydberg transitions. However such detection scheme requires high

power laser for the Rydberg transitions to fulfill the condition on the Rabi frequencies. The method proposed here to implement a Doppler-free detection is based on the electron shelving technique used in trapped ions system. A first test experiment was achieved using the two-step excitation scheme for the $^{85}Rb$ Rydberg state $61D_{5/2}$.

**Doppler free detection of the micromaser ground state $61D_{5/2}$ in a $Rb$ gas cell**

The atomic-level scheme is shown in figure 5.1. The 780 nm laser is frequency stabilized to the center of a $Rb$ hyperfine line using Doppler-free saturation spectroscopy in an other setup. Only atoms with zero-velocity component in the direction of the IR and the blue laser can therefore interact with both laser simultaneously and a Doppler-free signal can be obtained.

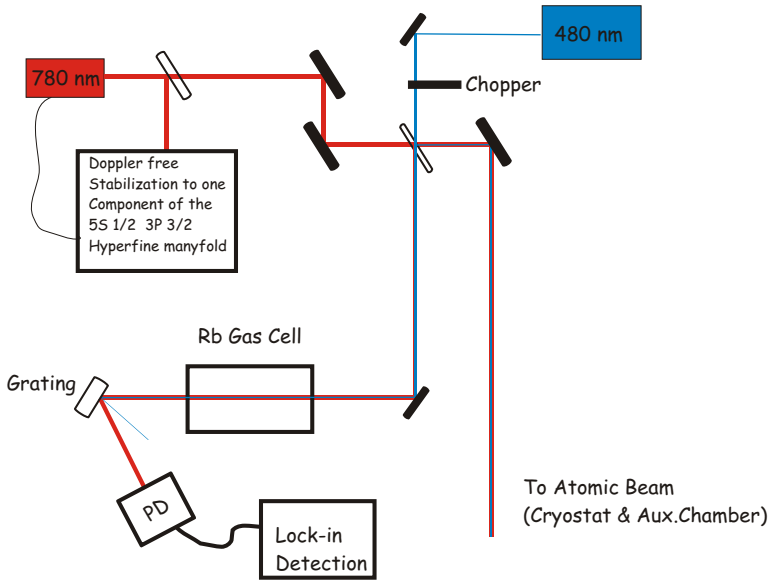


Figure 5.2: *Schematic experimental setup for optical detection of Rb Rydberg atoms in a room-temperature gas-cell*

The main parts of the experimental setup are shown in figure 5.2. The 480 nm radiation is produced by frequency doubling the light from a external cavity stabilized 960 nm diode laser leading to a maximum power of 40 mW. The 780 nm light is produced with a diode laser that is frequency stabilized to the $F = 3 \rightarrow F = 4$ hyperfine component of the $5S_{1/2}$ to $5P_{3/2}$ transitions by means of Doppler-free saturation spectroscopy. Both beams are then collimated to a

diameter of 1 mm and are linearly polarized. The IR is superimposed on the blue light before the cell and separated with a grating after the cell. Scanning the blue laser over the Rydberg transitions excites *Rb* atoms into the Rydberg states and the reduced absorption of the IR beam through the cell can be detected with the help of a photodiode. In order to increase the signal, a lock-in amplified detection technique is performed while the blue light is mechanically chopped.

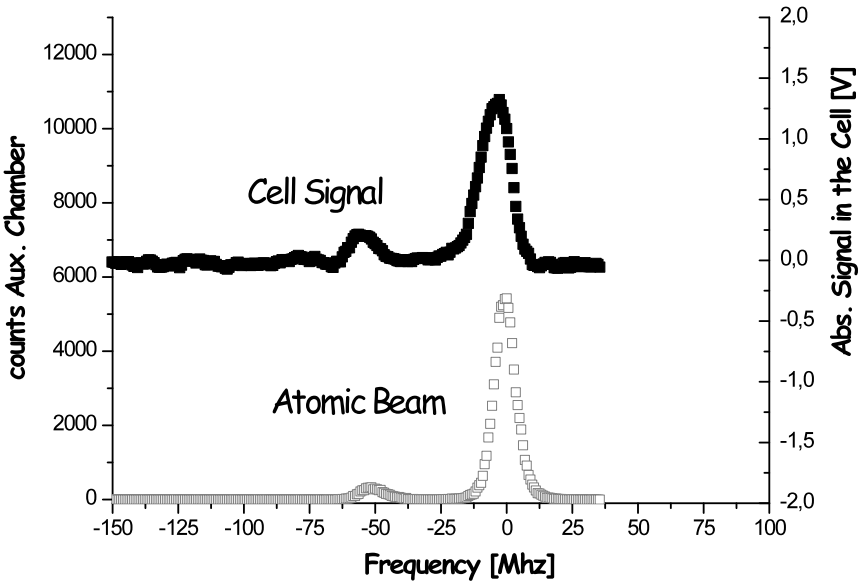


Figure 5.3: *Optical detection of the* $^{85}Rb$ *Rydberg state* $61D_{5/2}$ *in a gas cell. The absorption signal is compared to the spectroscopy signal observed with an atomic beam experiment.*

Figure 5.3 shows the excitation into the $^{85}Rb$ $61D_{5/2}$ Rydberg state. The spectroscopy is recorded at the same time both in a glass cell and with an atomic beam experiment as reference, demonstrating the feasibility of a non-destructive optical spectroscopy of Rydberg atoms in a room-temperature gas cell based on a purely optical detection scheme.

## 5.2 Non-Destructive Spectroscopy of Rydberg Atoms

Once a proof of principle experiment is realized in a two-step excitation scheme, the extension to other excitation schemes is discussed in this section. In addition, it is shown, how optical pumping can be used to excite only one single hyperfine level in the Rydberg hyperfine manyfold. As these hyperfine states are separated by just a few kHz, they are usually not resolved spectroscopically.

### Optical Spectroscopy with a 297 nm UV Laser

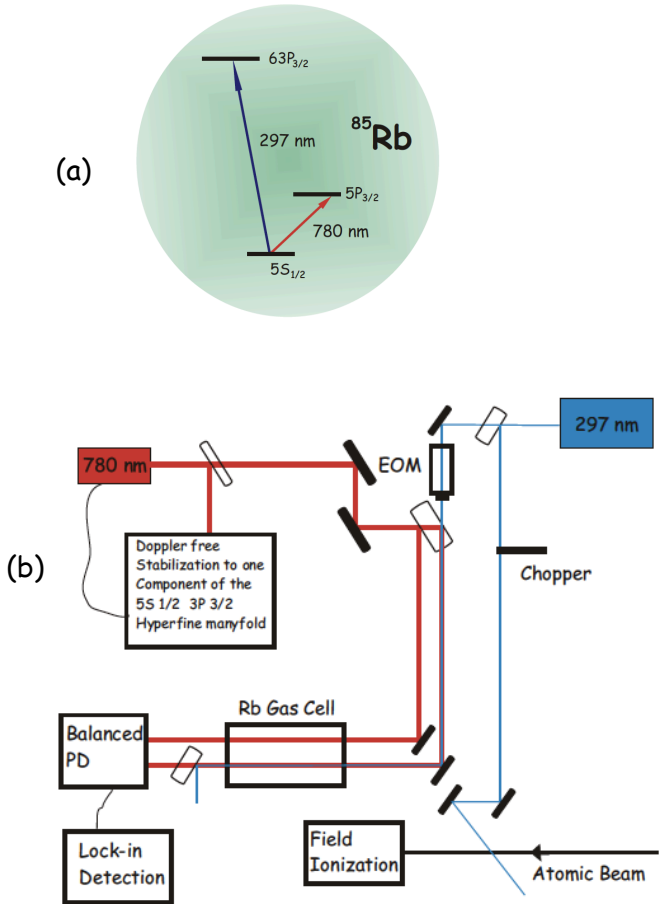


Figure 5.4: *(a) Level atomic V scheme for the excitation and detection of* $^{85}Rb$*,* $63P_{3/2}$*, Rydberg atoms; (b) schematic experimental setup for optical detection of UV-Rydberg transitions in a room-temperature gas cell*

The atomic scheme and the main parts of the experimental setup are shown in figure 5.4. The 297 nm radiation is produced by frequency doubling the light from a rhodamine 6G dye laser (Coherent 899 ring laser) in a separate enhancement cavity with a BBO crystal (LAS Wavetrain SC), leading to a maximum power of 45 mW of UV radiation. The 780nm is produced and locked as previously described. Both the IR and the UV beam are collimated to a beam diameter of 1 mm and are linearly polarized. Before entering the quartz glass cell, the IR light is split into two beams of equal intensity, and after the cell their differential absorption is measured with a balanced detector (Thorlabs PDB 150 A). One of the beam is superposed with the UV light before entering the glass cell. After the cell the two beam are separated with a mirror showing a high reflectivity coating for the UV radiation, meanwhile having a high transmission for the IR. The UV light is then scanned cross the Rydberg lines. The electron shelving based detection is then performed as the reduced absorption of the IR beam superposed on the UV beam, due to the Rydberg excitation, can be detected on the balance detector. To enable lock-in amplified detection techniques, the UV light can be chopped using a electro-optical-modulator (EOM, LINOS LM 13 P UV), or frequency modulation can be applied to the dye laser control electronics board.

Figure 5.5 shows the excitation of the $^{85}Rb$ $63P_{1/2}$, $63P_{3/2}$ fine structure doublet. In figure 5.5 (a) the UV laser light is periodically interrupted with a frequency of 6 kHz., the signal observed being the output voltage of the lock-in amplifier observed in phase with the interruption signal. The observed fractional change of the transmission of the two IR beams through the 10 cm long glass cell is in the order of $10^{-4}$ confirming the quantum amplification factor of 100 expected under such experimental conditions.

The frequency resolution is limited by the linewidth ($\delta\nu_{D2}$) of the $Rb$ $D2$ line. The natural linewidth $\delta\nu_{D2,nat}$ is 7 MHz. Assuming that the frequency of the 780 nm IR laser is stabilized on the center of one transition, it will interact with atoms in a velocity range $v = 0 \pm \delta v$, where the Doppler shift corresponding to $\delta v$ has to be within the linewidth $\delta\nu_{D2}$. As for the electron shelving scheme both laser have to interact with the same atoms, Rydberg transitions can only detected for atoms within the same velocity range. Therefore a minimum linewidth to be expected reads:

$$\delta\nu_{UV,min} = \frac{\delta\nu_{D2,nat}\nu_{UV}}{\nu_{IR}} = 18MHz \tag{5.1}$$

Different broadening mechanisms of Rydberg transitions were also examined using a thermionic detector [97]. At room temperature, values below 10 MHz were found, so that the velocity selection limited by the natural linewidth of the $D2$ line is the dominant factor contributing to the observed linewidth.

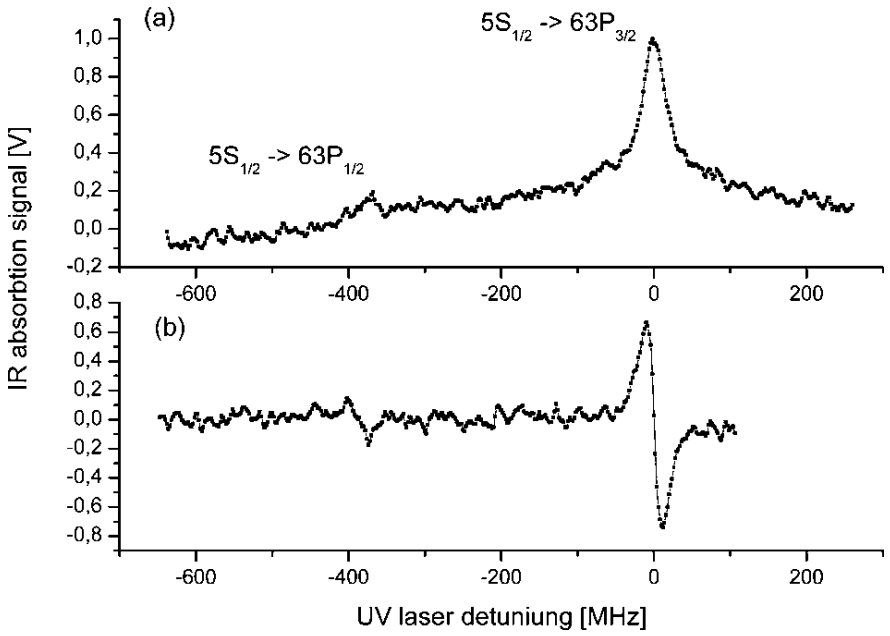


Figure 5.5: *(a)Absorption signal with a chopped UV laser; (b) absorption error signal with a frequency-modulated UV laser*

In figure 5.5 (b), the UV light is frequency modulated at a frequency of 420 Hz and a modulation depth of 1 MHz. Applying the lock-in detection results in a dispersive signal that can be used as an error signal for frequency stabilization of the dye laser. The zero crossing can be determined with an uncertainty better than 2 MHz for an averaging time of 300 ms. As the specified short-term linewidth of the dye laser is 1 MHz at 594 nm, this error signal can be used to compensate the frequency drift of the dye laser on the scale of its short-term linewidth [20]. In the next section the application of this locking scheme for the micromaser experiment will be explained in more detailed.

### Spectroscopy of *Rb* Rydberg States with three Diode Lasers

The excitation of *Rb* Rydberg levels with a three-step diode laser system has many advantages over a one-step UV laser setup. First, as mentioned in chapter 3, diode lasers are easier to maintain and need less alignment work in everyday operation. Second, higher excitation rates are obtained [30]. Finally, by controlling the polarizations of the three lasers, excitation of a single hyperfine level out of the hyperfine manifold is possible. To excite the same

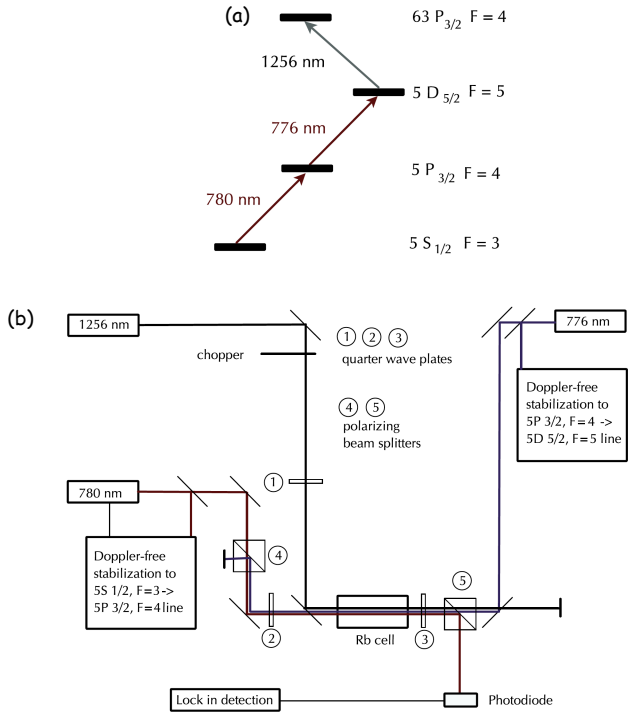


Figure 5.6: *(a) Level scheme for the excitation of Rb Rydberg states in a three laser cascade setup; (b) Laser setup for optical spectroscopy of Rb Rydberg atoms in a gas cell. The 780 and 776 nm lasers are frequency stabilized in separate setups. These laser are counter propagating and their $\sigma^+$, $\sigma^+$ polarization is realized by two $\lambda/4$ plates. The 1256 nm laser can be applied from both sides.*

$63P_{3/2}$ state as with the UV laser, the dipole selection rules impose to use three excitation steps.

The experimental setup is shown in figure 5.6 (b). All three lasers are grating-stabilized diode lasers (Toptica DL 100) equipped with standard diode laser control electronics (Toptica DCC 100, DTC 100, SC 100). The first laser is resonant with the $F = 3 \rightarrow F = 4$ hyperfine component of the D2 line in $^{85}Rb$, and the laser is frequency-stabilized using Doppler-free saturation spectroscopy.

The second stage is resonant with the $5P_{3/2} \rightarrow 5D_{5/2}$ transition at 775.8 nm. As the lifetime of the $5D_{5/2}$ is 10 times longer as that of the $5P_{3/2}$ level, its spectroscopic detection in a gas cell is already more challenging. Many groups use the 420 nm fluorescence emitted when the $6P$ levels, which are populated from the $5D$ levels, decay back to the $5S$ ground state. Here, a different

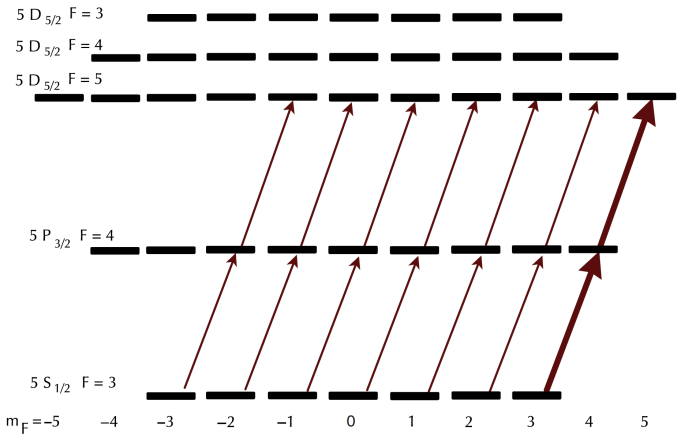


Figure 5.7: *Level scheme of $^{85}Rb$ including magnetics sublevels. If the population of the magnetic sublevels in the $5S_{1/2}$ state is transfered to the $m_F = 3$ sublevel by optical pumping with $\sigma^+$ polarized light, $\sigma^+$ polarized light in the second stage can only excite the $5D_{5/2}$, $F = 5$, $m_F = 5$ state.*

approach is used, observing the transmission of the 780 nm laser through the cell as the frequency of the 776 nm laser varies. Also here the different lifetimes of the excited atomic levels give rise to a quantum amplification factor of 10, so increasing the signal to noise ratio. Compared to the 420 nm fluorescence detection, the 780 nm absorption detection gives comparable results in terms of resolution and signal to noise ratio. Since no photomultipliers are required and a simple analogue photodiode signal can be used for further signal processing in the frequency stabilization, spectroscopy is performed with the second method.

Whereas the hyperfine splitting of the $5P_{3/2}$ level is easily resolved in Doppler-free spectroscopy, the hyperfine splitting of the $5D_{5/2}$ is only of the order of 10 MHz and therefore more difficult to resolve. In figure 5.8, two spectra of the $5D_{5/2}$ line are compared. In the first spectrum, the two lasers have a $\sigma^+$ polarization, with the quantization axis chosen along the propagation direction of the first stage. In this case, shown in figure 5.7, optical pumping and selection rules ensure that only the $m_F = 5$ sublevel of the $5D_{5/2}$, $F = 5$ level can be excited and the linewidth of the transition is below 10 MHz. The second spectrum shows by using a linear polarization of the 780 nm laser: one can excite all three hyperfine components of the same transition and three peaks can be resolved in the spectrum. The measured data can be explained by adding three Lorentzian lines with separation of 9.4 MHz and 18.4 MHz. This corresponds to the value of the hyperfine splitting of the $5D_{5/2}$ line [98]. By using a $\sigma^+$, $\sigma^+$ setup, the frequency of the laser can be stabilized on the

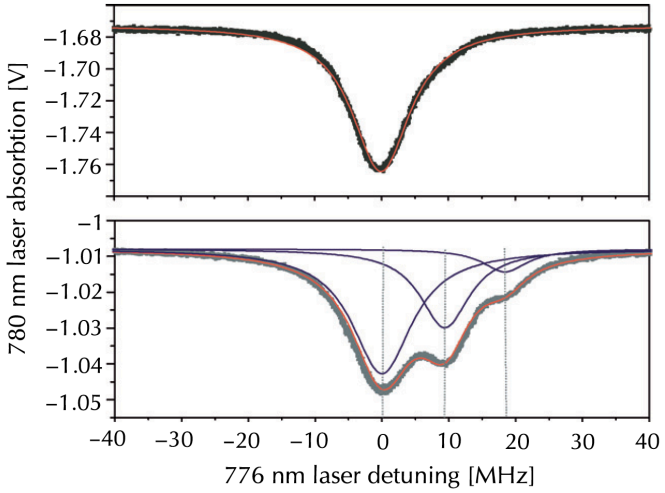


Figure 5.8: *Spectroscopy of the $5D_{5/2}$ levels with two diode lasers. In the upper plot, optical pumping with a $\sigma^+$ polarized 780 nm laser ensures that only the $5D_{5/2}$, $F = 5$ level is excited. In red a Lorentzian line fitted to the measured data is shown, the width of the fitted curve is 10.5 MHz. In the lower plot, the polarization of the 780 nm laser is linear, so that no optical pumping to the extremal $m_F$ occurs. As a consequence, all hyperfine sublevels of the $5D_{5/2}$ state can be resolved. In red a sum of three Lorentzian lines with frequency separations according to the hyperfine splitting of the $5D_{5/2}$ level is shown. In blue the individual Lorentzian lines contributing to this line are displayed*

$5P_{3/2}, F = 4 \rightarrow 5D_{5/2}, F = 5$ transition and excite the Rydberg states via a well-defined path.

The two beams can be combined and separated by using two polarizing beam splitters and two quarter wave plates as shown in figure 5.6 (b). The quarter wave plates are aligned so that the first one transfers the linearly polarized light, which has been transmitted by a polarizing beam splitter, into left-circularly polarized light, corresponding to $\sigma^+$ polarization if the quantization axis is chosen along the propagation axis. The second quarter wave plate, placed after the *Rb* glass cell, is oriented in the same way as the first one, reflecting the 780 nm by the second polarized beam splitter. This second quarter wave plate transforms the counter propagating 776 nm light into right-circularly polarized light, corresponding to $\sigma^+$ as the quantization axis was chosen along the 780 nm laser. This scheme is used both for the frequency stabilization of the 776 nm laser and for the Rydberg spectroscopy with three diode lasers.

After stabilization to the selected atomic transition, the 780 and 776 nm laser are superposed with the 1256 nm laser and the lasers interact with *Rb* atoms in a 15 cm room-temperature gas cell. To increase the excitation rate into the Rydberg levels, all lasers are focused within the *Rb* cell with lenses of focal length 30 cm. After the cell, the three beams are separated again by polarization-and wavelength selective elements and only the absorption of the 780 nm laser is used for the signal analysis. To enable a lock-in detection, the 1256 nm laser is mechanically chopped at a frequency of 1130 Hz. The absorption of the 780 nm laser is detected in phase with the chopping frequency and the demodulation time is set to 300 ms in each case. The motion of the atoms limits the interaction time of individual atoms with the light fields to timescales of 1 $\mu$s. This is much shorter than the periodicity of the chopping process on the observed lineshape. The frequency scan of the 1256 nm laser is calibrated by observing the transmission of a nearly plane-parallel Fabry-Perot interferometer with a free spectral range of 287 MHz.

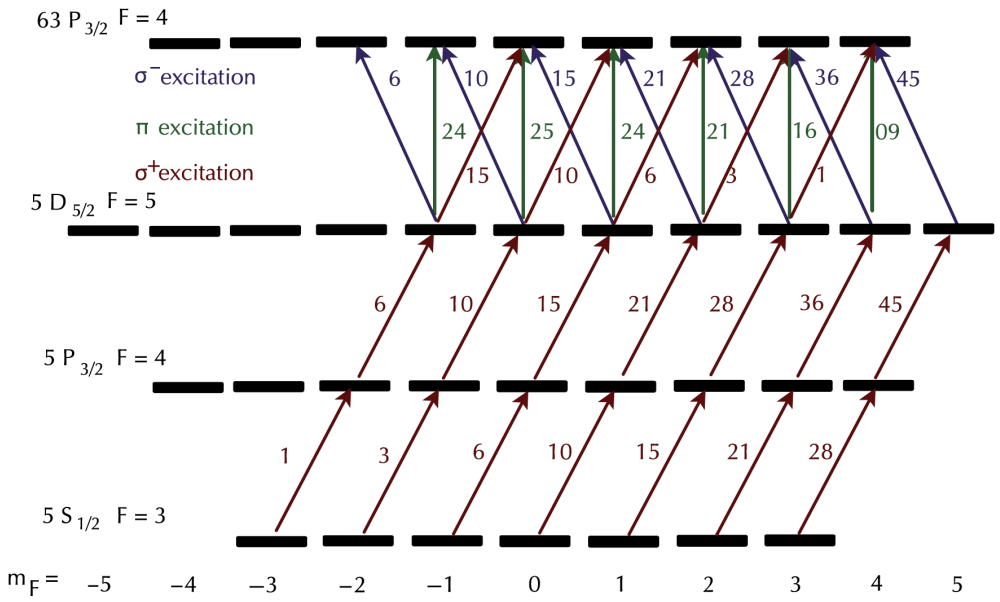


Figure 5.9: *Level scheme of* $^{85}Rb$ *including magnetic sublevels. By optical pumping and dipole selection rules one particular hyperfine level of the* $5D$ *and* $63P$ *levels can be selected. The angular part of the excitation probabilities is also given, showing that a* $\sigma^+$, $\sigma^+$, $\sigma^-$ *scheme gives the highest excitation probability*

Figure 5.9 shows the three-step excitation path and includes the angular

part of the relative excitation probabilities [99, 100]. It can be seen that by optical pumping on the 780 nm transition to the $m_F = 3$ substrate, one can realize the excitation path with the highest excitation probability. In addition, one can selectively address the $63P_{3/2}$, $F = 4$ hyperfine level of the Rydberg state.

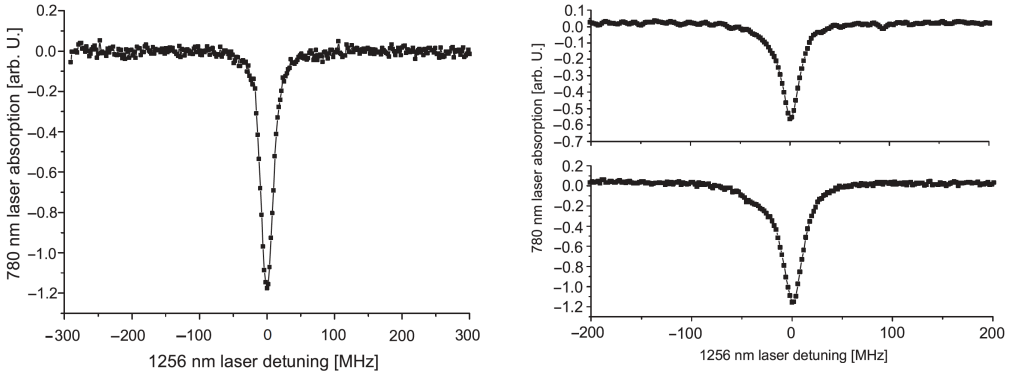


Figure 5.10: *(a)-left, absorption signal from the* $63P_{3/2}$ *Rydberg state in a room-temperature gas cell obtained with a three diode laser cascade setup. The 1256 nm laser is applied co-propagating with the 780 nm laser. (b)-right absorption signal from the* $63P_{3/2}$ *Rydberg state in a room-temperature gas cell obtained with a three diode laser cascade setup. The 1256 nm laser is applied counter propagating with the 780 nm laser. In the lower plot the power of the 776 nm laser is increased far above saturation. in this case an asymmetry in the line can be observed which is due to the excitation of the same final state via a different hyperfine sublevel of the intermediate* $5D_{5/2}$ *state*

To achieve a compromise between frequency resolution and good signal strength, the power of the first stage is chosen just below saturation intensity. The power of the second stage and third stage are 2 and 5 mW, respectively. After superposing the counter propagating 780 and 776 nm lasers with $\sigma^+$ polarization one has the freedom to apply the 1256 nm laser from both sides. Figure 5.10 (a) shows an excitation spectrum of the $63P_{3/2}$ level if the third laser is applied co-propagating with the first one, while in figure 5.10 (b), it is applied counter propagating with the second laser. In each case the polarization of the 1256 nm laser has be tuned to $\sigma^-$ to avoid a dark state. The two excitation geometries give rise to approximately the same signal-to-noise ratio and also the frequency width of 20 MHz (FWHM) is similar in both cases. In figure 5.10 (b), it can be seen that an increased power of the 776 nm laser leads to an asymmetric line shape, which can be attributed to different excitation paths via different hyperfine levels of the $5D_{5/2}$ state [21].

In addition to the $P$ levels, the Rydberg $F$ levels can be reached with a three-step excitation as well. Figure 5.11 shows a spectrum of the $60F$ state, which is detuned 11.5 GHz below the $63P$ state. In this case linear polarization has been chosen for all three lasers and all lasers are co-propagating.

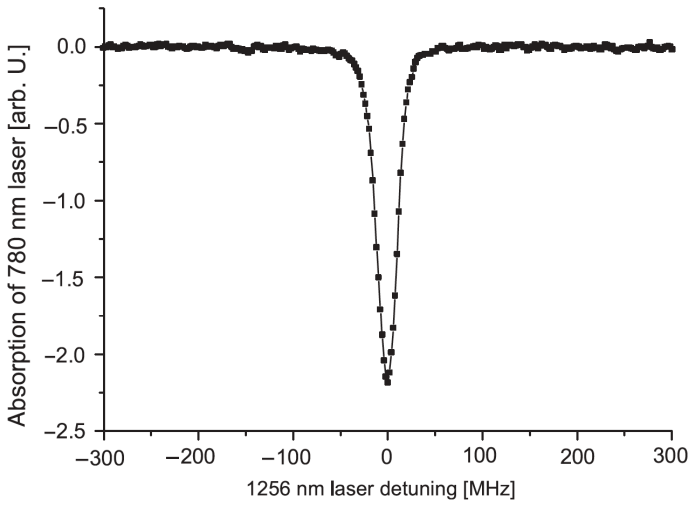


Figure 5.11: *Excitation signal from the* $60F$ *Rydberg state in a room-temperature gas cell obtained with a three diode laser cascade setup.*

The quantum amplification effect, which has already been described above, is also responsible for the observation of the Rydberg transitions in a three-step excitation setup. As an excitation to the $5D$ state already hinders 10 absorption and emission cycles on the D2 line, the quantum amplification for the three-step excitation is expected to be reduced by the same factor if compared with the single-single step excitation in a $V$ scheme. Nevertheless, the available interaction time in the cell of about 1 $\mu$s in a focused laser beam leaves enough time for a quantum amplification effect of about 50, which explains the good signal-to noise ratio in the observed spectra.

## 5.3 Applications to the Micromaser Experiment

In the previous section the optical spectroscopy of Rydberg atoms in a gas cell is demonstrated. This method presents also the advantage that Rydberg transition in a gas cell are highly immune to linear and quadratic DC-Stark shifts [95], giving these Rydberg lines an unexpectedly high frequency stability

and this method can be used for frequency-stabilization of laser to Rydberg transitions. This is due to a screening effect or electrostatic screening created by the thin film layer of *Rb* atoms formed on the surface of the glass cell, reducing the electrostatic field. Like the electric field of the nucleus is reduced inside an atom due to the shielding effect, the electric field in the conducting *Rb* film layer is further reduced by the cloud of conduction electrons. The Rydberg atoms remain sensitive to AC-Stark effect, and electro-optic effect such as Kerr effect have been recently observed [101].

The dispersion signal observed in figure 5.5 can be utilized as an error signal to stabilize the frequency of the 297 nm laser to the $5S_{1/2} \rightarrow 63P_{3/2}$ transition in $^{85}Rb$ used in the micromaser experiment. The demodulation time of the lock-in amplifier is set to 300 ms, limiting the bandwidth of the servo loop below 10 Hz. The error signal is given to a proportional-integral-derivative (PID) regulator (SRS SIM 960) that acts as an external-frequency control voltage for the dye laser. The frequency stability of the laser can be tested by exciting Rydberg atoms in an atomic beam apparatus where the atoms are detected via state-selective ionization and performing a time of flight experiment. By setting an angle of 11° between the laser and the atomic beam, the resonance frequency of the atoms in the beam is Doppler shifted with respect to atoms at rest. As the linewidth of the laser is much smaller than the Doppler width of the thermal atomic beam, velocity selection of the excited Rydberg atoms is made by tuning the laser frequency. The velocity spread of the excited atoms is then a direct measure of the frequency stability of the exciting laser and can be used to test the performance of the laser stabilization in the gas cell; the Doppler width due to the angular divergence of the atomic beam is less than 1 MHz.

The typical velocity range of the thermal atomic beam is 200 m/s to 600m/s leading to a Doppler shift at 297 nm in the range of 200 to 600 MHz which corresponds to a Doppler shift in the IR at 780 nm in the range of 80 to 200 MHz. To lock the UV laser in the gas cell, the atoms have to be resonant with both lasers and therefore have to see the same Doppler shift. One solution would be to use an acousto-optic modulator (AOM) to shift the IR frequency. However the large frequency shift required combined with the large spectral bandwidth of the full velocity range would require the implementation of many AOMs. An alternative and more elegant method to achieve locking of the UV laser to Doppler-shifted frequencies, is to use a technique that is similar to the well-known crossover resonances in Doppler-free saturation spectroscopy. Using the hyperfine manyfold of the D2 line $F = 3 \rightarrow F = 2, 3, 4$ transition in $^{85}Rb$ shown in figure 5.12, the IR laser is no longer stabilized to the $F = 3 \rightarrow F = 4$ hyperfine component of the $5S_{1/2} \rightarrow 5P_{3/2}$ transition but to either the $F = 3 \rightarrow F = 3$ component with detuning of 121.6 MHz or the

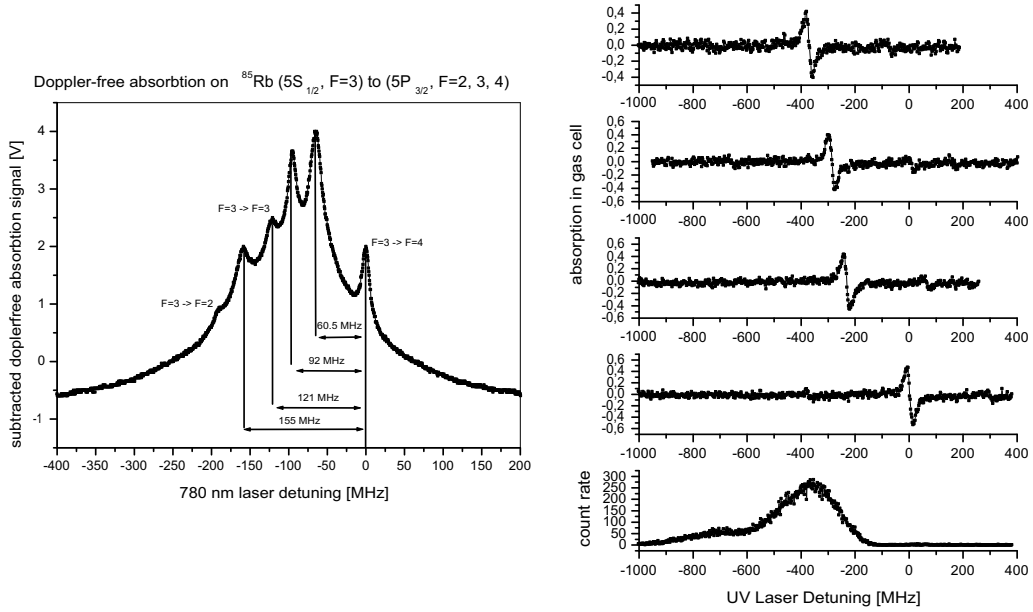


Figure 5.12: *Left; the hyperfine manyfold of the D2 transition line in* $^{85}Rb$*. Right; (a) Doppler-shifted signal from an atomic beam under angular excitation; (b)-(e) shifted dispersive signal from a gas cell with a 780 nm laser locked to (b)* $F = 3 \rightarrow F = 4$ *resonance, (c)* $F = 3 \rightarrow F = 2, 4$ *crossoverline, (d)* $F = 3 \rightarrow F = 3$ *resonance, and (e)* $F = 3 \rightarrow F = 2, 3$ *crossoverline*

$F = 3 \rightarrow F = 2, 4$ and $F = 3 \rightarrow F = 2, 3$ crossoverlines with frequency detuning of 92.5 MHz and 153.3 MHz, respectively. The $F = 3 \rightarrow F = 4$ is now resonant with atoms having a well-defined velocity and the UV Rydberg transition is Doppler shifted by a frequency of:

$$\Delta\nu_{UV} = \Delta\nu_{IR}\frac{\nu_{UV}}{\nu_{IR}} \tag{5.2}$$

Figure 5.12 shows the Rydberg excitation signal in the gas cell for different frequencies of the IR laser and, for comparison, the spectrum obtained from an atomic beam under angular excitation. It is clearly seen that the Doppler shifted dispersive signal can be used to lock the UV laser on a frequency that allows velocity-selective excitation in an atomic beam. With these lines, one single AOM can be enough to cover the Doppler shifts of the hole velocity spectrum of the atomic beam.

By making short UV excitation pulses of 5 $\mu$s duration with a mechanical chopper and detecting the atoms 10 cm behind the excitation region, a time-of-flight spectrum can be recorded with the same method described in

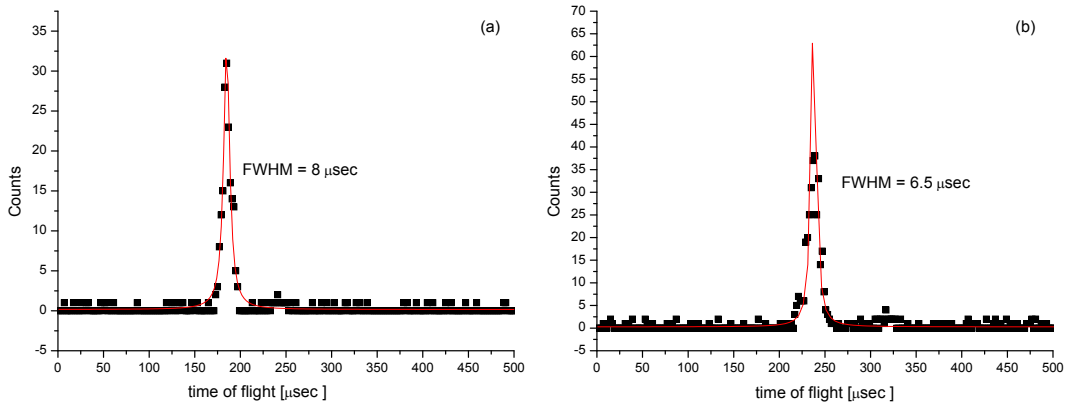


Figure 5.13: *Time-of-flight spreding of Rydberg atoms after velocity selective excitation in an atomic beam; (a) the IR laser is locked on the* $F = 3 \rightarrow F = 2, 3$ *crossoverline with UV laser detuning of 402 MHz ; (b) the IR laser is locked on the* $F = 3 \rightarrow F = 3$ *resonance with UV laser detuning of 319 MHz*

Chapter 4 to measure Rabi oscillations. Figure 5.13 shows the distribution of arrival times for UV laser detuning of 402 MHz (left) and 319 MHz (right). From the width of this distribution (6.5-8 $\mu$S), the laser frequency stays within a frequency window of 2 MHz in the UV over recording times of several hours. As this number coincides with the short-term frequency stability of the frequency-doubled dye laser, the long-term frequency stabilization of the laser on the level of its short-time linewidth is demonstrated. The results compare also very well with the results obtained by stabilizing the laser frequency to the signal obtained from state-selective ionization in an atomic beam, with the advantage of a much simpler setup, involving no vacuum chamber and no cryogenic cooling.

# Chapter 6

# Quantum Trajectories

*Parallel to the realization of cavity QED experiments with ground state atoms and the development of a new spectroscopy method of Rydberg atoms in a gas cell, a numerical and theoretical work supporting the ongoing experiments has been achieved. The time dependence of the micromaser field can not be solved analytically and therefore numerical treatment has to be performed. For the study of the micromaser linewidth and the measurement of the phase diffusion, a numerical simulation method has been developed using the Quantum Trajectory Method. Finally, the realization of quantum Ramsey interferences in a toroidal cavity developed for the realization of Quantum Non Demolition (QND) measurements is theoretically demonstrated.*

In Chapter 2, a general theoretical introduction about the one-atom maser has be done and the steady-state of the micromaser field has been analytically calculated. However, there are no analytical solutions for the time dependence of the field density matrix $\rho$, except in the particular case of trapping states at zero temperature. In order to go beyond the approximations of an analytical treatment of the time evolution of the cavity field, one has to take recourse to numerical methods. The micromaser is ideally suited for treatments by numerical simulation (Monte Carlo) methods. The random arrival time of each atom can be easily modeled, and the calculation of the field change due to the passage of each atom is straightforward as the effect of the cavity decay between the passage of two atoms can also be readily calculated [102][103]. By carrying out this procedure for a sequence of atoms during a time interval $(0, t)$, repeating it and averaging it, it is possible to reconstruct the time evolution of the cavity field $\rho(t)$ for a given $\rho(0)$, or the time dependence of the mean value of the cavity field variables [35]. Therefore there are many similarities between the methods used to analyze the micromaser features and the quantum trajectory method (QTM) used in quantum optics in the treatment

of Markovian master equation [104][105][106]. Rather than solving the master equation for a density operator itself, the method involves the construction of an ensemble of states statistically equivalent to the density operator solution. These states evolve stochastically by non-unitary operations for a certain time interval interrupted at random by discontinuous changes of state, e.g "Quantum Jumps". For example an atom entering the cavity in the upper state undergoing a transition to the lower maser state as it emits a photon, or, in the case of cavity decay as for the micromaser, the loss of a photon from the cavity to the environment.

However the correspondence between the master equation and the ensemble of trajectories is not unique as the kinds of quantum jump is not unique. If the different ensembles that can be generated, all correspond to the same density operator, they can represent the master equation. In the case each state of the ensemble is pure and remains pure through the time evolution governed by a non-linear stochastic Schrödinger equation, only $N$ components from the state vector are needed, compared to the $N^2$ components of the density operator showing an advantage for large $N$ as a large number of simulations are necessary to obtain statistically reliable averages.

Nevertheless QTM is more than a calculation tool and is connected to quantum measurement theory. The master equation describes the irreversible dynamics of a dissipative system coupled to a reservoir. In the case of the micromaser, the atoms leaving the cavity can be understood as decay products of the cavity. Therefore the detection of these atoms represents from a quantum measurement perspective the acquisition of information by the observer, and with each detection the cavity field will be projected into a new state, e.g undergoing a quantum jump, conditioned on the detection results. An explicit connection is established between a quantum trajectory and a macroscopic record of detection and a quantum trajectory analysis of the master equation can be built around the chosen detection scheme.

The essential elements of a quantum trajectory are explicitly built into the micromaser by the presence of the atomic beam. The cavity field evolution, e.g decay, is interrupted by a quantum jump due to the presence of an atom at a random time, representing one unravelling of the micromaser dynamics.

In the following section, the quantum formalism applied to the micromaser and its application for numerical simulations will be presented. The particular case of phase diffusion in the micromaser and quantum Ramsey interferences in a toroidal cavity will be discussed.

## 6.1 QTM applied to the Micromaser

The quantum trajectory formalism will be outlined here in reference to the master equation (2.57) introduced in Chapter 2. The Markovian master equation for Poissonian pumping can be written as:

$$\frac{\partial \rho}{\partial t} = \mathcal{R}(\mathcal{A} - 1 + \mathcal{L})\rho \tag{6.1}$$

with:

$$\begin{aligned}\mathcal{A}\rho = \cos(g\tau\sqrt{a^\dagger a + 1})\rho(t_0)\cos(g\tau\sqrt{a^\dagger a + 1}) + \\ a^\dagger \frac{\sin(g\tau\sqrt{a^\dagger a + 1})}{\sqrt{a^\dagger a + 1}}\rho(t_o)\frac{\sin(g\tau\sqrt{a^\dagger a + 1})}{\sqrt{a^\dagger a + 1}}a\end{aligned} \tag{6.2}$$

Equation (6.1) can be re-expressed in terms of a set of operators $C_i, i = -1, 0, 1, 2$ with:

$$C_{-1} = \sqrt{\gamma(n_{th} + 1)}a \tag{6.3}$$

which corresponds to the loss of a photon from the cavity field the the reservoir. The operator

$$C_1 = \sqrt{\mathcal{R}}a^\dagger \frac{\sin(g\tau\sqrt{a^\dagger a + 1})}{\sqrt{a^\dagger a + 1}} \tag{6.4}$$

is associated with the gain of a photon to the cavity from an atom passing through the cavity while,

$$C_0 = \sqrt{\mathcal{R}}\cos(g\tau\sqrt{a^\dagger a + 1}) \tag{6.5}$$

corresponds to an atom in the excited state passing through the cavity without giving a photon.
Finally,

$$C_2 = \sqrt{\gamma n_{th}}a^\dagger \tag{6.6}$$

is associated to the gain of a photon from the reservoir.

With equation (2.49) expressing $\mathcal{L}$ and using:

$$\mathcal{R}\rho = \frac{1}{2}(C_1^\dagger C_1 + C_0^\dagger C_0)\rho + \frac{1}{2}\rho(C_1^\dagger C_1 + C_0^\dagger C_0) \tag{6.7}$$

one can rewrite equation (6.1) in the form:

$$\frac{\partial \rho}{\partial t} = \sum_{i=-1}^{2}[C_i \rho C_i^\dagger - \frac{1}{2}(C_i^\dagger C_i \rho + \rho C_i^\dagger C_i)] \tag{6.8}$$

The terms

$$C_i \rho C_i^\dagger = J_i \rho \tag{6.9}$$

can be associated with the system undergoing discrete jumps of type $C_i$ as $\rho \to C_i \rho C_i^\dagger$ with for exemple a gain of one photon in the cavity if the jump is of type $J_1$ or a loss of one photon for a $J_{-1}$ operation. The operators $J_i$ can then be linearly combined to form a new operator $\mathcal{J}$:

$$\mathcal{J}\rho = \sum_i C_i \rho C_i^\dagger = \sum_i J_i \rho \tag{6.10}$$

Now replacing $\mathcal{L}$ by $\mathcal{L} - \mathcal{J} + \mathcal{J}$ and using the identity:

$$e^{(A+\eta B)t} = e^{At} + \sum_{n=1}^{\infty} \eta^n \int_0^t dt_n \int_0^{t_n} dt_{n-1} \cdots \int_0^{t_2} dt_1 e^{A(t-t_n)} B e^{A(t_n - t_{n-1})} B \cdots B e^{At_1} \tag{6.11}$$

the solution for the time evolution of the cavity field reads:

$$\begin{aligned} \rho(t) = \rho_c^{(0)}(t) P^{(0)}(t) + \sum_{n=1}^{\infty} \sum_{i_1} \cdots \sum_{i_n} \int_0^t dt_n \int_0^{t_n} dt_{n-1} \cdots \int_0^{t_2} dt_1 \\ \times \rho_c^{(n)}(t; i_1, t_1, \cdots, i_n, t_n) \\ \times P^{(n)}(i_1, t_1, \cdots, i_n, t_n; [0, t]) \end{aligned} \tag{6.12}$$

with:

$$\rho_c^{(0)}(t) = \frac{e^{(\mathcal{L}-\mathcal{J})t}}{Tr[e^{(\mathcal{L}-\mathcal{J})t}\rho(0)]}$$

$$P^{(0)}(t) = Tr[e^{(\mathcal{L}-\mathcal{J})t}\rho(0)] \tag{6.13}$$

and

$$\rho_c^{(n)}(t; i_1, t_1, \cdots, i_n, t_n)$$

$$= \frac{e^{(\mathcal{L}-\mathcal{J})(t-t_n)} \mathcal{J}_{i_n} e^{(\mathcal{L}-\mathcal{J})(t_n - t_{n-1})} \mathcal{J}_{i_{n-1}} \cdots \mathcal{J}_{i_1} e^{(\mathcal{L}-\mathcal{J})(t_1)\rho(0)}}{Tr[e^{(\mathcal{L}-\mathcal{J})(t-t_n)} \mathcal{J}_{i_n} e^{(\mathcal{L}-\mathcal{J})(t_n - t_{n-1})} \mathcal{J}_{i_{n-1}} \cdots \mathcal{J}_{i_1} e^{(\mathcal{L}-\mathcal{J})(t_1)\rho(0)}]} \tag{6.14}$$

$$P^{(n)}(i_1, t_1, \cdots, i_n, t_n; [0, t])$$

$$= Tr[e^{(\mathcal{L}-\mathcal{J})(t-t_n)} \mathcal{J}_{i_n} e^{(\mathcal{L}-\mathcal{J})(t_n - t_{n-1})} \mathcal{J}_{i_{n-1}} \cdots \mathcal{J}_{i_1} e^{(\mathcal{L}-\mathcal{J})(t_1)\rho(0)}]$$

$P^{(n)} = 0, 1, 2, \cdots, n$ can be interpreted as the probability that an event of the type $i_n$ occurs in the time interval $[t_n, t_n + dt_n]$, $P^{(0)}$ being the probability that no events happens in the time interval $[0, t]$, e.g no atoms passing through the cavity during this time interval and no interaction between the cavity field and the environment. $\rho^{(n)_c(t;i_1,t_{1n},t_n)}$ can be interpreted as the conditioned state of the cavity at the time $t$. The conditioning is on $n$ jumps of type $i_1, \cdots, i_n$ induced by the jump operators $J_i, i = -1, 0, 1, 2$ at the times $t_1, \ldots, t_n$, while the system evolution is governed by the non-unitary operator $e^{(\mathcal{L}-\mathcal{J})t}$ between two jumps and given that the cavity is initially prepared in the state $\rho(0)$.

The numerical implementation of the QTM is then realized by propagating the conditioned state through infinitesimal time steps, asking at the end of each step whether or not a jump has occurred and of which type it was [106]. However a more efficient procedure is particularly suited for the micromaser. The principle is to evaluate after each jump, the time of occurrence of the next jump. In other word, the conditioned state $\rho^{(n)_c(t_n;i_1,t_1\cdots i_n,t_n)}$ at the time $t_n$ will propagate under the action of the non-unitary operators $e^{(\mathcal{L}-\mathcal{J})t}$ until $t = t_{n+1}$, the time of the next jump. $t_{n+1}$ can be generated numerically by evaluating the probability that a jump of any kind occurs in the time interval $[t_{(n)}, t_{(n+1)}]$. [105] shows that the probability can be evaluated in terms of a new random variable $r$ defined by:

$$r(t) = Tr[e^{(\mathcal{L}-\mathcal{J})(t-t_n)}\rho_c^{(n)}(t; i_1, t_1 \cdots, i_n, t_n)] \tag{6.15}$$

where $r$ can be shown to be uniformly distributed on $[0, 1]$. Therefore, it is possible to simulate the time of the $(n + 1)th$ jump by choosing a random number $r_{n+1}$ from the distribution $[0, 1]$ and calculating the time $t_{n+1}$ of the next jump by the condition:

$$r_{n+1} = Tr[e^{(\mathcal{L}-\mathcal{J})(t_{n+1}-t_n)}\rho_c^{(n)}(t_n; i_1, t_1 \cdots, i_n, t_n)] \tag{6.16}$$

The remaining steps in the simulation are standards: the probability that a jump of type $J_i$ occurs is given by:

$$P_i = \frac{Tr[J_i\rho_c^{(n)}(t_n; i_1, t_1 \cdots, i_n, t_n)]}{Tr[\mathcal{J}\rho_c^{(n)}(t_n; i_1, t_1 \cdots, i_n, t_n)]} \tag{6.17}$$

and then the new conditioned state reads:

$$\rho_c^{(n+1)}(t_{n+1}; i_1, t_1 \cdots, i_{n+1}, t_{n+1}) = \frac{J_i\rho_c^{(n)}(t_n; i_1, t_1 \cdots, i_n, t_n)}{Tr[\mathcal{J}\rho_c^{(n)}(t_n; i_1, t_1 \cdots, i_n, t_n)]} \tag{6.18}$$

This state is then propagated till the next jump in an iterative way, using the procedure defined in (6.14) and (6.15) with new random number $r$ and so

until the trajectory completes the time of interest. Repeating the process with the same initial state $\rho(0)$ will generate a new trajectory. Averaging over all trajectories allows the reconstruction of the state density operator $\rho(t)$.

As previously mentioned, the operator $\mathcal{J}$ can be arbitrarly constructed from a linear combination from the different jump operators $J_i$. One possible choice would be to consider a jump of the cavity occurs only in the presence of an atom and consider the interaction of the cavity field and the environment as part of the evolution between two jumps. In this case:

$$\begin{aligned}\mathcal{J}\rho &= (J_0 + J_1)\rho \\ &= \cos(g\tau\sqrt{a^\dagger a + 1})\rho\cos(g\tau\sqrt{a^\dagger a + 1}) + \\ &\quad a^\dagger \frac{\sin(g\tau\sqrt{a^\dagger a + 1})}{\sqrt{a^\dagger a + 1}}\rho\frac{\sin(g\tau\sqrt{a^\dagger a + 1})}{\sqrt{a^\dagger a + 1}}a\end{aligned} \tag{6.19}$$

From the simulation procedure $(6.14) - (6.16)$ the time of the $(n+1)th$ jump is given by:

$$r_{n+1} = e^{-\mathcal{R}(t_{n+1} - t_n)} \tag{6.20}$$

which is the arrival time of the next atoms arriving in the cavity. This is only determined by the statistical properties of the atomic beam and not by the dynamics of the system.

The simulation algorithm provided from this approach allows the simulation of the time-dependent density operator $\rho(t)$ of the cavity field. However in this case the individual quantum trajectories will produce mixed states in general, even if the cavity is in an initial pure state. Therefore, the problem can be simplified if only pure state conditioned operators need to be considered. If:

$$\mathcal{J} = J_{-1} + J_0 + J_1 + J_2 \tag{6.21}$$

Then,

$$(\mathcal{L} - \mathcal{J})\rho = -\frac{1}{2}\gamma(n_{th} + 1)(a^\dagger a\rho + \rho a^\dagger a) - \frac{1}{2}\gamma n_{th}(a^\dagger a\rho + \rho a^\dagger a) - \mathcal{R}\rho \tag{6.22}$$

The operators $J_i$ and $(\mathcal{L} - \mathcal{J})$ have the properties of mapping pure states into pure states, leading to a quantum trajectory simulation in term of stochastically evolving pure states. In this case one can consider any change of the cavity as a jump operation as the state of the cavity remains unchanged between two jumps.

For a conditioned state $|m\rangle$ after the jump at a time $t_n$, the waiting time for the next jump can be evaluated from (6.14):

$$t_{n+1} - t_n = \frac{-\mathcal{R}^{-1} log(r_{n+1})}{1 + \mathcal{R}[(n_{th} + 1)m + n_{th}(m + 1)]} \tag{6.23}$$

while from (6.15) the probability that the next jump is of type $i$ at $t_{n+1}$ is given by:

$$p^{-1} = \frac{\mathcal{R}(n_{th}+1)m}{1+\mathcal{R}[(n_{th}+1)m+n_{th}(m+1)]} \qquad |m\rangle \to |m-1\rangle \tag{6.24}$$

$$p^{0} = \frac{\cos^2(g\sqrt{m+1}\tau)}{1+\mathcal{R}[(n_{th}+1)m+n_{th}(m+1)]} \qquad |m\rangle \to |m\rangle \tag{6.25}$$

$$p^{1} = \frac{\sin^2(g\sqrt{m+1}\tau)}{1+\mathcal{R}[(n_{th}+1)m+n_{th}(m+1)]} \qquad |m\rangle \to |m+1\rangle \tag{6.26}$$

and

$$p^{2} = \frac{\mathcal{R}n_{th}(m+1)}{1+\mathcal{R}[(n_{th}+1)m+n_{th}(m+1)]} \qquad |m\rangle \to |m+1\rangle \tag{6.27}$$

$P^0$ does not involve any change of the cavity field but has to be taken into account as it represents the case of an atom in the upper maser state passing trough the cavity without letting a photon inside. As the detection scheme is based on the discrimination of the states of the atoms emerging from the cavity, it is also important to take this operation in consideration as one wants to connect the quantum trajectory formalism with the theory of continuous measurement on an atomic beam [107].

Finally, as the cavity is initially in a thermal state at a finite temperature $T$, the cavity density operator can be represented in the photon number basis with its matrix element given by:

$$\rho_{n,n}(0) = \frac{n_{th}^n}{(1+n_{th})^{n+1}} \tag{6.28}$$

The experimental conditions can therefore easily be implemented in the simulation as one has access to all experimental free parameters (interaction time, atomic pumping rate, and cavity temperature e.g initial thermal state of the cavity).

However, given the large number of trajectories (over 100 000) required to obtain significant results for the steady-state of the micromaser, it is undoubtedly the case that using numerical simulations does not provide any advantage over a direct analytical treatment of the master equation. On the other hand the intimate connection between Quantum Trajectory Measurements and continuous measurements also enables a different perspective on the application of the method to the micromaser, for example in the context of testing ground for the quantum theory of continuous feedback [108, 109] or in the study of collective effects in the trapping state regime [110].

## 6.2 Micromaser Linewidth and the Phase Diffusion

One particular case where it is relevant to apply a quantum trajectory treatment is for the study of the micromaser spectrum and the measure of the micromaser linewidth $D$ [111].

There exist various definitions of the spectrum [112, 113]. One is governed by the decay of the expectation value of the electric field [114]:

$$\langle E(t)\rangle \sim \sum_{n=0}^{\infty}(n+1)^{1/2}\rho_{n,n+1}(t) \tag{6.29}$$

Hence the micromaser spectrum study differs from the experiment on the photon statistics as it involves the off-diagonal elements of the cavity density matrix $\rho_{n,n+1}$ rather than the diagonal elements used for the study of the photon statistics and it requires their full time dependance rather than their steady-states values.

The study of the micromaser spectrum requires therefore a time dependent measurement of the off diagonal elements of the radiation density matrix. Also it is shown that looking at the micromaser spectrum is analog to study the micromaser linewidth. The measurement of the decay of the off-diagonal elements of the field density matrix will then provide a direct measurement of the micromaser linewidth. In 1991 Scully and co-workers demonstrated analytically the relation between expectation value of the electrical field and the linewidth $D$ of the micromaser [111]:

$$\langle E(t)\rangle \sim e^{-(D/2)t}\sum_{n=0}^{\infty}(n+1)^{1/2}\rho_{n,n+1}(0) \tag{6.30}$$

where $D$ reads:

$$D = 4N_{ex}\sin^2\left(\frac{g\tau}{4\sqrt{\langle n\rangle}}\right) + \frac{\gamma(2n_{th}+1)}{4\langle n\rangle} \tag{6.31}$$

In the limit of small interaction time or large mean photon number one recovers the familiar Schawlow-Townes linewidth by expanding the sin function:

$$D = \frac{\alpha + \gamma(2n_{th}+1)}{4\langle n\rangle} \tag{6.32}$$

with $\alpha = \gamma(N_{ex}^{1/2}g\tau)^2 = \gamma\theta^2$ and $\theta$ is defined as the pump parameter.

$D$ presents also two novel features quite distinct from the familiar Schawlow-Twones linewidth for a laser. First of all in the region of trapping states, sharp

resonances are present. For large values of $\theta$ the linewidth $D$ can even oscillate. Figure 6.1 [111] shows the detailed behavior of the phase diffusion constant $D$ (solid line), as a function of the pump parameter $\theta$ for $N_{ex} = 50$ atoms and $n_{th} = 10^{-4}$. In order to show the strong dependence of $D$ to the mean photon number $\langle n \rangle$ the maser pump curve with a normalized photon number $n/10$ is also plotted.

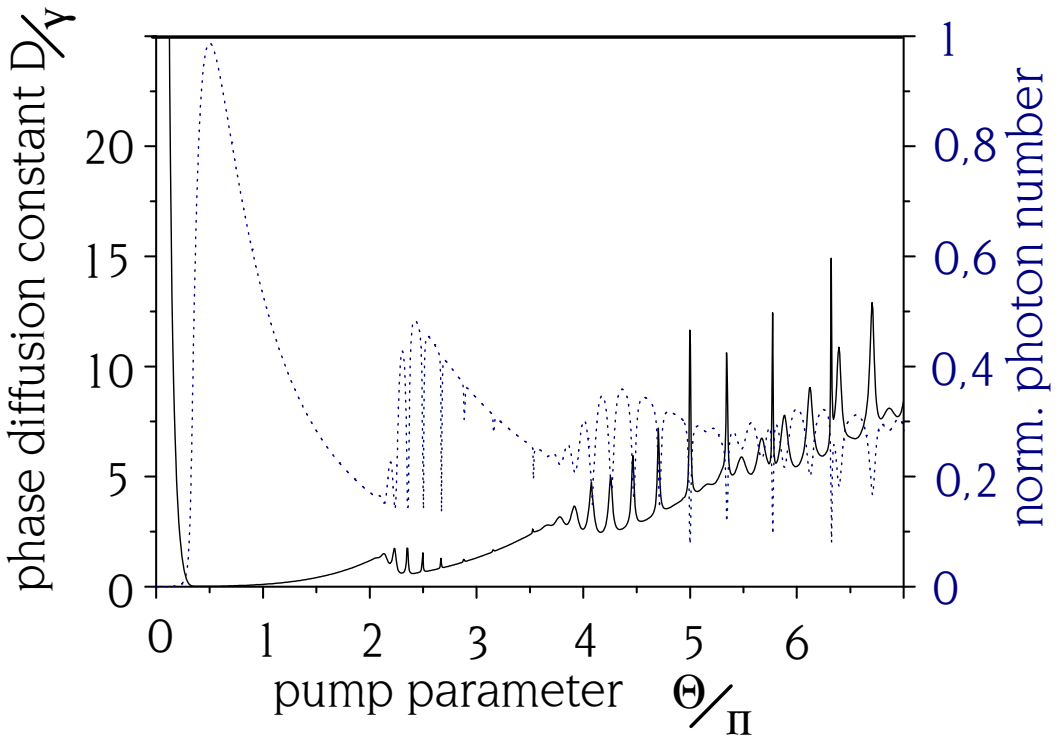


Figure 6.1: *Phase Diffusion Constant D*

However in order to measure the phase diffusion factor $D$ one faces two issues due to the properties of the micromaser. The phase diffusion acts only on the off-diagonal elements of the field density matrix. First, due to the incoherent atomic pumping, as only upper state atoms are injected into the cavity, no off-diagonal terms are produced. Secondly, as it is shown in Chapter 3, the measurement of the cavity field is done via the state selective detection of the outgoing atoms. However, if this method is relevant to measure the photon statistics, as the atomic and photon statistics are coherently linked to the Jaynes-Cummings interaction, no information about the phase of the field can be extracted from this measurement.

In order to access to a phase measurement of the maser field, Scully and co-worker proposed to realized a Ramsey type experiment [111]. Based on a Ramsey type interferometer [41] with two additional low Q microwave cavities $C_1$ and $C_2$, the experiment goes as follows:
In a first step a weak microwave field in $C_1$ drives the atoms in a coherent superposition $|e\rangle$ and $|g\rangle$. However, due to the very small probabilities of the $|g\rangle$ states, no changes on the photon statistics are done compare to an incoherent pumping. However, the atoms, so prepared, produce a phase state of the maser field with non-zero off-diagonals elements $\rho_{n,n+1}$.
In the second step, the field in $C_1$ is switched off and the maser field begins to phase diffuse under the incoherent atomic pumping. As previously mentioned the atoms exit the cavity in a superposition of $|e\rangle$ and $|g\rangle$. Interacting with a second classical field with a well-defined phase in $C_2$ allows to encode the phase information about the maser cavity onto the atomic statistics. The outgoing result is that the atomic probability to detect excited atoms $P_e$ and the off-diagonal elements $\rho_{n,m}$ have the same diffusion constant $D$:

$$P_e = \frac{1}{2} + e^{-\frac{1}{2}Dt} \sum_n \cos(\alpha - \beta) \cos(g\tau\sqrt{n+e}) \times \sin(g\tau\sqrt{n+1})\rho_{n,n+1}(0) \quad (6.33)$$

where $\alpha$ and $\beta$ are respectively the phase of $C_2$ and the initial phase of the micromaser.

However, the possible presence of electrical stray fields at the entrance holes of the cavity [74] could have a negative effect with a random change of the atomic phase state and therefore doesn't make micromaser experiment suitable for the realization of the Scully proposal. Also, the implementation of two extras cavities will enhance the time of flight of the atoms, being comparable to their lifetime, introducing decoherences into the system. An other method proposed by Casagrande et al.[115] using a quantum-state reconstruction proposed by Bodendorf et al.[40] is more suitable and also a very good candidate for a treatment using quantum trajectories.

Using a coherent displacement in phase space by injecting a coherent field into the micromaser cavity it is possible to encode the phase information onto the photon statistics. Probing the displaced field by an excited atoms allows a full reconstruction of non-classical cavity field states, providing informations of their decoherence [116].

Starting from the cavity state $\rho$ one wants to reconstruct, the application of a displacement in phase space under the injection of a coherent state $|\alpha\rangle$ reads:

$$D(\alpha) = e^{(\alpha a - \alpha^* a^\dagger)} \quad (6.34)$$

And the probability to detect an atom in the excited state is then [86]:

$$p_e(\alpha) = \sum_n \langle n|D(\alpha)\rho D^\dagger(\alpha)|n\rangle \cos^2(g\tau\sqrt{n+1}) \tag{6.35}$$

Figure 6.2 shows how the displacement operator acts on the photon statistics, e.g $\rho_{n,n}$.

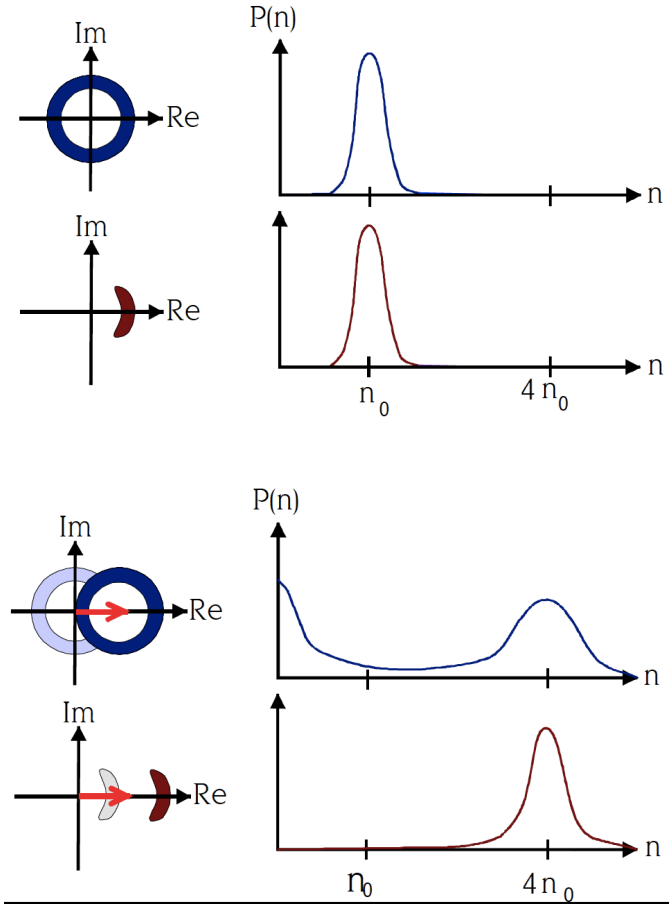


Figure 6.2: *Field Displacement in Phase Space and Atomic Statistics: the state selective detection of the Rydberg atoms gives only information over the photon number statistics. As shown in the upper graph, two field states with the same photon statistics but with different phase will lead to the same atomic statistics. However, after a field displacement operated in the phase space, the phase information is written on the photon statistics, and two displaced field with different phase will then lead to two different atomic statistics.*

The measurement of the phase diffusion is then done as follow:

- At $t = 0$ a coherent state $|\alpha\rangle$ is injected in the cavity.

- The phase of the maser field diffuses under the incoherent atomic pumping to the micromaser steady-state $\rho^{ss}$.

- The interaction time is chosen to fulfill the trapping states condition with $n_{trap} = \alpha^2$ in order to exhibit the larger dependence.

- Operate at a time $t$ a displacement of the phase diffused field and probe it with an atom.

From the above steps it is straight forward to see the link with a quantum trajectories treatment of the phase diffusion problem and its numerical implementation:
Starting from the initial state $\rho(0) = |\alpha\rangle\langle\alpha|$ one apply the algorithm describes by the equation 6.23 - 6.27 for the desired evolution time $t$. Then at t, one proceed to the displacement operation to extract the expected value for the atomic detection:

$$P_e(\alpha, t) = e^{-\frac{1}{2}Dt}\chi(\alpha) + P_e^{ss}(\alpha) \tag{6.36}$$

with:

$$\chi(\alpha) = 2\sum_n \sum_i \rho_{i,i+1}(0)\langle n|D(-\alpha)|i\rangle\langle i+1|D(\alpha)|n\rangle \times \cos^2(g\tau\sqrt{n+1}) \tag{6.37}$$

Repeating the algorithm for many $t$ gives a full dynamic of the phase diffusion process. Figure 6.5 shows the numerical results using a quantum trajectory treatment for the phase diffusion dynamics in the micromaser. The Husini distribution function $Q(\alpha)$ is calculated and represented for different time evolution. Starting from a well defined phase state for a coherent field at $t = 0$, the phase of the micromaser field start to diffuse through an intermediate states, ending to a complete phase-loss information for a Fock state. The parameter are $|\alpha\rangle = 2$, $N_{ex} = 50$, $\tau = \frac{\pi}{g\sqrt{5}}$ and $\gamma = 2.15$ Hz.

## 6.3 Ramsey Interferences in a Toroidal Cavity

In this section, the realization of Ramsey interferometry experiment between a single atom and quantized fields is discussed. The method of using spatially separated fields proposed by Ramsey [117] has found many application

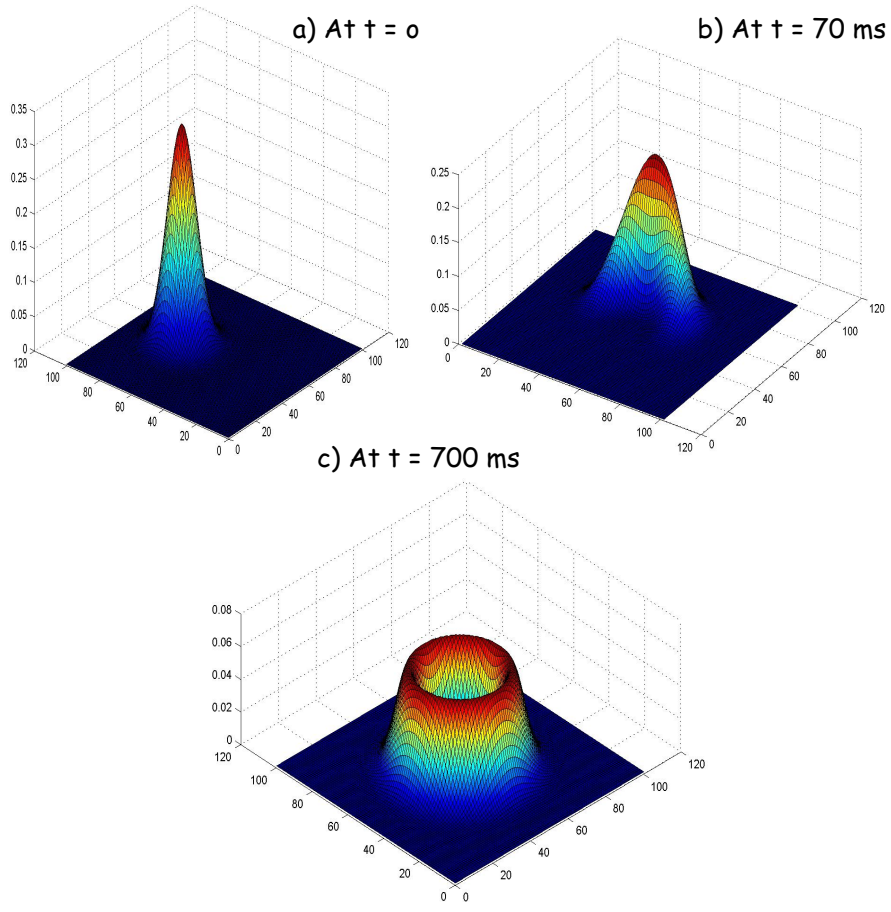


Figure 6.3: *Time evolution of the Q-representation of the micromaser field. Starting from a coherent state with a well defined phase, under the action of the atoms pumping the cavity into a fock state, the phase starts to diffuse ending in the undefined phase state of a Fock state.*

in particular for high resolution work [118]. The existence of fringes in the Ramsey technique has been interpreted as due to quantum interferences in the transition amplitudes and is therefore a way of doing atomic interferometry. Originally proposed as a technique in the microwave domain, it was then extended to the optical domain [119]. The field used in each Ramsey zone is coherent with large amplitude which is not changed as it interacts with an atom.

The realization of Cavity QED experiment at the quantum level between a single atom and a quantized field of a high Q cavity offers now the possibility to study the Ramsey interferometer with quantized field.

A two-level atom interacts for a well defined time $\tau$ with each cavity separate by a free evolution during the time of flight between the two cavities. As for the micromaser the atoms is then detected after the interaction with the second cavity. The two cavities have the same frequency $\omega_F$, as the two atomic levels $|e\rangle$ and $|g\rangle$ have a frequency separation $\omega_A$. Using the Jaynes-Cummings interaction outlined in Chapter 2, the interaction between the atom and the cavity reads:

$$H_{AF} = \hbar g_i (a^\dagger \sigma e^{i\Delta t} + a\sigma^\dagger e^{-i(\Delta)t}) \tag{6.38}$$

with the detuning $\Delta = \omega_F - \omega_A$, and $g_i$ are the atom-field coupling constant for the $ith$ cavity. The cavity fields are initially in an arbitrary state $\sum_{n,m} \mathcal{P}_{n,m}|n,m\rangle$ and the atom is prepared in the excited state $|e\rangle$.

After the first interaction the wave function of the Atom-Field system reads:

$$\begin{aligned}\Psi_{A-F}(\tau) =& e^{-i\Delta\tau} \sum_{n,m} \mathcal{P}_{n,m}[\cos(\lambda_{n,1}\tau) + \frac{i\Delta}{\lambda_{n,1}} \sin(\lambda_{n,1}\tau)]|e,n,m\rangle \\ &- ie^{i\Delta\tau} \sum_{n,m} \mathcal{P}_{n-1,m} \frac{g_1\sqrt{n+1}}{\lambda_{n,1}} \sin(\lambda_{n,1}\tau)|g,n,m\rangle \end{aligned} \tag{6.39}$$

with $\lambda_{n,1} = \sqrt{(\frac{\Delta}{2})^2 + g_1^2(n+1)}$ the generalized Rabi frequency for the first cavity.

The system undergoes in a free evolution for a time T as the atoms fly from one cavity to the other one. During this time the Hamiltonian of the system reads:

$$H_{free} = \hbar\omega_F a^\dagger a + \frac{1}{2}\hbar\omega_A \sigma_z \tag{6.40}$$

The action of $\sigma_z$ on the atomic component is:

$$\sigma_z|e\rangle = |e\rangle; \sigma_z|g\rangle = -|g\rangle \tag{6.41}$$

so that before entering again in the cavity the new state of the system is :
$\Psi_{A-F}(\tau + T) = e^{-i\frac{H_{free}}{\hbar}T}\Psi_{A-F}(\tau)$

$$\begin{aligned}\Psi_{A-F}(\tau + T) =& e^{-i\Delta\tau} \sum_{n,m} e^{-i\varphi_e T}\mathcal{P}_{n,m}[\cos(\lambda_{n,1}\tau) + \frac{i\Delta}{\lambda_{n,1}} \sin(\lambda_{n,1}\tau)]|e,n,m\rangle \\ &- ie^{i\Delta\tau} \sum_{n,m} e^{-i\varphi_g T}\mathcal{P}_{n-1,m} \frac{g_1\sqrt{n+1}}{\lambda_{n,1}} \sin(\lambda_{n,1}\tau)|g,n,m\rangle \end{aligned} \tag{6.42}$$

with $\varphi_e = \omega_F n + \frac{\omega_A}{2}$ and $\varphi_g = \omega_F(n+1) - \frac{\omega_A}{2}$. Before to go further, one can remark that:

$$\varphi_g - \varphi_e = \Delta \tag{6.43}$$

Introducing the following function:
$C_i(\tau) = \cos(\lambda_{n,1}\tau) + \frac{i\Delta}{\lambda_{n,1}}\sin(\lambda_{n,1}\tau)$
and $S_i(\tau) = -i\frac{g_1\sqrt{n+1}}{\lambda_{n,1}}\sin(\lambda_{n,1}\tau)$,
which describes the dynamics of a two-level atom interacting with a single mode of a radiation field, the state of the system after the interaction in the second cavity reads:

$$\begin{aligned}\Psi_{A-F}(2\tau+T) = &\sum_{n,m}\mathcal{P}_{n,m}C_n(\tau)C_m(\tau)e^{-i\Delta\tau-i\varphi_eT}\\ &+\mathcal{P}_{n-1,m+1}S_{n+1}(\tau)S_m(\tau)e^{-i\Delta(\tau+T)-i\varphi_gT}|e,n,m\rangle\\ &\sum_{n,m}\mathcal{P}_{n-1,m}S^*_{n-1}(\tau)C^*_{m-1}(\tau)e^{-i\Delta\tau-i\varphi_eT}\\ &+\mathcal{P}_{n,m-1}C_n(\tau)S^*_{m-1}(\tau)e^{-i\Delta(\tau+T)-i\varphi_gT}|g,n,m\rangle \qquad (6.44)\end{aligned}$$

The structure of the final state clearly shows that there are two paths for the system to involve to its final state like the two arms of an interferometer. In the case of an atom entering in the excited state $|e\rangle$ and emerging from the second cavity in the ground state $|g\rangle$, the two path would be, i) no photon emission in the first cavity but in the second only:
$|e,n,m\rangle \rightarrow |e,n,m\rangle \rightarrow |g,n,m-1\rangle$
or ii) emission of a photon in the first cavity and no-absorption in the second cavity:
$|e,n,m\rangle \rightarrow |g,n-1,m\rangle \rightarrow |e,n-1,m\rangle$
Tracing over the field gives the detection probability for an atom to be detected in the ground state:

$$P_g = \sum_{n,m}|\mathcal{P}_{n-1,m}S^*_{n-1}(\tau)C^*_{m-1}(\tau) + \mathcal{P}_{n,m-1}C_n(\tau)S^*_{m-1}(\tau)e^{-i\Delta T}|^2 \qquad (6.45)$$

One can then show that if the fields in cavity 1 and 2 are coherent, with mean photon number of $\bar{n}$ and $\bar{m}$ , one recovers the classical case whith:

$$P_g = |S^*_{\bar{n}}(\tau)C^*_{\bar{m}}(\tau) + C_{\bar{n}}(\tau)S^*_{\bar{m}}(\tau)e^{-i\Delta T}|^2 \qquad (6.46)$$

If Ramsey interferences occur in the classical case when the two fields are uncorrelated and of different strength, in the quantum case, however, the interference between the two path depends on the photon statistics of each cavity field. In particular, in the case of two Fock states $|N\rangle$ and $|M\rangle$ in each cavity, the two paths becomes independent as the two different field statistics lead to two different realization probabilities. Therefore in the case of quantized field, the condition on the quantum statistics of the two independent Ramsey zone imply that the two cavities are either in a well-defined phase state, e.g

coherent states, or the two cavities are entangled. An experiment with two microwave cavities interacting with a single Rydberg atom has been realized [120]. In the case of two coherent fields, Ramsey interferences were observed. However, when the first cavity was not in a well-defined phase state, the interferences vanished. Also, in the case of very small coherent states, the quantum treatment shows fringes with a smaller contrast than for the classical case [121].

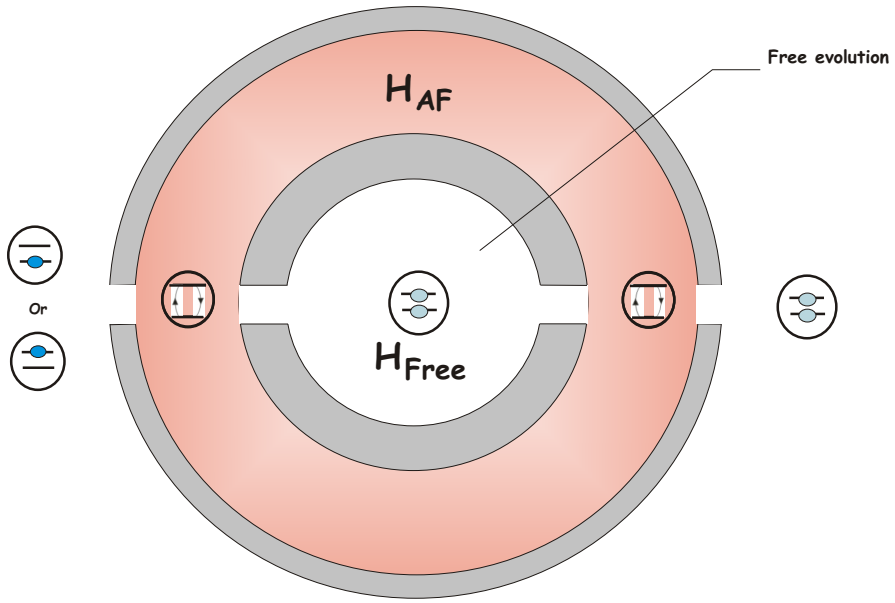


Figure 6.4: *Torroidal cavity: the high Q cavity allows the realization of a Ramsey interferometer with quantized field. The atom interact with the cavity field a first time before leaving for the free-evolution region and reentering it. Due to the long coherence time of the cavity and the long lifetime of the Rydberg atoms, the atom-field system remains coupled during the all process, leading to the realization of a quantum Ramsey interferometer.*

In the Garching experiment, Ramsey interferences with quantized field are investigated in the quantum beat experiment. In 1994 Braginski and Khalili proposed the used of a toroidal microwave cavity for a quantum non-demolition measurement (QND) [122, 123]. Figure 6.4 shows the design of the toroidal cavity. The main particularity of this cavity is that the interaction takes place twice with a free evolution of the system in-between. Due to the high Q of

the cavity, one assume that the field does not decay during the free evolution and is therefore a suitable candidate to study Ramsey interferences with a quantized field.

Assuming the cavity is in a Fock state $|n\rangle$, from (6.44) the final state of the system reads:

$$\begin{aligned}\Psi_{A-F}(2\tau+T) \quad &= e^{-i2\Delta\tau}\{e^{-i\varphi_e T}(\cos(\lambda_n\tau)+i\frac{\Delta}{2\lambda_n}sin(\lambda_n\tau))^2 \\ &\quad e^{-i\varphi_g T}\frac{g^2(n+1)}{\lambda_n^2}\sin^2(\lambda_n\tau)\}|e,n\rangle \\ &\quad -ie^{i2\Delta\tau}\frac{g\sqrt{n+1}}{\lambda_n}\sin(\lambda_n\tau)\{e^{-i\varphi_g T}(\cos(\lambda_n\tau)+i\frac{\Delta}{2\lambda_n}\sin(\lambda_n\tau)) \\ &\quad +e^{-i\varphi_e T}(\cos(\lambda_n\tau)-i\frac{\Delta}{2\lambda_n}sin(\lambda_n\tau))\}|g,n+1\rangle\end{aligned} \tag{6.47}$$

In an other form:

$$\Psi_{A-F}(2\tau+T) = A_n(\tau,T)|e,n\rangle + B_n(\tau,T)|g,n+1\rangle \tag{6.48}$$

with:

$$A_n(\tau,T) = e^{-i2\Delta T}C_n^2(\tau)e^{-i\phi_e T} + S_n^2(\tau)e^{-i\phi_g T}$$

$$B_n(\tau,T) = S_n^*(\tau)C_n^*(\tau)e^{-i\Delta\tau-i\varphi_e T} + C_n(\tau)S_n^*(\tau)e^{-i\Delta(\tau+T)-i\varphi_g T}$$

and the probability for an atom to be detected in the ground state is:

$$\begin{aligned}P_g \quad = \quad &\frac{g^2(n+1)}{\lambda_n^2}\sin^2(\lambda_n\tau)\{2cos^2(\lambda_n\tau)[1+\cos(\Delta T)] \\ &+\frac{\Delta^2}{2\lambda_n^2}\sin^2(\lambda_n\tau)[1-\cos(\Delta T)] \\ &\frac{2\Delta}{\lambda_n}cos(\lambda_n\tau)\sin(\lambda_n\tau)\sin(\Delta T)\}\end{aligned} \tag{6.49}$$

From this, one can make some remark:
- first of all we see that in resonance, the toroidal cavity leads exactly to the realization of the Jaynes-Cummings interaction in the micromaser, with an interaction time of $2\tau$:

$$P_g = \sin^2(2g\sqrt{n+1}\tau) \tag{6.50}$$

- an other interesting feature is that when $\Delta T = 2\pi$ we recover also the micromaser case for an interaction time of $2\tau$:

$$P_g = \frac{g^2(n+1)}{\lambda_n^2}\sin^2(2\lambda_n\tau) \tag{6.51}$$

This feature is also in accord with the Ramsey interference with classical field.

The implementation of the QTM for the torroidal cavity is then straight forward. From equation (6.48), the two jumps operator $C_1$ and $C_0$ can be rewritten as:

$$C_1 = \frac{\sqrt{\mathcal{R}}a^\dagger}{\sqrt{a^\dagger a + 1}} B_n(\tau, T) \tag{6.52}$$

and

$$C_0 = \sqrt{\mathcal{R}} A_n(\tau, T) \tag{6.53}$$

The numerical simulation is then realized as outlined in the section 6.1. Figure 6.5 shows the simulation for an initial thermal state with $< n_{th} >= 1.5$, $\mathcal{R} = 100$, and $\tau = T/2 = 66$ $\mu$s.

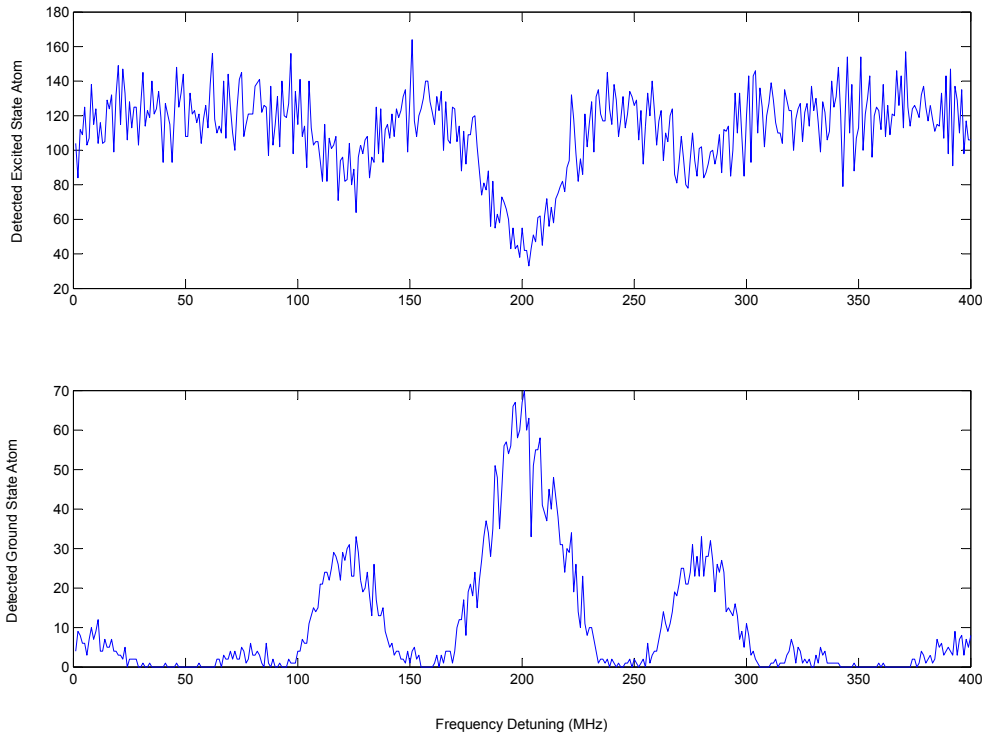


Figure 6.5: *Quantum Ramsey Interferences in a torroidal cavity*

# Outlook

In this thesis, the experimental results, where the ground state of a two-level atomic system interacts with a single mode of a high Q cavity, are presented. A new laser system to promote $^{85}Rb$ atoms into the Rydberg maser ground state $61D_{5/2}$ is developed and major improvements on the cryogenic system are achieved.

With a better control of the still temperature in the dilution cryostat and the addition of extra heat shielding around the experimental environment, the end-temperature is improved by a factor of two at $\sim 150$ mK. Moreover, a continuous working temperature from 150 mK to 1.3 K is possible, opening the path for the observation of quantum stochastic resonances in the micromaser.

The development of a new laser setup using a two-step diode laser system opened the possibility of exciting maser ground states that have never be done in this setup until now. We have also shown that purely optical spectroscopy of $Rb$ Rydberg states is possible in a room-temperature gas cell in three different excitation schemes using the quantum amplification of the electron shelving. The excitation of Rydberg states is monitored by observing the absorption of the laser driving the strongest transition. The spectroscopy method developed in this thesis can be used to detect Rydberg states with high frequency resolution and can be therefore the basis for convenient stabilization setups for a wide range of experiments. Especially, ultracold Rydberg gases are a promising candidate for realizing controlled quantum gates in atomic ensembles. Improvements in excitation and detection techniques and especially methods to stabilize laser to specific Rydberg transitions are therefore important in many experiments. Finally, the Rydberg transitions in a gas cell are highly immune to a linear and quadratic DC Stark shift. If magnetic fields are shielded by a $\mu$-metal cover, the Rydberg lines in a cell are as stable as low-lying $Rb$ levels. The closely spaced Rydberg levels therefore form a dense comb of atomic lines which offers interesting possibilities for frequency metrology and coherent control applications.

Finally, experiments with ground states atoms have been performed for the first time in the one-atom-maser. Measurements of the magnetic field compensation have achieved a higher contrast and Stark effect experiments

with high lying D state have been performed. The frequency shift of the $61D_{5/2}$ level in presence of small DC electrical field has been measured with a time of flight experiment leading to an evaluation of the fourth-order Stark effect for the 61D state in $^{85}Rb$.

The interaction between the maser ground state and the cavity field has been investigated for both a low atomic injection rate and a high atomic pumping leading to the measurement of the first maserlines in this configuration. The first observation of Rabi oscillations, with a high contrast, where ground state atoms interact with the quantized thermal field of the cavity, gives important informations about the actual field temperature.

Sending either excited state atoms or ground state atoms inside the cavity opens the possibility for a wide range of new experiments. Among them, the generation of more robust trapping states is possible by mixing excited and ground states atoms in the atomic injection. Also pump-probe experiments could be realized. Sending a sequence of excited atoms prepares the cavity in a well defined quantum state. The generated field state can then be probed with ground state atoms. At low injection rate with less than one ground state atom per cavity decay time, the realization of Rabi oscillations with high number Fock-state is possible. At higher injection rate, the quantum field generated in the cavity can be used for atom-atom entanglement.

# Bibliography


[1] A. Einstein, Phys. Zeitschr., **18**, 121 (1917)

[2] V. Weisskopf and F. Wigner, Z. Phys., **63** 54 (1930)

[3] W.E. Lamb Jr. and R.C. Retherford, Phys. Rev., **72**, 241 (1947)

[4] H.A. Bethe, Phys. Rev., **72**, 339 (1947)

[5] R. Pohl et al., The Muonic Hydrogen Lamb-Shift Experiment, Proceedings of the EXA05, eds. A. Hirtl, J. Marton, E. Widmann and J. Zmeskal, Austrian Academy of Sciences Press, Vienna, p. 285 (2005)

[6] E. T. Jaynes and F. W. Cummings, IEEE J. Quant: Elec **51** 89 (1963)

[7] E.M Purcell, Phys. Rev., **69**, 681 (1946)

[8] H.B.G Casimir and D. Polder, Phys. Rev., **73**, 360 (1948)

[9] G. Rempe et al., Coherences and Quantum Optics VIII, Kluwer Academic / Plenum Publishers, New York, p. 241(2003)

[10] J. Clarke and F.K. Wilhem, Nature, **453**, 1031 (2008)

[11] G. Burkard et al., Phys. Rev. Lett., **83**, 4204 (1999)

[12] J.A Gallas, G. Leuchs, H. Walther and H. Finger(1985), Advances in Atomic and Molecular Physics, Vol.20, Academic Press, New York, p.413

[13] S. Haroche and J.M Raymond, (1985), Advances in Atomic and Molecular Physics, Vol.20, Academic Press, New York, p.350

[14] P. Filipowicz, J. Javanainen and P. Meystre, Phys. Rev. A, **34**, 3077 (1986)

[15] S.Brattke, B.T.H. Varcoe and H. Walther, Phys. Rev. Lett., **86**, 3534 (2001)

[16] O.Benson, G. Raithel and H. Walther, Phys. Rev. Lett., **72**, 3506 (1994)

[17] J. Ye, H.J. Kimble and H. Katori, Science, **320**, 1734 (2008)

[18] R. Blatt and D. Wineland, Nature, **453**, 1016 (2008)

[19] H. Dehmelt, IEEE Trans. Instrum. Meas., **31**, 83 (1982)

[20] P. Thoumany, T.W. Hänsch, G. Stania, L. Urbonas and Th. Becker, Opt. Lett., **34**, 1621 (2009)

[21] P. Thoumany, T. Germann, T.W. Hänsch, G. Stania, L. Urbonas and Th. Becker, J. of Mod. Opt., **56**, 2055 (2009)

[22] G.Feher et al., Phys. Rev., **109**, 221 (1958)

[23] K.H. Drexhage, H. Kuhn and F.D. Schäfer, Ber. Bunsen Ges. Phys, **72**, 329(1968)

[24] D. Meschede, H. Walther and G. Müller, Phys. Rev. Lett., **54**, 551 (1985)

[25] J.C. Slater, Microwave Electronics (Princeton, N.J.: Van Nostrand, 1950)

[26] B-G. Englert, Elements of Micromaser Physics, 1994

[27] F. Bloch and A. Siegert, Phys. Rev., **57**, 522 (1940)

[28] G. Rempe , H. Walther and N. Klein, Phys. Rev. Lett., **58**, 353 (1987)

[29] B.T.H Varcoe, S. Brattke, M. Weidinger, H. Walther, Nature, **403**, 743 (2000)

[30] L.Urbonas, Experiments with the One-Atom-Maser, Dissertation, Ludwig-Maximilians-Universität, München (2009)

[31] P. Lougovski et al., Phys. Rev. Lett., **78**, 2547 (2003)

[32] D. Suter, The Physics of Laser-Atom Interactions, Cambrige University Press, (1997)

[33] L.A. Luigiato, M.O. Scully and H. Walther, Phys. Rev. A, **36**, 740 (1987)

[34] H.J Carmichael, Statistical Methods in Quantum Optics 1, Springer (1999)

[35] G. Rempe and H. Walther, Phys. Rev. A, **42**, 1650 (1990)
G.Rempe, F. Schmidt-Kaler and H. Walter, Phys. Rev. Lett., **64**, 2783 (1990)

[36] J.P. Gordon, H.J. Zeiger and C.H. Townes, Phys. Rev., **95**, 282 (1954)
J.P. Gordon, H.J. Zeiger and C.H. Townes, Phys. Rev., **99**, 1264 (1955)

[37] C. Kittel, Introduction to Solid State Physics, J. Wiley and Sons, New York, 7th Edition (1996)

[38] G. Babst, Aufbau und Test eines Mikromaser mit Supraleitenden Resonator im Temperaturbereich von $0.5K$, Dissertation,Ludwig-Maximilians-Universität, München (1989)

[39] T. Müller-Seidlitz, Untersuchungen am Ein-Atom-Maser, Dissertation, Ludwig-Maximilians-Universität, München (1992)

[40] C.T. Bodendorf et al., Phys. Rev. A, **57**, 1371 (1998)
M.S. Kim et al., Phys. Rev. A, **58**, R65 (1998)

[41] N.F. Ramsey, Molecular Beams, Clarendon Oxford (1956)

[42] G. Marchi, Construction of an Apparatus for the Measurement of the Phase Diffusion in the Micromaser, Dissertation, Universita Degli Studi di Milano (2003)

[43] J. Rydberg, Phil. Mag. $5^{th}$ series, **29**, 331, (1890)

[44] A. Dalgarno, Rydberg Atoms in Astrophysics, in Rydberg States of Atoms and Molecules, edited by R.F. Stebbings and F.B. Dunning, Cambridge University Press, (1983)

[45] P. Koch, Rydberg studies using fast beams, in Rydberg States of Atoms and Molecules, edited by R.F. Stebbings and F.B. Dunning, Cambridge University Press, (1983)

[46] T. Cubel, et al., Phys. Rev. A, **72**, 023405 (2005)

[47] M. Seaton, Quantum defect theory, Rep. Prog. Phys., **46**, 167, (1983)

[48] B. Sanguinetti et al. , J. Phys. B, **42**, 165004 (2009)

[49] T.F. Gallagher, Rydberg Atoms, Cambridge University Press, (1994)

[50] L.G. D'yachkov and P.M. Pankratov, J. Phys. B, **24**, 2267 (1991)

[51] B. Oumarou, et al., Phys. Rev. A, **37**, 1885 (1988)

[52] A.R. Edmonds, et al., J. Phys. B, **12**, 2781 (1979)

[53] W. Lange, Kohärent angeregte Rydberg-Atome in einem resonator-modifizierten Vacuumfeld, Dissertation, Ludwig-Maximilians-Universität, München (1994)

[54] I.I. Beterov et al., Phys. Rev. A, **79**, 052504 (2009)

[55] A.L. de Oliveira et al., Phys. Rev. A, **65**, 031401(R) (2002)

[56] F. Gounand, J. Phys. (Paris), **40**, 457 (1979)

[57] C.E. Theodosiou, Phys. Rev. A, **30**, 2881 (1984)

[58] M.L. Zimmerman, Phys. Rev. A, **20**, 2251 (1979)

[59] D.H. Tuan, S. Liberman and J. Pinard, Opt. Com., **18**, 533 (1976)

[60] D. Meschede, Strahlungwechselwirkung von Rydbergatomen Realisierung eines Ein-Atom-Maser, Dissertation, Ludwig-Maximilians-Universität, München (1984)

[61] J.D. Jackson, Classical Electrodynamics, J. Wiley Verlag, third edition collection (1999)

[62] W. Buckel, Superconductivity - Fundamentals and Applications, J. Wiley Verlag, second edition (2007)

[63] A.N. Luiten (editor), Frequency Measurement and Control, vol. 79 of Topics in Applied Physics, Springer (2001)

[64] G. Müller, Supraleitende Niobresonatoren im Millimeterwellenbereich, Dissertation, Bergishe Universität - Gesamthochschule Wuppertal (1983)

[65] M.A. Allen, et al. , Superconducting Niobium Cavity Measurements at SLAC, IEEE Transactions on Nuclear Science, **18 (3)**, 168 (1971)

[66] N. Klein, Supraleitende Mikrowellenresonatoren für Anwendungen in physikalischen Grundlagenexperimenten, Externer Bericht, WUB-DIS 89-3, Bergishe Universität - Gesamthochschule Wuppertal (1989)

[67] R.P. Heerlein, Entwicklung von neuartigen Mikrowellenresonatoren für den Ein-Atom-Maser, Diplomarbeit, Ludwig-Maximilians-Universität, München (1998)

[68] T.R. Roberts and S.G. Sydoriak, Phys. Rev., **98**, 1672 (1955)

[69] G. Batey, V. Mikheev, J. Low Temp. Phys., **113**, 933 (1998)

[70] H. London, Proc. 2nd Int.Conf. on Low Temp. Phys. (Oxford Univ. Press, London 1951), 157

[71] D.J. Cousins et al. , J. Low Temp. Phys., **114**, 547 (1999)

[72] A. Buchleitner and R. Mantega, Phys. Rev. Lett., **80**, 3932 (1998)

[73] J. Bernu et al. , Phys. Rev. Lett., **101**, 180402 (2008)

[74] G. Raithel, Habilitation, Ludwig-Maximilians-Universität, München , (1995)

[75] J.M. Pierce, Methods of Experimental Physics, vol. 11, Academic Press, New York, p. 541 (1973)

[76] H. Padamsee, K. Shepard and R. Sundelin, Physics and Accelerator Applications of RF Superconductivity, Annu. Rev. Nucl. Part. Sci., **43**, 635 (1993)

[77] W. Hanle, Über magnetische Beeinflussung der Polarisation der Resonanzfluoreszenz, Zeitschrift für Physik, **30**, 93 (1924)

[78] C.T. Bodendorf, Untersuchungen am Ein-Atom-Maser mit externer Einkopplung, Dissertation, Ludwig-Maximilians-Universität, München (2000)

[79] S.Brattke, Untersuchung von Photonenzahlzuständen mit dem Ein-Atom-Maser, Dissertation, Ludwig-Maximilians-Universität, München (2001)

[80] T. Germann, Experimente für den Ein-Atom-Maser mit Hilfe eines 3-stufigen Diodenlaser-Systems, Diplomarbeit, Ludwig-Maximilians-Universität, München (2008)

[81] R.T. Hawkins et al., Phys. Rev. A, **15**, 967 (1977)

[82] T.F. Gallagher et al., Phys. Rev. A, **15**, 1937 (1977)

[83] T.F Gallagher and W.E. Cooke, Phys. Rev. A, **18**, 2510 (1978)

[84] P. Kulina and R-H Rinkleff, J. Phys. B: At. Mol. Phys., **18**, 245 (1984)

[85] U. Fano and J.W. Cooper, Rev. Mod. Phys, **40**, 441 (1965)

[86] G. Marchi, Construction of an Experimental Apparatus for the Measurement of the Phase Diffusion in the Micromaser, Tesi di Dottorato, Università degli Studi di Milano

[87] T. Meunier et al., Phys. Rev. Lett., **94**, 010401 (2005)
M. Brune et al., Phys. Rev. Lett., **76**, 1800 (1996)

[88] M. Saffman, T.G. Walker and K. Mølmer, Reviews of Modern Physics, **82**, 2313 (2010)

[89] D. Jaschke et al., Phys. Rev. Lett., **85**, 2208 (2000)

[90] G. M. Lankhuijzen and L. D. Noordam, Adv. At., Mol., Opt. Phys., **38**, 121 (1998)

[91] D.J. Bradley et al., J. Phys. B, **6**, 1594 (1973)

[92] J.R. Rubbmark et al., J. Phys. B, **10**, 421 (1977)

[93] M. Auzinsh et al., Opt. Commun., **264**, 333 (2006)

[94] L. Lorini et al., "Recent Atomic Clock Comparisons at NIST", EUr. Phys. J. Special Topics, **163**, 19 (2008)

[95] A.K. Mohapatra, T.R. Jackson and C.S. Adams, Phys. Rev. Lett., **98**, 113003 (2007)

[96] S. Mauger, J. Millen and M. P. A. Jones, J. Phys. B, **40**, F319 (2007)

[97] B.P. Stoicheff and E. Weinberger, Phys. Rev. Lett., **44**, 733 (1980)

[98] F. Nez et al., Opt. Commun., **102**, 432 (1993)

[99] H.J. Metcalf and P. van der Straten, Laser Cooling, Springer New York (1999)

[100] M. Rotenberg et al., the 3-j and 6-j Symbols, Technology Press, Massachusetts Institute of Technology Cambridge MA, (1959)

[101] A.K. Mohapatra et al., Nature Physics, **4**, 890 (2008)

[102] P. Meystre and E.M. Wright, Phys. Rev. A, **37**, 2524 (1988)

[103] C. Wagner, R.J. Brecha, A. Schenzle and H. Walther, Phys.Rev. A, **47**, 5068 (1993)

[104] J. Dalibard, Y. Castin and K. Molmer, Phys. Rev. Lett., **68**, 580 (1992)

[105] C.W. Gardinger, A.S . Perkins and P. Zoller, Phys. Rev. A, **46**, 4382 (1992)

[106] H.J Carmichael, An Open System Approach to Quantum Optics, Springer (1993)

[107] J.D. Cresser and S.M Pickles, Quantum Semiclass. Opt., **8**, 73-104 (1996)

[108] H.M Wiesman, Phys. Rev. A, **49**, 2133 (1994)

[109] A. Liebman and G. J. Milburn, Phys.Rev. A, **51**, 736 (1995)

[110] F. Casagrande, A. Lulli and S. Ulzega, Phys .Rev. A, **60**, 1582 (1999)

[111] M.O. Scully and al., Phys. Rev. A, **44**, 5992 (1991)

[112] T. Quang et al., Phys. Rev. A, **48**, 803 (1993)

[113] J.D. Cresser, Phys.Rep., **94**, 47 (1983)

[114] M.O. Scully and W.E. Lamb, Phys. Rev., **159**, 208 (1967)

[115] F. Casagrande et al., Phys. Rev. Lett., **90**, 183601 (2003)

[116] S. Deleglise et al., Nature, **455**, 510 (2008)

[117] N.F. Ramsey, Phys. Rev., **78**, 695 (1950)

[118] L. Essen and J.V.L. Parry, Nature, **176**, 280 (1955)

[119] M.M. Salour and C. Cohen-Tannoudji, Phys. Rev. Lett., **38**, 757 (1977) J.C. Bergquist, S.A. Lee and J.L. Hall, Phys. Rev. Lett., **38**, 159 (1977)

[120] P. Bertet et al., Nature, **411**, 166 (2001)

[121] G.S. Agarwal, P.K. Pathak and M.O. Scully, Phys. Rev. A, **67**, 043807 (2003)

[122] V.B. Braginsky, F.Ya. Khalili, Phys. Lett. A, **186**, 15 (1994)

[123] M.P. Klembovsky, M.L. Gorodetsky and T. Becker, JETP Lett., **79**, 550 (2004)

# Acknowledgment

This work has been possible through the contributions of many people both at the scientific and at a more personal level. Therefore, I would like to thanks them for all their supports during my researchs.

I deeply thank Prof. Herbert Walther, for the opportunity to work on this beautiful Micromaser experiment.

I am very thankful to Prof. Theodor W. Hänsch, who agreed to continue my supervision after the death of Prof. Walther, providing a very motivating environment with new perspectives to continue my PhD.

A special thanks to Dr. Thomas Becker. For his support from the first day, as I started as an internship student till the end of this manuscript, for all the advices, discussions, constructive comments, new ideas and the final correction of this work.

A particular thanks goes to Prof. Pavel Lougovski, for the great friendship started in an office at MPQ, the collaborations and discussions over the years and for valuable comments on earlier versions of this thesis.

I am also very thankful to Dr. Linas Urbonas, Dr. Gabriele Marchi, Dr. Gernot Stania, Mikhael Klembowsky and Dr. Bruno Sanguinetti, who worked with me over the last years, for their positive input and valuable advices.

I also thank all my colleagues at MPQ for the wonderful working atmosphere here, the funny coffee break and in particular Dr. Maria Eckholt, it was very interesting and funny to organize conferences with you.

I also want to thank Mrs. Hermann and all the administrative staff of MPQ who make any bureaucratic work much easier for me. Also a special thanks to Mrs. Faß from the LMU for the help in the management of my Marie Curie Fellowship.

I am thankful to Mr. Thomas Ströbl and the MPQ workshop who always managed to realize high precise work from my not so accurate drawings.

On a more personal level, I would to thank my parents and my brother who always supported me during all these years abroad.

Finally, I would like to thanks all my friends for their support during all these years and especially Giovanna for her presence and patience. Without you, would have been everything more complicated.